DESIGN OF MULTI-CHANNEL SPECTROMETERS FOR SCANNING ION/ELECTRON MICROSCOPES

KANG HAO CHEONG

(B.Sc.(Hons), National University of Singapore)

A Thesis Submitted for the Degree of Doctor of Philosophy

Department of Electrical and Computer Engineering

National University of Singapore

2014

Declaration

I hereby declare that this thesis is my original work and it has been written by me in its entirety. I have duly acknowledged all the sources of information which have been used in the thesis. This thesis has also not been submitted for any degree in any university previously.

Kang Hao Cheong
18 August 2014

Acknowledgements

I am extremely fortunate to be, again, deeply indebted to my supervisor, Professor Anjam Khursheed, for his advice, encouragement and support during this project and taking time to read through the thesis. Thank you for giving me the opportunity to take up your research project for my FYP and PhD.

I would like to thank all the staffs in CICFAR lab, particularly Mrs Ho and Linn Linn. Special thanks go to my seniors, Dr. Mans Osterberg and Dr. Hung Quang Hoang for all their guidance and Mr. Nelliyan Karuppiah for the technical advice throughout the project. I truly appreciate the support and fruitful discussions with Mr. Avinash Srinivasan, Mr. Han Weiding and Mr Tan Zong Xuan. Thank you for everything!

I would like to express my gratitude to my wife, Li Fang who has been behind me at every stage, providing unwavering support, patience and understanding. Finally, I would like to dedicate this thesis to Li Fang.

Contents

Summary

The potential advantages of multi-channel analysers over conventional sequential detection are well known and are active areas of research both for electron energy spectroscopy and ion mass spectroscopy. Their inherent advantage of capturing the entire spectrum in parallel, promises at least an order of magnitude speed up in data acquisition times for analytical techniques such as Auger Electron Microscopy (AES) and Secondary Ion Mass Spectrometry (SIMS). Recently, a new set of multi-channel spectrometer designs have been proposed which involve the simultaneous adjustment of an array of electrode voltages/coil currents using computational simulation methods, departing from the traditional approach of using certain analytical field distributions or electrode shapes. The aim of this PhD work is to critically evaluate these more complex multi-channel designs and further develop them, transforming them into realistic engineering designs from which prototype analysers can be made.

Direct ray tracing methods together with the Damped least-squares method were used for evaluating and developing realistic engineering spectrometer designs. Two such multi-channel energy analysers were developed for the Scanning Electron Microscope (SEM), while another multi-channel mass analyser was made for Focused Ion Beam (FIB) instruments.

The first energy analyser functions as a parallel energy magnetic box spectrometer. It uses a deflection field that is allowed to vary in such a way that it steadily increases in the path of incoming electrons; electrons having a wide range of different energies can be deflected and focused on to a flat detector. The simulation methods used for the design were able to account for magnetic saturation and the 3D fringe field at the entrance slit, something which had not

been previously achieved. The analyser entrance geometry was also transformed into a conical upper part so that it can be used as an add-on attachment in the SEM, allowing for short SEM working distances (< 20 mm). With these modifications, the simulated relative energy resolution is predicted to lie below 0.13% for an entrance polar angular spread of ± 50 mrad across the Auger electron energy range of 50 to 2500 eV on its intrinsic plane. This energy resolution is typically over an order of magnitude better than previous wide-range multi-channel analysers proposed for parallel AES, such as the Hyperbolic Field Analyser. A prototype of this analyser design was built, and its experimentally measured magnetic field distribution lay close to the predicted simulation field distribution, with a margin of error below 5%.

The second multi-channel energy analyser uses an array of electrodes to create an electric retarding field to mirror and deflect electrons through an exit grid so that they are focused onto a flat detection plane for a wide energy range (typically 50 to 2500 eV). The analyser is rotationally symmetric and is predicted to have second-order focusing properties (high quality focusing optics) across the entire energy range. Several design features of this analyser were altered in order to transform it into an analyser attachment for the SEM, such as extending its working distance, defined as the distance from the specimen to the entrance of the analyser. Three-dimensional simulation was also used to investigate the fringe fields of various exit grid layouts. A prototype of the analyser was made and designed for multi-channel detection using an array of channeltrons. The whole arrangement was fitted as an add-on attachment inside a SEM. The experimental results provide preliminary proof-of-principles to demonstrate that the PRMA prototype can function as an energy spectrometer attachment inside a SEM.

Lastly, a mass analyser based upon the parallel magnetic sector box analyser design has been developed for FIB instruments. Simulations predict that, in combination with a sector energy spectrometer, it can be used to deflect and focus ions having a wide range of charge-to-mass ratios onto a flat plane detector. However, the simulation results also predict that the focusing properties are likely to be degraded by magnetic saturation if made too small, and that there are definite limits to how compact it can realistically be. Feasible analyser lengths need to be around 500 mm or more, making it better suited to a dedicated SIMS instrument, rather than as an attachment for a FIB.

List of Tables

List of Figures

List of Symbols

SYMBOL	DESCRIPTION
B	Magnetic field strength
Ψ_1, Ψ_2, Ψ_3	Magnetic scalar potential
C_c	Chromatic aberration term
C_s	Second-order spherical aberration term
E_p	Pass energy of analyser
SE	Secondary electron
SNR	Signal-to-noise ratio
T	Transmittance (transmission) of a spectrometer
$V, V_1, V_2, V_3, , V_4, V_5, V_6, V_7, V_8, V_9, V_{10}, V_{11}, V_D$	Potentials applied to electrodes
V_{DEF}	Deflection voltage of the analyser
V_M	Mirror voltage
V_S	Specimen voltage
W	Working distance
CMA	Cylindrical mirror analyser
DLS	Damped least-squares method
FIB	Focused Ion Beam
HDA	Hemispherical deflector analyser
PRMA	Parallel radial mirror analyser
SDA	Spherical deflector analyser

Chapter 1 : Introduction

At present, the detection systems of the Scanning Electron Microscope (SEM) or Focused Ion Beam (FIB) are not generally designed to capture the energy spectrum of the ions/electrons scattered from the sample. Their output signals are formed by secondary and backscattered electrons/ions, which are usually detected separately, as shown in Figure 1.1. The energy spectra of these scattered particles contain valuable information about the sample under study.

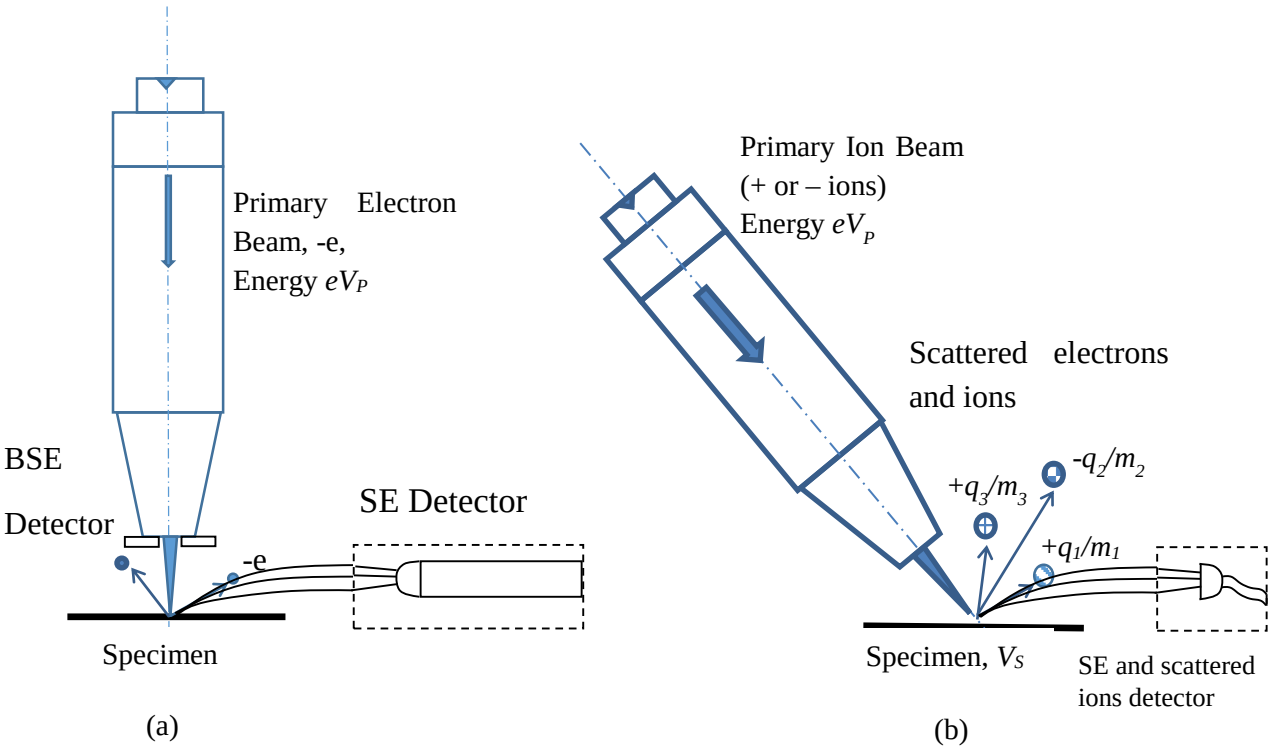

Figure 1.1: Focused electron/ion beam columns: (a) Electron microscope (b) Ion microscope.

Figure 1.2 depicts a schematic representation of the various kinds of signals generated from the primary beam/specimen interaction inside a SEM. As the primary beam penetrates the specimen surface, it scatters electrons from a range of different depths, some of which escape from the surface. Scattered electrons that escape from close to the specimen surface are known as secondary electrons and are created by inelastic collisions. Electrons that are scattered back from deeper levels are known as backscattered electrons and they are generated by multiple

elastic collisions. Secondary and backscattered electrons make up the two most common signals that are used to form the SEM image.

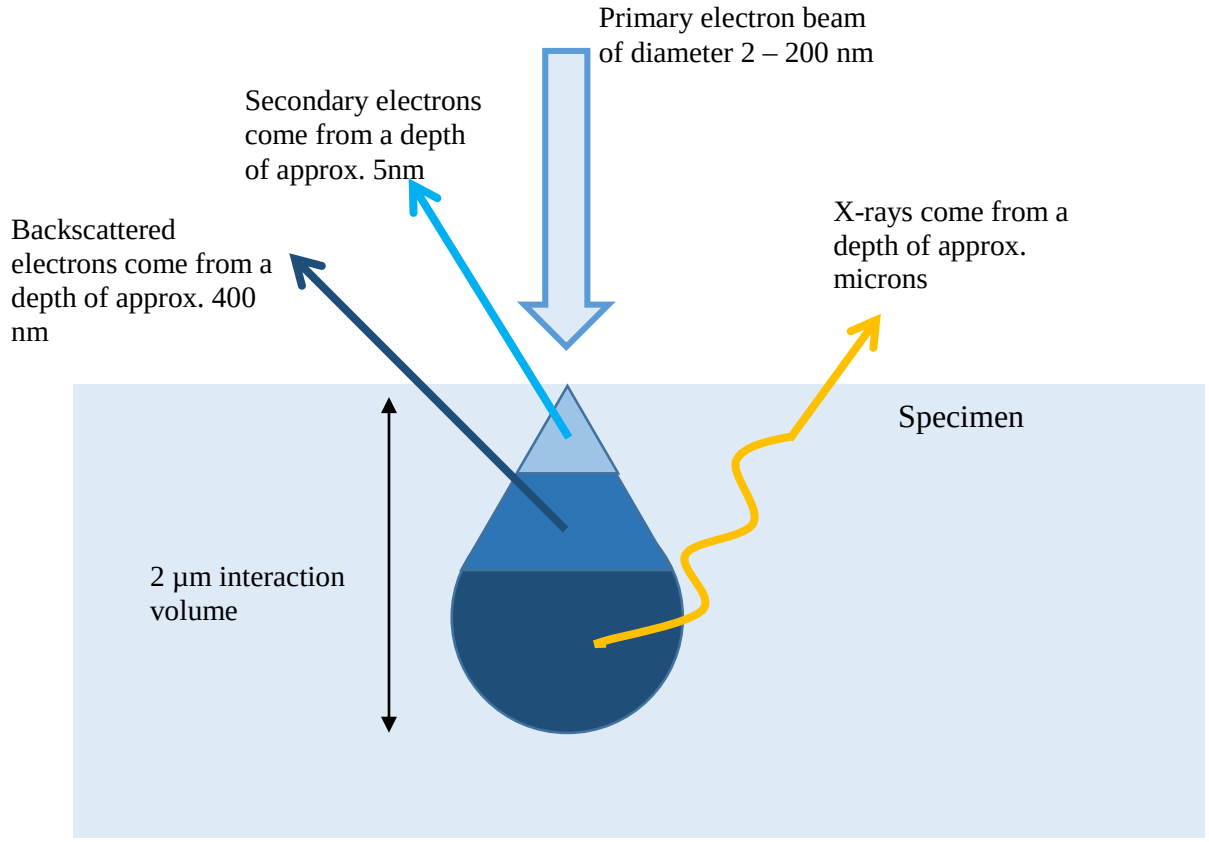

Figure 1.2**:** The typical spatial resolution of different signals - secondary electrons, backscattered electrons and X-rays in the SEM. Different signals come from different depth.

Figure 1.3 depicts the form of the energy distribution of the scattered electrons from the sample inside a SEM. Secondary electrons have low energies and are defined to be those electrons that have energies less than 50 eV. Most of them, however, lie in the 0.5 to 5 eV energy range. Backscattered electrons are defined to lie in the broad energy range of 50 eV up to the primary beam energy. Auger electrons emanate from inner atomic shells and their energies show up as characteristic peaks in the energy spectrum. Secondary electrons provide information about the sample's surface topography, and the image formed from the secondary electron detector's signal is the most widely used type of image generated from the SEM. It is typically used to

inspect how the surface of a sample looks on the nano-scale. The backscattered electron spectrum changes significantly with atomic number, and in practice, imaging from backscattered electrons in the SEM provides useful qualitative material information about the specimen, and is frequently used in addition to the topographic information obtained from secondary electrons. The primary beam current is typically in the pico to nano-amperes range. Although the beam spot diameter can be less than 2 nm, the spatial resolution of the SEM is usually limited by the interaction volume of generated within the sample (usually in the micron range for beam energies above 5 keV).

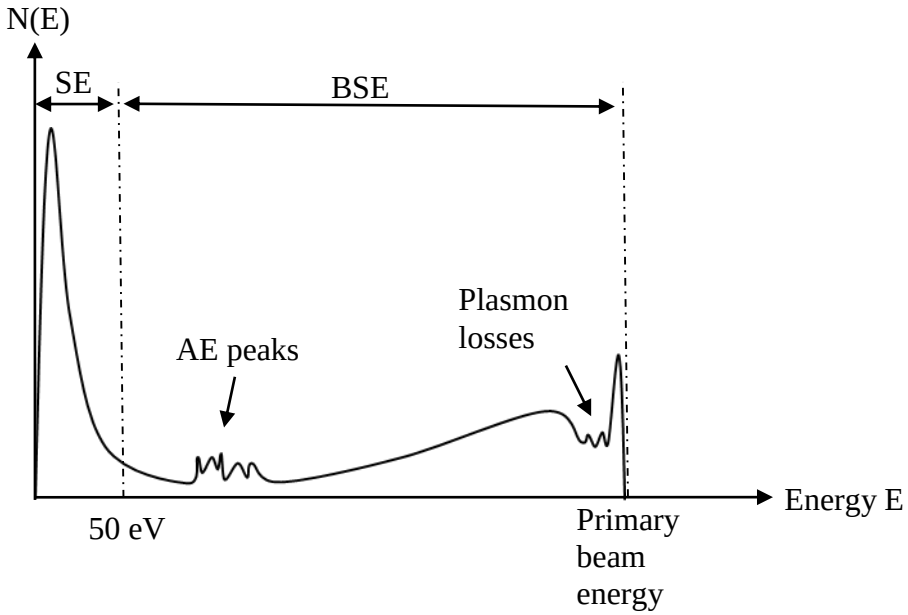

Figure 1.3: Energy distribution of scattered electrons.

Figure 1.4 depicts the energy spectra of atomic and molecular $A1_n^+$ ions (n = 1, 2 and 6) emitted from sputter-cleaned aluminium under impact at normal incidence of 10 keV Ar^+ ions [1.1]. At very low energies, the measured secondary ion yield increases rapidly, passes through a well-defined peak and then decreases towards higher energies. For large ion clusters ($n \geq 3$), the peak moves towards low energies with increasing n. Moreover, the fall-off on the high-energy

side of the peak is steeper for larger *n* [1.1]. The spectral features seen in Figure 1.4 are observed generally in Secondary Ion Mass Spectrometry (SIMS), not only for homonuclear molecular ions but also for heteronuclear ions [1.2]. These secondary ions are either positively or negatively charged and have kinetic energies of the order of 20 eV, but different ions have different energy distributions. The secondary mass spectrum is obtained by collecting the secondary ions and subjecting them to mass-to-charge ratio filtering prior to detection. The mass spectrometer also has to incorporate ways to suppress the adverse effects caused by initial energy and angular spread from the sample. The primary ion beam current is in the nano-ampere range, and the spatial resolution in most SIMS instruments is typically in microns.

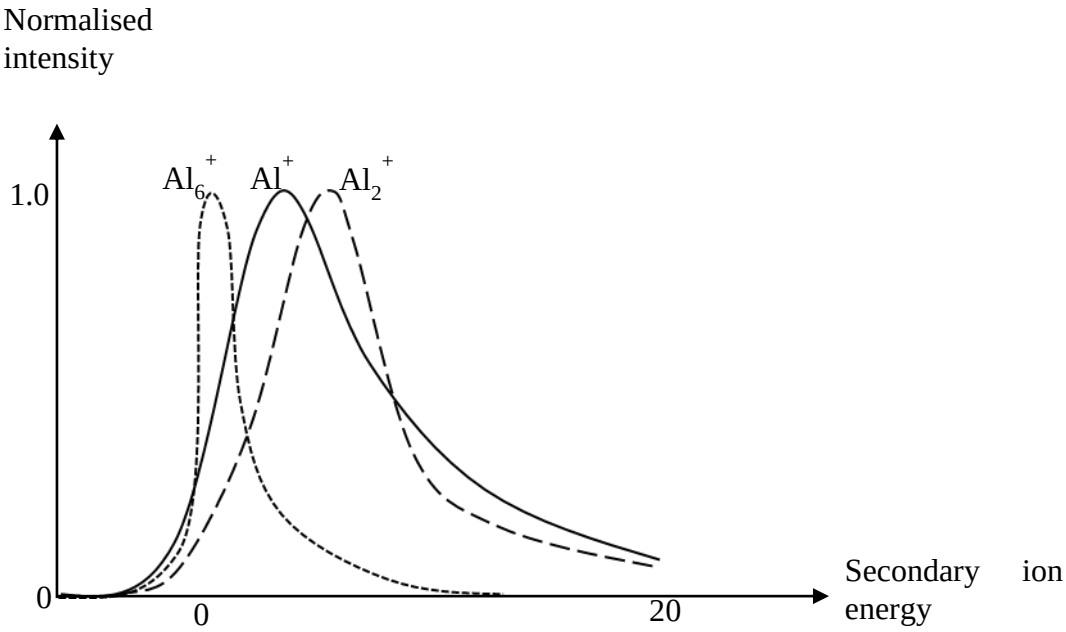

Figure 1.4: Energy spectra for atomic and molecular secondary-ions sputtered from aluminium [1.1].

Ion/electron mass/energy spectrometers are commonly used in surface science analytical techniques such as Auger Electron Microscopy (AES) and SIMS. The kind of spectrometers used in Scanning Auger Microscope (SAM) and SIMS systems are far too large and complex

to be integrated directly into the SEM or FIB. For this reason, SAM and SIMS have become stand-alone specialized surface science instruments that provide mainly elemental/chemical information. These instruments require ultra-high vacuum (UHV) at the specimen, making them much more costly and complex than the FIB and SEM, which require a moderate vacuum. UHV is necessary for these applications in order to reduce surface contamination. At 0.1 mPa (10^{-6} Torr), it only takes 1 second to cover a surface with a contaminant, therefore, much lower pressures are needed for long experiments.

Both the SAM and SIMS have a modest imaging capability, largely confined to the micron-scale, unlike the FIB or SEM, which can image on the nano-scale. In the SEM, the main analysis tool for defect/material analysis is the energy-dispersive X-ray spectroscopy (EDS) method, which often uses a lithium doped silicon detector to monitor the energy of the emitted X-rays from the sample. This technique is fast due to the parallel acquisition of X-ray energies, but is limited by a spatial and depth resolution of about 1μm and is difficult to use for low energy electron beam applications (<10kV) [1.3]. As the technology roadmap for semiconductors predicts nodes smaller than 32 nm, as well as emerging nanotechnology, standard defect inspection technique like the EDS will no longer be sufficient due to its limited spatial resolution [1.4].

The problems described above, provide the main motivation for the work to be carried here, which aims to develop multi-channel electron energy spectrometer attachments for the SEM and a mass spectrometer attachment for FIB instruments, so that quantitative elemental analysis can be mapped with high image resolution, on the nano-scale. In particular, this thesis will leverage on some multi-channel spectrometer designs already made by Khursheed, to be

described in more detail in section 1.4, and to further develop these designs into practical engineering prototypes.

1.1 Sequential band-pass energy spectrometers

Electron energy spectrometers can be understood best in terms of the energy range that they are designed to capture, and whether scattered electrons are detected sequentially or in parallel. Most electron energy spectrometers proposed for the SEM have been made for the purpose of quantifying voltage contrast, a technique based upon detecting the shift in the SE spectrum as a means to measuring surface potential changes, typically for the purpose of monitoring signals on Integrated Circuit tracks. This was largely confined to retarding field spectrometers, which capture an integrated form of the SE spectrum [1.5]. However, interest in voltage contrast spectrometers gradually declined in the 1990s, shortly after the practice of covering Integrated Circuits with a ground metal layer was introduced, preventing SEM inspection. Apart from voltage contrast spectrometers, very few other electron energy spectrometers have been proposed for the SEM.

An electrostatic toroidal deflection analyser attachment for the SEM designed to capture the BSE spectrum scattered from the specimen under test was designed by Rau and Robinson [1.6, 1.7]. Figure 1.5 depicts the schematic diagram layout of this toroidal spectrometer. The spectrometer is characterized by first order optics, for aperture slits required to give sufficient electron intensities at the detector, the energy resolution was measured to be 2.5% [1.8], considerably worse than those normally used for Auger analysis (< 0.3%). First-order optics (focusing) is defined by the focal point position staying constant with respect to first-order changes in input polar angle, that is, to the first-order, trajectories that leave with slightly different initial angles focus at the same exit point. Second-order optics (focusing) is defined

by the focal point position not changing with respect to second-order variations in the input angle [1.5].

The Rau and Robinson toroidal spectrometer has the added complication that the detector must lie on a cylindrical wall shaped surface, making it difficult to take advantage of its rotational symmetry. The spectrometer was used for providing depth information of multi-layer thin films by monitoring BSE energy spectra inside the SEM [1.8]. Recently, the same spectrometer design was successfully used for monitoring specimen charging, where specimen surface charges to -5 kV [1.9].

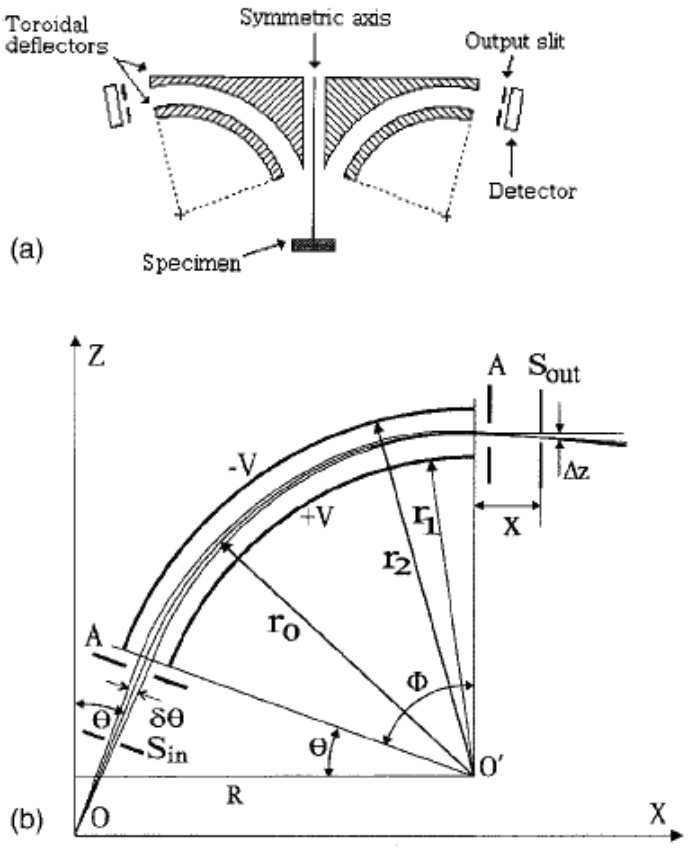

Figure 1.5: Schematic diagram layout of a first-order focusing toroidal spectrometer reported by Rau and Robinson: (a) Cross-section showing specimen and detector; (b) Simulation layout, OZ is the rotational axis of symmetry [1.6].

Toroidal energy spectrometers that are designed to collect electrons/ions over 2π radian emission angles in the azimuthal direction typically have first-order focusing properties only. Khursheed and Hoang recently proposed a second-order focusing toroidal spectrometer design, one that is based upon obtaining an intermediate focus in the r-z plane, which allows for second-order spherical aberration contributions accumulated before and after the intermediate focus to cancel [1.10], as shown in Figure 1.6. A range of different geometrical designs were investigated, the best of which predict an energy resolution of 0.146% for acceptance angles between $\pm 6^{o}$. The spectrometer has a limited parallel energy acquisition mode, where the increase in energy resolution with respect to the band centre rises by less than a factor of 2 for energies that lie within $\pm 4\%$ of the pass energy; a maximum input angular spread of $\pm 10^{o}$ and a maximum parallel energy band width of $\pm 15\%$ (30% total) of the pass energy. The central ray enters the spectrometer at an angle of 45^{o} with respect to the horizontal axis and the input angular spread in the azimuthal direction is 100^{o}. The toroidal energy analyser has found its applications in mapping dopant carrier concentrations in semiconductor devices where shifts in SE spectra of several mV can be monitored [1.11], and has also been used to provide material quantification from the BSE spectrum [1.12].

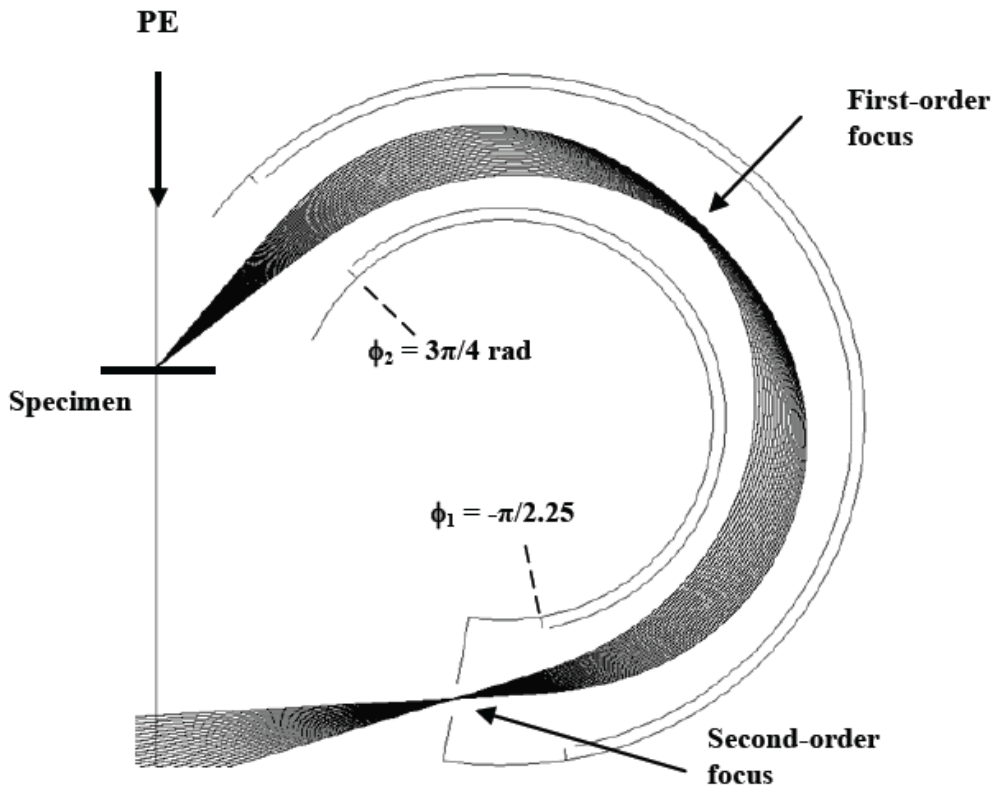

Figure 1.6: Simulated ray paths of electrons through the spectrometer at the pass energy for a wide variety of entrance angles. The central ray enters in at 45º and 21 trajectories are plot over uniform steps for an input angular spread varying from -104 mrad to +104 mrad (-6º to 6º) [1.10].

For Auger Electron Spectrometry (AES), the Scanning Auger Microscope (SAM) is normally used, instead of integrating an energy spectrometer into the SEM chamber. This is due to two main reasons. The first reason is that AES requires Ultra High Vacuum (UHV) conditions (typically 10^{-9} to 10^{-10} Torr), in order to prevent the build-up of contaminating layers on the specimen surface. In a SEM chamber, where the vacuum level ranges between 10^{-5} to 10^{-6} Torr, layers of hydrocarbon would in a matter of seconds build-up on the specimen surface and make it impossible to carry out AES. The second main reason is the limited space available inside the SEM chamber for the energy analyser. The specimen chamber typically measures 250 mm

by 250 mm by 200 mm, most of which is taken up by the pole-piece of the final lens, specimen stage, and BSE/SE detectors.

The two most commonly used energy analyser designs for the SAM are the Cylindrical Mirror Analyser (CMA) and the Hemispherical Deflector Analyser (HDA). The CMA consists of two co-axial cylinders with a potential difference applied across them, as shown in Figure 1.7. Here the electron beam focusing column is located inside the spectrometer. Only electrons with a suitable energy range can pass through electric field created by the potential difference without hitting either of the cylinders. Sar-El first described the CMA in [1.13] and Palmberg used it to observe Auger electron spectrum [1.14]. The CMA was subsequently developed by many research groups for charged particle spectrometry applications [1.15, 1.16].

The best resolution of the CMA for an angular spread of ±6°, theoretically without the effect of the output aperture is known to be around 0.155% [1.17]. The CMA is characterised by its second-order optics and this best resolution is typically around a factor of 6 times better than most other types of spectrometers which are usually characterized by first-order optics [1.18].

In practice, CMAs operate with an energy resolution ranging from 0.25% to 0.7% for an angular spread of ±6° [1.19]. The poorer resolution is largely due to the depth of focus error, which is caused by specimen misplacement. From a transmittance point of view, the CMA is very efficient because it has rotational symmetry and all electrons that pass through it are deflected by the same field distribution, neglecting the finite size of the source. The transmittance of the second-order focusing CMA is estimated to be 16.84% (an angular spread of ±6º), assuming that its entrance/exit grids have 90% transparency. As illustrated in Figure 1.7, both the specimen and focal point must lie on the rotational axis of symmetry. However,

the electron optical column is required to be placed inside the analyser, in a field-free central region, thereby making it difficult to combine the CMA with other existing electron beam instruments such as the SEM.

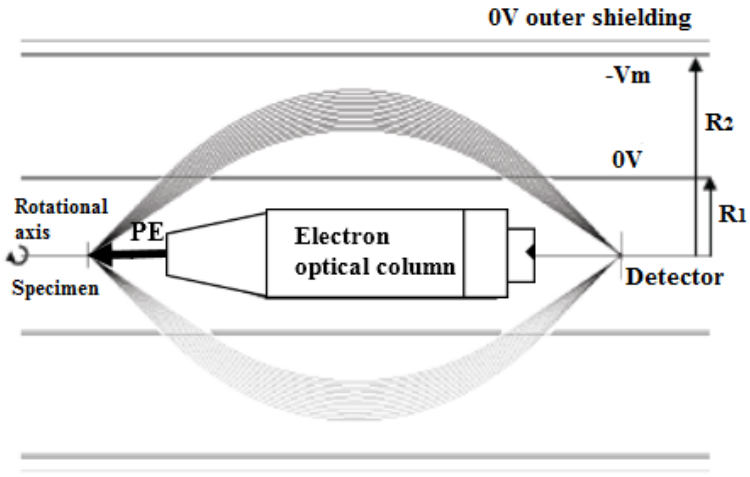

Figure 1.7: The CMA layout. The electric field distribution is created between concentric cylinders which are biased at different voltages, the inner one is usually grounded, located at radius R_1 from the rotational axis of symmetry, and the outer one, located at radius R_2 is biased to a mirror voltage ($-V_m$). [1.5].

It turns out that the HDA is presently the most widely used electron energy analyser for auger electron energy acquisition. It is constructed by two inner and outer hemispheres with radii R_1 and R_2, in which the inner is grounded and the outer is biased at a potential V_m to deflect incoming electrons as shown in Figure 1.8. Although the HDA is characterized by first-order focusing properties and has a poor energy resolution when used individually (around 2% for an angular spread of ±6º in both in-plane and out-of-plane directions) [1.18], it is usually combined with a series of lenses in a pre-analyser decelerating column that allows it to operate in a retardation mode as shown in Figure 1.8, effectively lowering the analyser pass energy.

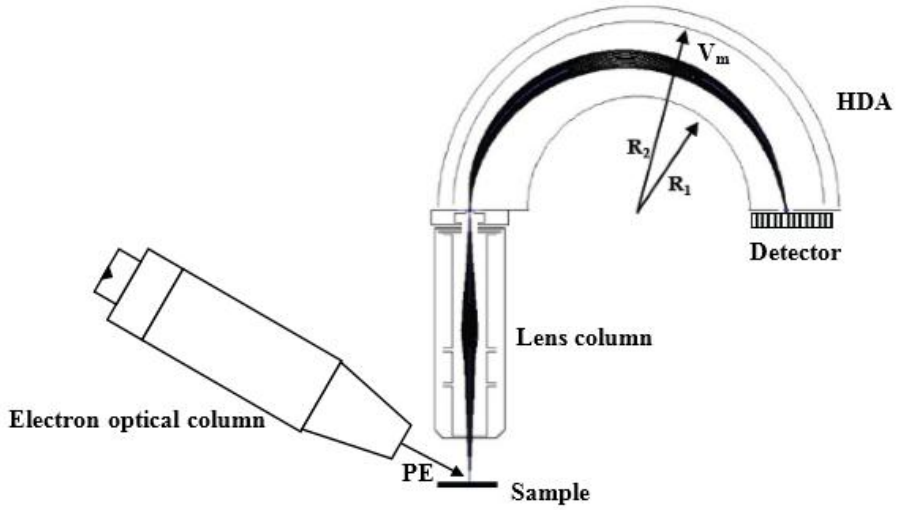

Figure 1.8: Schematic diagram of a HDA combined with its pre-retardation lens column [1.5].

A relative energy resolution below 0.05% can be achieved by the HDA in its retarding mode [1.20]. However, the transmittance is comparatively low, due to its small angular azimuthal angle collection range, usually below ±3° entrance angular spread, about 50 times lower than that for the CMA. A single detector can also be placed at the analyser exit plane, instead of an aperture slit, and the HDA can be operated in a multi-channel mode with a band-pass width of around ±3% of the pass energy. Its main advantage lies in its ability to slow electrons within it, effectively bring down the pass energy, and thereby increasing its energy resolution.

A practical constraint for the HDA is that it is usually attached to the specimen chamber, coming in at angle of typically 45° to the electron focusing column. The whole spectrometer is many more times larger than the specimen chamber and normally hangs to one side of it. Hence, the HDA system is typically placed outside the specimen chamber of the SAM. The pre-retardation lens is integrated into the specimen chamber through a port to collect scattered

electrons from the specimen. This arrangement is not suitable for combining it with existing SEM, since SEM chambers are relatively small and the space in between the objective lens and the specimen is limited by a short working distance (of less than a few centimetres).

For reasons stated above, it is difficult to integrate the usual sequential Auger spectrometers, the CMA and the HDA, with existing SEM instruments for the purpose of AES. Electron energy spectrometers that are suitable for AES (that have a comparable performance to the CMA and the HDA) must be specially designed to fit as compact attachments that can fit into the limited space of existing SEM specimen chambers. Two such sequential analysers have been designed so far, although their usage as Auger electron spectrometers in the SEM is still not feasible due to the UHV requirement. One such spectrometer is the second-order toroidal analyser already mentioned, by Hoang and Khursheed [1.10], which has an energy resolution that is comparable to the CMA (not taking into account the depth of focus problem). Hoang and Khursheed have experimentally verified their simulated resolution predictions [1.21]. Figure 1.9(a) shows a layout diagram of the second-order toroidal analyser fit into the SEM chamber [1.22]. The other analyser designed for the SEM is the Radial Mirror Analyser (RMA), and is shown in Figure 1.9(b) [1.23]. The RMA is rotationally symmetric about the primary beam axis, capable of 2π radian detection, and has a predicted relative energy resolution of better than 0.025% for a polar angular spread of ±6°, around an order of magnitude better than the CMA for the same acceptance angle, and comparable to the best energy resolution of the HDA.

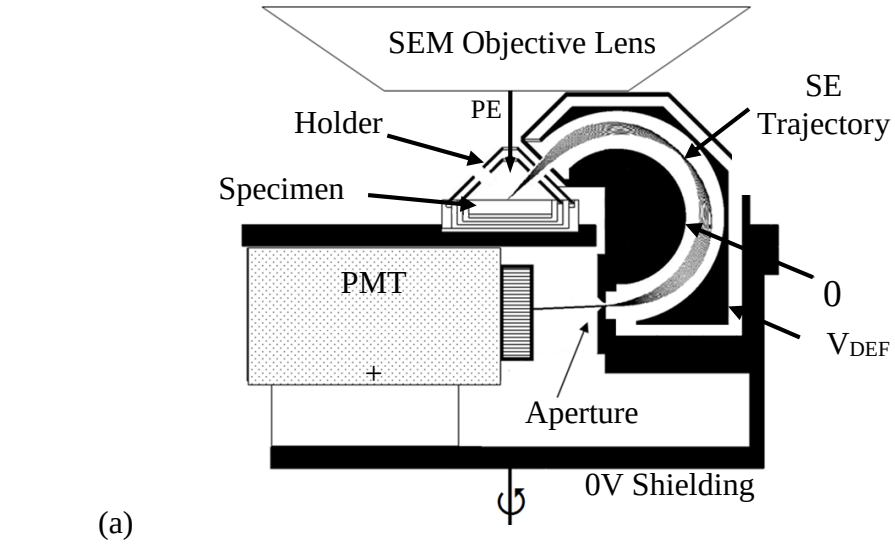

(a)

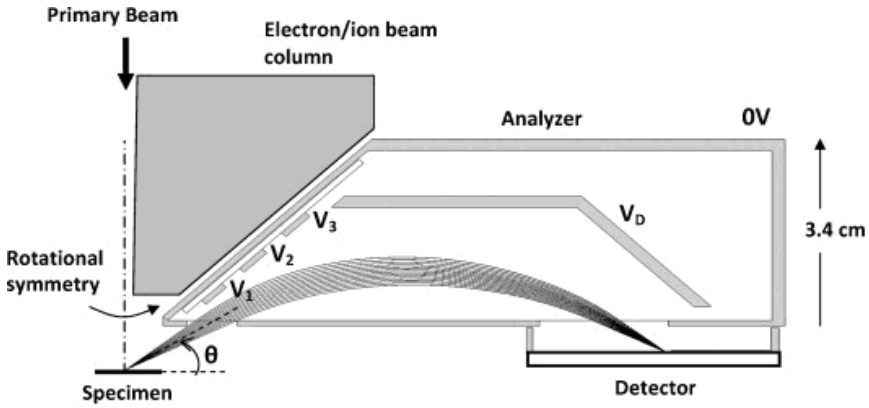

(b)

Figure 1.9: Two sequential analysers specially designed to fit as compact attachments that can fit into the limited space of existing SEM specimen chambers (a) Layout diagram of the second-order toroidal analyser being fit into the SEM chamber [1.22] (b) Layout diagram of the RMA being fit into the SEM chamber [1.23].

1.2 Sequential mass spectrometers

Another application of the kind of add-on spectrometer designs to be pursued in this thesis is the combination of FIB with SIMS. The ability to modify/change the specimen surface with the FIB on the nano-scale and at the same time obtain material composition information through SIMS has many potential benefits for the nanofabrication of semiconductors. There are a variety of different mass spectrometers used in SIMS, ranging from the use of (a) electric/magnetic sector fields, (b) electrostatic field time-of-flight to (c) RF quadrupole fields. The most compact of these spectrometers is the RF quadrupole field spectrometer. Proposals to combine FIB with SIMS are mostly based on the RF-quadrupole spectrometer, but they usually require bulky special purpose systems where the SIMS is placed alongside the FIB. An example of an attempt to combine FIB and SIMS in this way is shown in Figure 1.10, a system that was jointly developed by the University of Chicago and Hughes Research Laboratories in the early 1980s.

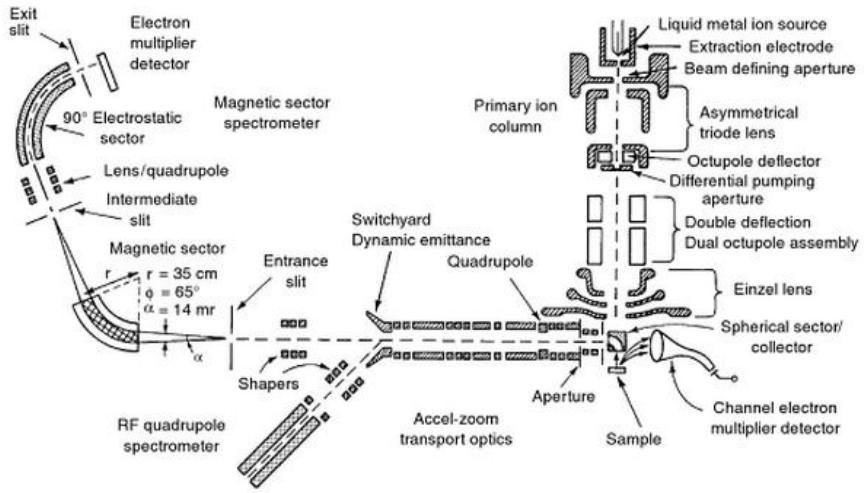

Figure 1.10: Schematic diagram of University of Chicago FIB-SIMS secondary-ion mass spectroscopy in collaboration with Hughes Research Laboratories [1.24].

The magnetic sector design (with the use of an electric sector) is generally able to achieve a higher mass resolution than the other two types of mass spectrometers for SIMS [1.25]. A well-

known example of a sector field mass spectrometer is shown in Figure 1.11. The design consists of a 90º deflecting cylindrical electrostatic sector field and the 60º deflecting homogeneous magnetic sector field [1.26]. The energy dispersion in the electrostatic sector cancels out the dispersion in the magnetic sector, therefore ions are focused both with respect to energy and angular on the detector plane, and dispersion is according to their mass-to-charge ratios. This is known as the double focusing property. Such a mass analyser is operated in a sequential mode, where the strength of the magnetic field sector is ramped in time, and different charge-to-mass ion ratios are captured as a time varying signal at the detector.

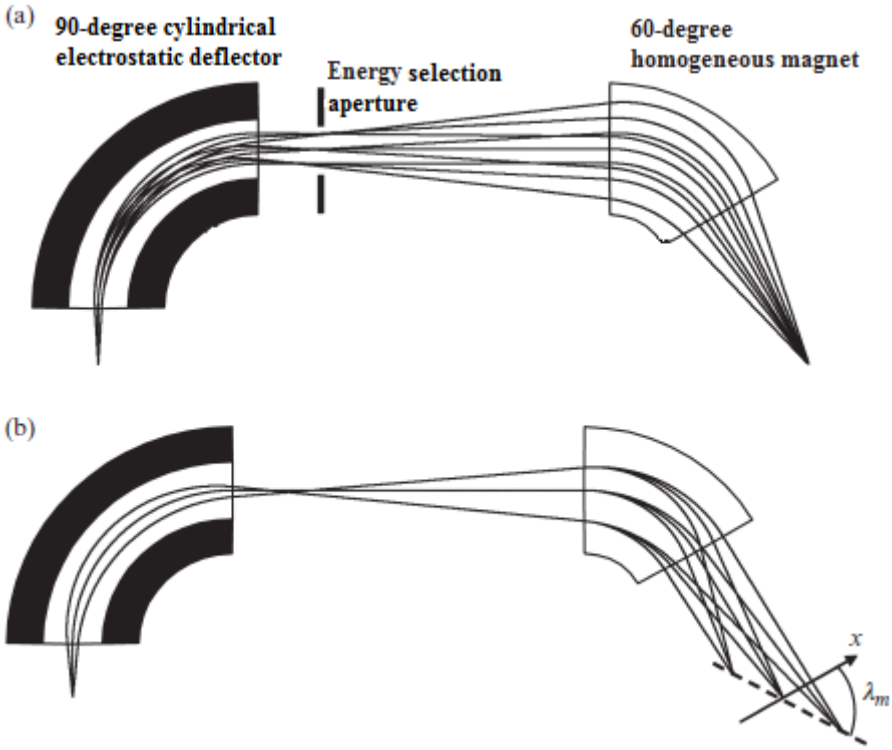

Figure 1.11: (a) Trajectories of ions with different energies and initial directions in the dispersion plane of the mass analyser with double focusing; at the intermediate Gaussian image plane an aperture can be placed to restrict the energy spread accepted by the analyser (b) Trajectories of ions with different masses and initial directions in the same analyser; the points of the final images form the ‘‘angular’’ mass focal line inclined with respect to the profile plane by the angle λ_m = 62.9º [1.27].

1.3 Parallel wide-range analyser designs

A common feature of the analysers discussed so far are that they are sequential, that is, an analyser electrode needs to be ramped in time in order for them to generate either an energy or mass spectrum, this greatly restricts the overall data-acquisition time. In AES, for a typical electron energy spectrum exceeding the 2500eV range, the total acquisition time can be of the order of minutes [1.28]. Therefore, parallel energy acquisition, where the output signal over a wide range of different energies is obtained simultaneously, has been the subject of considerable research, and forms the overall theme of this thesis. Parallel analysers can speed up data-acquisition times by more than an order of magnitude, reducing the acquisition of an Auger Electron Spectrum to less than a few seconds. Some previous multi-channel (parallel) spectrometer designs that allow different energies to be obtained simultaneously will be reviewed in this section.

The first fully multi-channel voltage contrast spectrometer for the SEM was designed by Khursheed and Dinnis [1.29]. Their proposal was based upon using the time-of-flight of secondary electrons in which the primary beam is pulsed, as is normally required for time resolved voltage contrast measurements on integrated circuits. Blanking of the beam may inevitably reduce the output average current by one to two orders of magnitude. The specimen is placed in a magnetic immersion lens, and the secondary electrons are collimated as they travel up the objective lens bore, as shown in Figure 1.12.

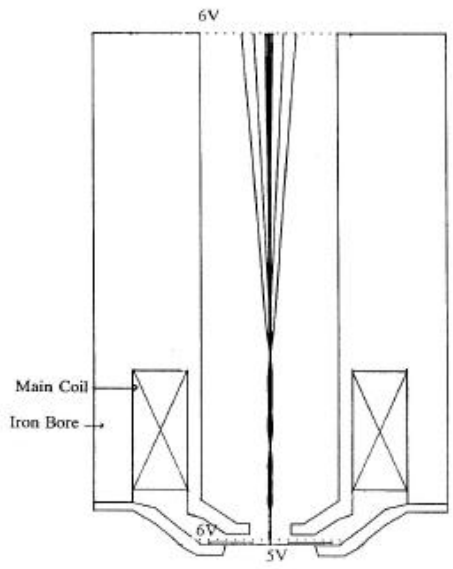

Figure 1.12: Simulated 3 eV SE trajectory paths through a time-of-flight voltage contrast analyser for a wide-variety of different emission angles [1.29].

A high bandwidth detector system collects the secondary electrons at the top of the objective lens. The lens bore acts as a drift-tube region for the secondary electrons. The sharply decreasing axial field strength through which the secondary electrons initially travel will not only collimate the secondary trajectory paths, but make their time-of-flight relatively independent of their initial emission angle. Under these conditions, the output signal will be directly related to the form of the initial secondary electron energy spectrum [1.30]. Although strictly speaking, the time-of-flight spectrometer output signals are sequential in nature, that is, they involve the recording of a signal that varies in time (with the arrival time of electrons), they do not involve any analyser electrode voltage being ramped. The arrival time spread is generally many orders of magnitude smaller than the rate to which analyser deflection electrodes can be ramped. For this reason, time-of-flight spectrometers are usually referred to as multi-channel or parallel spectrometers [1.5].

The other main contribution towards a multi-channel analyser design with a SEM column has come from Kienle and Plies [1.31]. Kienle and Plies proposed a parallel energy multichannel SE analyser design for a mixed field objective lens based upon the use of Wien filters [1.31]. Figure 1.13 shows the schematic layout for this multi-channel secondary electron off-axis analyser reported by Kienle and Plies. The primary beam travels through the column and is decelerated down to a landing voltage of 1 kV at the specimen. SEs are typically accelerated to 8 kV as they travel back up the column, and are deflected off-axis by a Wien filter. They are then further deflected and dispersed by an electric spherical deflector analyser (SDA), after which their image is magnified and focused on to the Yttrium Aluminium Garnet (YAG) scintillator to generate a light image, which is captured by a CCD placed behind the scintillator. The whole spectrum of SEs from 0 to 20 eV can be simultaneously captured. This design can also be set to another operating mode, where it captures the BSE. As depicted in Figure 1.13, the Kienle and Plies spectrometer has the disadvantage of requiring a complicated redesign of the electron column. Another Wien filter needs to be placed further up the column, in order to cancel out adverse energy dispersion and second-order geometrical aberration effects on the primary beam. In addition, several stages of magnifying the energy dispersion are also required, since the lower Wien Filter only deflects the secondary electron beam by 15°, and the SDA is limited to a deflection angle of 75°. Another limitation of using a Wien filter for electron energy spectrometers is that its energy dispersion is relatively low, resulting in poor performance of its spectrometer action. This analyser is fully multi-channel and is able to capture spectral energy information in parallel, like the SEM time-of-flight analyser designed by Khursheed and Dinnis.

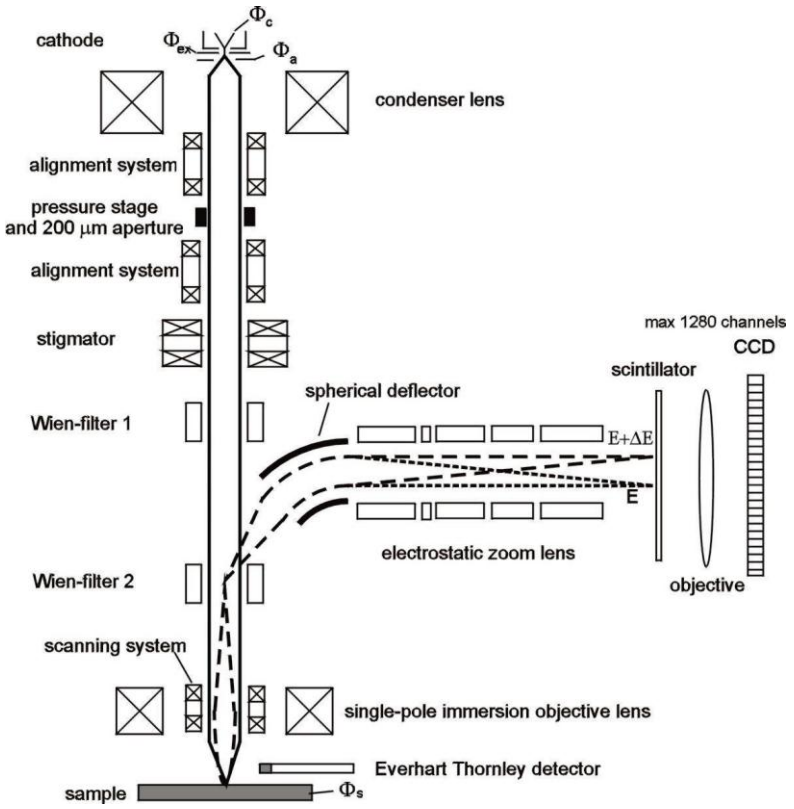

Figure 1.13: Schematic layout for the multi-channel secondary electron off-axis analyser reported by Kienle and Plies [1.31].

New possibilities of using multi-channel energy spectrometers for other applications inside the SEM other than for voltage contrast and for acquisition of SE spectra are recently emerging. For instance, the possibility of carrying out AES in the SEM has been demonstrated in the work by El-Gomati [1.32, 1.33] and Cubric [1.4], where the Auger spectrum from a specimen can be acquired by a fast energy analyser after cleaning its surface by ion bombardment. In order to acquire the Auger spectrum fast enough (in seconds), a parallel analyser attachment is required. This makes AES a promising tool for analysing nano-scale defects and elemental identification inside the SEM. If a high performance electron energy spectrometer and an ion flood gun can be incorporated into a SEM without greatly increasing the working distance, there is the potential for the SEM to be used as a low cost instrument for both imaging and spectroscopic analysis on the nano-scale. However, this means multi-channel energy

spectrometer attachments for the SEM must specifically be designed for AES, and not limited to SE spectral range, as with previous voltage contrast analyser designs.

The hyperbolic field analyser (HFA) proposed by Jacka et al. [1.34, 1.35] is a parallel energy analyser design proposed for Auger electron microscopy. Figure 1.14 shows a schematic diagram of the HFA. It can collect an energy spectrum in parallel with a range defined by Emax/Emin ≈36 and is typically set to capture a spectrum from about 75 eV to greater than 2500 eV. Compared to most electron energy analysers, the total transmission efficiency of the HFA is small. It can only collect 0.05% of 2π sr emission in order to provide an energy resolution of a few eV. However, the data acquisition time over the entire energy range between 75 eV to 2500 eV is very fast, normally less than 50 ms [1.28]. This parallel energy analyser has been developed and commercialized by Shimadzu corporation for fast analysis on the nano-scale [1.4]. The HFA analyser has also been incorporated into the chamber of a conventional SEM due to its compact size [1.4].

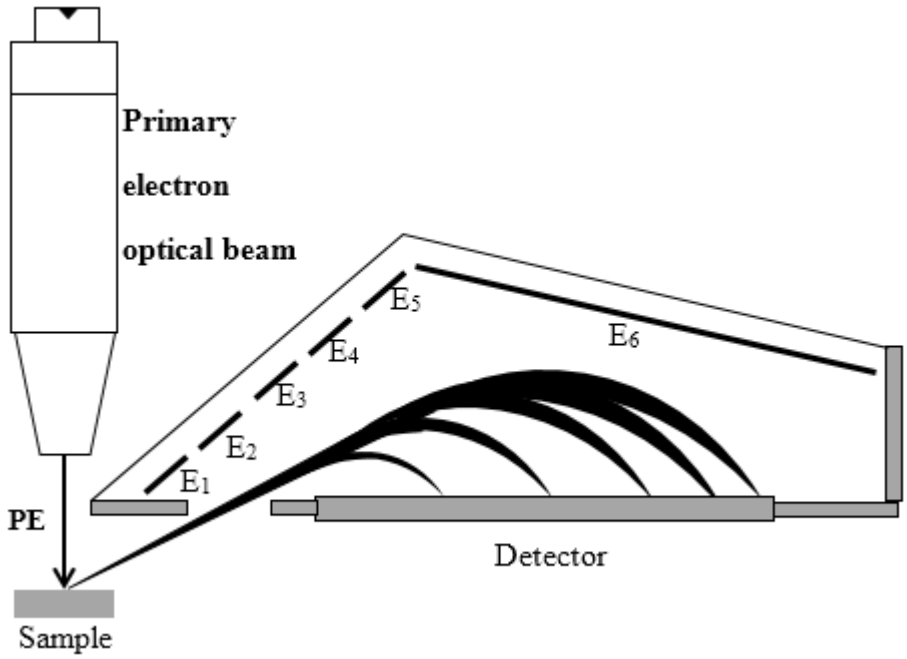

Figure 1.14: A schematic diagram of a HFA.

A widely used parallel mass spectrometer in SIMS using electric/magnetic sector fields is the Mattauch-Herzog design, as shown in Figure 1.15. This geometry consists of a cylindrical electrostatic sector analyser that forms a parallel beam of ions initially diverging from a point object at the optic axis, and a 90º deflecting homogeneous sector magnet with the straight exit boundary inclined at an angle of 45º with respect to the profile plane normal to the optic axis as shown in Figure 1.15. Because of such a configuration, after passing through the sector magnet, ions over a wide range of masses are focused at different positions on the exit boundary with the double focusing property, achieved along a straight detection.

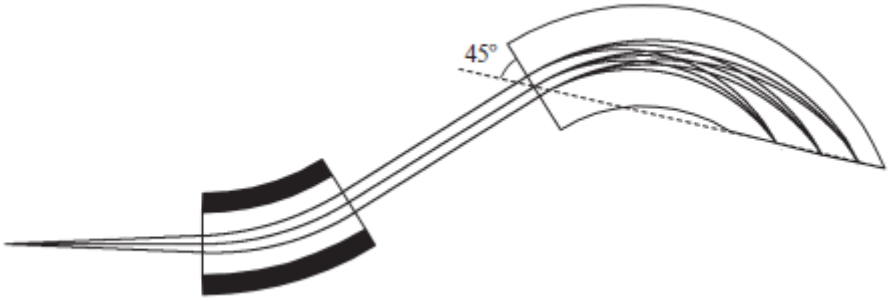

Figure 1.15: Ion trajectories with three different initial directions in the dispersion plane and three different masses in a Mattauch-Herzog type mass analyser [1.27].

The CAMECA Nano SIMS instrument utilises a Mattauch-Herzog type mass analyser, optimised for high lateral resolution analysis while maintaining high mass resolution (≈5,000). For instance, a mass resolution of 3,500 is achievable while still maintaining 100% transmission [1.25]. Figure 1.16(a) shows the schematic of the ion optics for the Nano SIMS, while Figure 1.16(b) shows the Nano SIMS system in a laboratory setting.

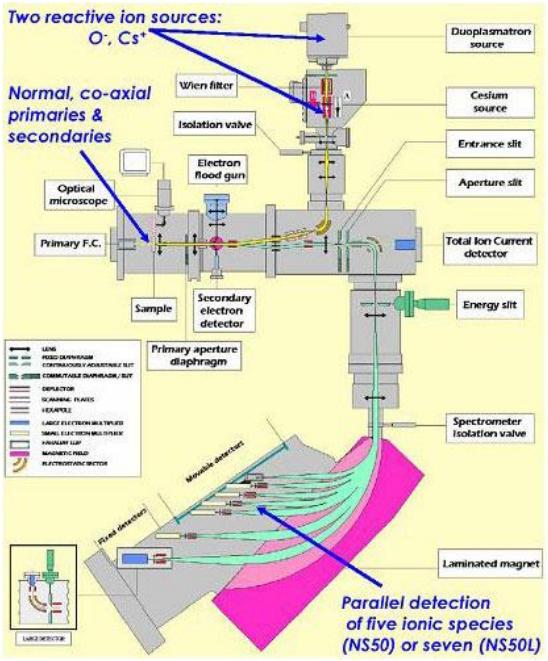

(a)

(b)

Figure 1.16: Nano SIMS manufactured by CAMECA: (a) Schematic of the ion optics for the Nano SIMS [1.36] (b) Nano SIMS in the Laboratory for Space Science, Washington University [1.37].

1.4 Multi-channel electrode array analyser designs

Khursheed proposed a parallel energy magnetic box spectrometer design [1.38]. The design is based upon the concept of using an array of permanent magnets (or electromagnets) to create a deflection field whose strength varies along the length of a simple sector magnet. The

strengths of the magnets are selected so that they create an asymmetric Gaussian-like field distribution. Simulation results predict that this kind of field distribution is able to disperse and focus scattered electrons on to a straight-edged detector lying in the plane of deflection (x-y) for emission energies that vary by more than an order of magnitude for an input angular spread ranging from -25 to 25 mrad. A schematic diagram of the magnetic sector box spectrometer design for parallel energy acquisition is shown in Figure 1.17.

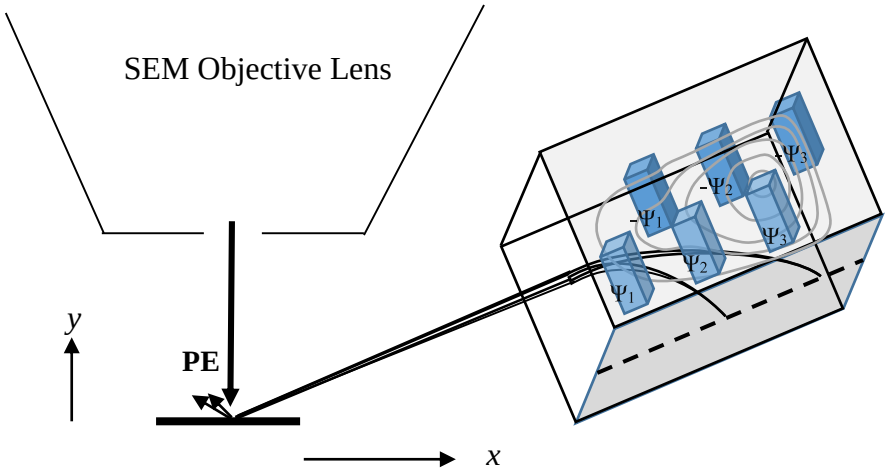

Figure 1.17: Schematic diagram of the magnetic sector box spectrometer design for parallel energy acquisition. Electrons enter the magnetic sector box spectrometer horizontally. The scalar potential contour lines are drawn on the odd-plane symmetry for illustrative purpose. Ψ_1, Ψ_2, and Ψ_3 denote magnetic scalar potentials.

Khursheed departed from the conventional method of analyser design based upon using an analytical field distribution or by altering the shape of a single sector plate. He discovered that an exact fit of the analytical field is sufficient but not necessary. He also discovered that the use of an array of sector plates provides greater flexibility and produces designs that can provide better simulated analyser characteristics than those based upon an analytical field distribution [1.39]. A larger bending angle of the electrons (with respect to the line of entry) experienced in a magnetic deflection field distribution of $B_z(x, y)$ given below was found to

produce better focusing properties. An example of this was approximately described by the field distribution:

$$B_Z(x,y) = B_0\left(\frac{y-y_1}{y_2-y_1}\right)^{1/4} \frac{1}{\left[1+\left(\frac{x-x_0}{a}\right)^2\right]} \qquad (1.1).$$

where x_1, x_2, y_1 and y_2 represent the deflection field region outer boundaries in the x-y plane, B_0 is the maximum field strength, x_0 is the position of B_0 in the x-direction, and a is a constant that controls how fast the field strength falls (in the x-direction). In the y-direction, the maximum field strength is located at $y = y_2$, the upper boundary [1.39]. Figure 1.18(a) depicts the simulated trajectory paths of electrons through the field distribution described by equation 1.1 for an input angular spread ranging from -40 to 40 mrad. Figure 1.18(b) depicts the simulated trajectory paths of electrons through a numerically solved magnetic sector box spectrometer, predicted to be better and more general than a spectrometer designed according to equation 1.1. Electrons enter the analyser at an angle of 45º to the x-axis. The analyser is predicted to have an average relative energy resolution of 0.33% (minimum of 0.147% and maximum of 0.622%) on a flat detection plane located well away from the primary electron beam axis for an input angular spread ranging from -50 to 50 mrad, where the electron energy of detection varies from 50 to 2500 eV.

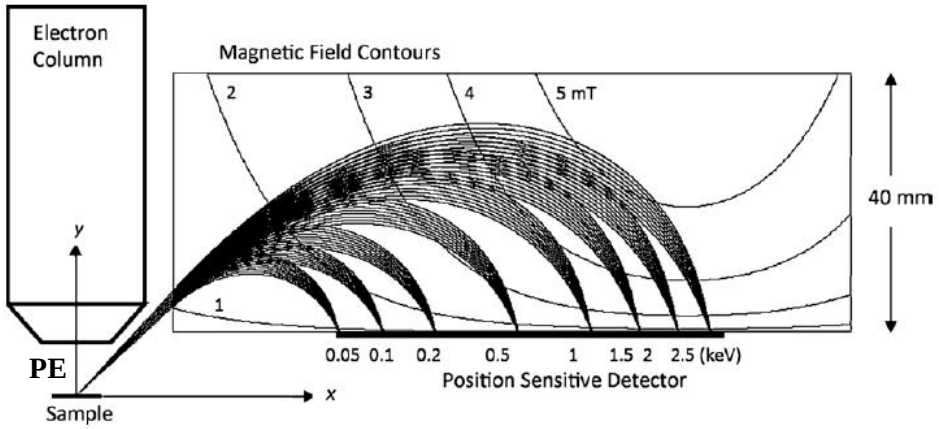

(a)

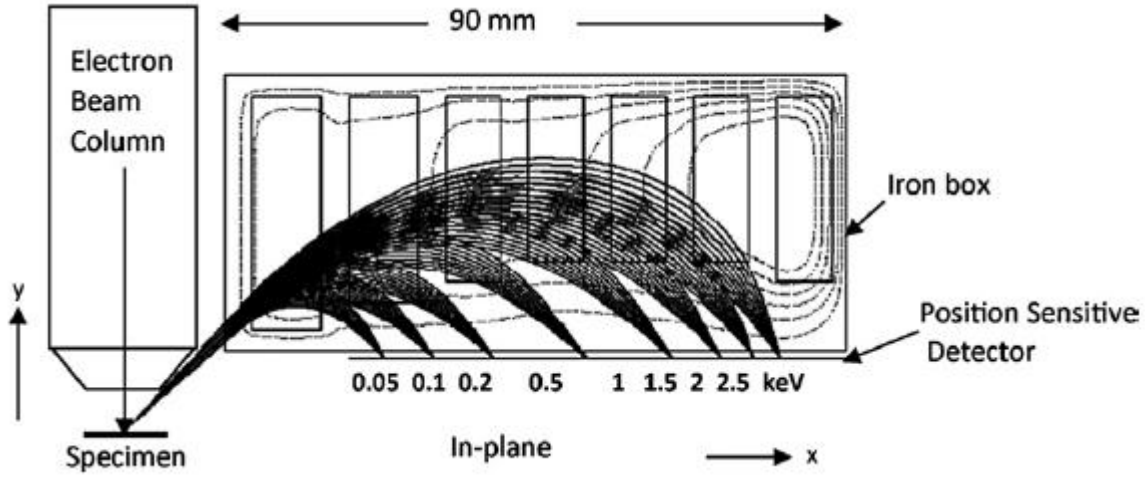

(b)

Figure 1.18: The second magnetic sector box spectrometer design for parallel energy acquisition. Electrons enter the magnetic sector box spectrometer at an angle of 45º. (a) Simulated trajectory paths of electrons through an analytically generated parallel energy analyser magnetic deflection field distribution for an input angular spread ranging from −40 to +40 mrad [1.39]; (b) Simulated trajectory paths of electrons through the numerically solved magnetic sector box spectrometer for an input angular spread ranging from −50 mrad to +50 mrad [1.39].

Khursheed's magnetic box spectrometer designs form the starting point for work to be carried out in this thesis. Several improvements in the parallel magnetic box analyser design need to be made before a practical prototype can be made. Firstly, the idealised magnetic scalar potential excitation needs to be replaced by the more realistic model using magnetic vector

potential in 3D. Secondly, the material saturation and fringe field effects at the entrance slit need to be included into the simulation. Lastly, the current rectangular box makes it difficult to fit the analyser close to the specimen within the SEM chamber due to the conical shape of the objective lens pole-piece, a sloping front entrance is required, so that it can fit around the final lens pole-piece. One objective of this thesis will be to complete these simulation model/design improvements, and then go on to make a practical prototype analyser. The main advantage of magnetic electron energy spectrometers over electrostatic ones is that they avoid the use of high voltages. However, magnetic spectrometers are only able to collect electrons emitted over a small solid angle, which limits their collection efficiency [1.40]. Since these type of magnetic box spectrometers are relatively small, one way of improving the collection efficiency is to have a box array within the SEM specimen chamber as add-on units in the azimuthal angular direction, thus providing quantitative spectral information in addition to the topographical information obtained by the SEM's existing SE and BSE detectors.

Electric field spectrometers with rotational symmetry have typically been used to increase the collection efficiency, where electrons are emitted over a 2π angular range. Recently, Khursheed et al. proposed a wide-band electric field energy spectrometer, which they referred to as the Parallel Radial Mirror Analyser (PRMA), designed to operate as an attachment for the SEM [1.23], where the energy range can vary by over a factor of 50. Electrons are plot for energies 100 to 5000 eV with 7 electron trajectories for select energies over a polar angular spread of $\pm 3^{o}$ around a central angle of 24.6^{o}, as shown in Figure 1.19. The analyser has a fully rotationally symmetric detection plane ($2\ \pi$ collection in the azimuthal direction) and is predicted to have second-order focusing properties for all electrons/ions that are detected. The starting point for the PRMA design was to use the RMA geometry, together with the HFA field distribution, and from there Khursheed et al. systematically added more electrodes and varied their voltages until second-order focusing across the entire energy range was obtained. This is

the first time that a wide-range parallel analyser is predicted to have second-order focusing across its entire energy range and can be imagined as an advanced design of a fully rotationally symmetric HFA.

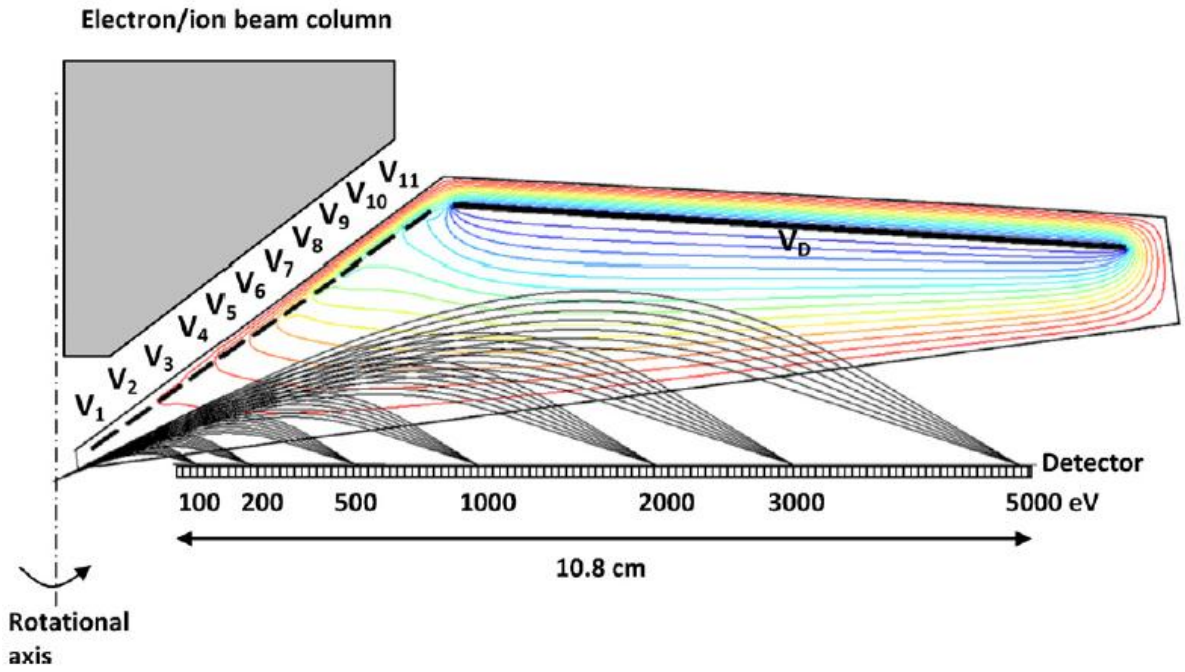

Figure 1.19: Simulated trajectory paths through a second-order focusing PRMA design. Equipotential lines plot from −176 to −2464 V in uniform steps of −176 V are also indicated [1.23].

Khursheed et al. based their predictions on the direct ray tracing of electrons through two-dimensional numerically solved field distributions using the commercial Lorentz 2EM software [1.41]. For a polar angular spread of ± 3°, the simulated energy resolution at an energy of 100 eV is around 0.65%, and it drops to less than 0.2% for energies between 300 eV to 5000 eV, a factor of around 6 times better or more than the HFA for most of its energy range. The transmittance of the PRMA is predicted to be over two orders of magnitude better than the HFA [1.23].

Although the PRMA design has significant advantages over the HFA, several challenges need to be overcome before a practical engineering design can be made for it and this will form another major theme for this thesis.

Firstly, the PRMA's current working distance, that is the distance from the specimen to the entrance of the analyser, is relatively small, only 3.5 mm, and this needs to be increased to over 5 mm in order to make room for other instrumentation that must be placed close to the specimen in the SEM chamber. This requires investigation on how the PRMA optics depends on working distance and involves substantial redesign of the analyser.

A second problem relates to the PRMA's exit grid. Khursheed et al. made their predictions for an ideal grid, that is, they modelled it to be a 100% transmission 0 volt equipotential line in their simulations. In practice, the presence of a grid will both scatter and block electrons, reducing transmission to the detector plane and adding background noise to the output signal. Moreover, it introduces fringe fields, changing the trajectory paths of electrons that travel through it, altering the final energy resolution. These effects need to be carefully analysed before a practical exit grid design for the PRMA can be made.

A third problem relates to parallel detection for the PRMA. In order to take full advantage of its inherent rotational symmetry, the PRMA requires a radial ring multi-channel detector. These kinds of detectors are at present, not commercially available. As an interim measure, a simple alternative detection system that makes use of detectors that are readily available needs to be found.

1.5 Objectives and scope of the thesis

The objectives of this thesis are to further develop the multi-channel spectrometer designs initiated by Khursheed and transform them into realistic engineering designs from which prototype analysers can be made. Chapter 2 describes the direct ray tracing simulation method by the Lorentz software, and how a Damped least-squares routine was used together with it in order to automatically optimise a large number of multi-electrode parameters within the analyser simulation. Chapter 3 describes improvements to the multi-channel energy magnetic box analyser design for the SEM, leading to the fabrication of a prototype. Chapter 4 describes the use of a multi-channel energy magnetic spectrometer design to make a multi-channel mass spectrometer design suitable for use as an add-on attachment for FIB instruments. Chapter 5 describes developments to the proposal for the PRMA, in terms of simulation designs, the making of a prototype, the development of a parallel detection system, and proof-of-principles experiments. Some suggestions for future work and the conclusions of the thesis are presented in Chapter 6.

References

[1.1] K. Wittmaack, Energy dependence of the secondary ion yield of metals and semiconductors, Surface Science, 53 (1975) 626-635.
[1.2] A.G. Fitzgerald, B.E. Storey, D.J. Fabian, Quantitative Microbeam Analysis, Taylor & Francis, 1993.
[1.3] J. Golstein, D. E. Newbury, D. C. Joy, C. E. Lyman, P. Echlin, E. Lifshin, L. Sawyer, J.R. Michael, Scanning Electron microscopy and x-ray microanalysis, 3rd edition ed., Springer, 2003.
[1.4] D. Cubric, A. De Fanis, I. Konishi, S. Kumashiro, Parallel acquisition electrostatic electron energy analyzers for high throughput nano-analysis, Nuclear Instruments and Methods in Physics Research Section A: Accelerators, Spectrometers, Detectors and Associated Equipment, 645 (2011) 227-233.
[1.5] A. Khursheed, Scanning Electron Microscope Optics and Spectrometers, World Scientific, 2011.
[1.6] E. I. Rau, V. N. E. Robinson, An annular toroidal backscattered electron energy analyser for use in scanning electron microscopy, Scanning, 18 (1996) 556-561.
[1.7] E. I. Rau, A. Khursheed, A. V. Gostev, M. Osterberg, Improvements to the design of an electrostatic toroidal backscattered electron spectrometer for the scanning electron microscope, Rev. Sci. Instrum., 73 (2002) 227-229.
[1.8] D. Berger, M. Filippov, H. Niedrig, E. Rau, F. Schlichting, Experimental determination of energy resolution and transmission characteristics of an electrostatic toroidal spectrometer adapted to a standard scanning electron microscope, J. Electron. Spectrosc. Relat. Phenom., 105 (1999) 119.
[1.9] M. Belhaj, O. Jbara, S. Fakhfakh, Quantitative voltage contrast method for electron irradiated insulators in SEM, Journal of Physics D: Applied Physics, 41 (2008).
[1.10] A. Khursheed, H.Q. Hoang, A second-order focusing electrostatic toroidal electron spectrometer with 2π radian collection, Ultramicroscopy, 109 (2008) 104 -110.
[1.11] H.Q. Hoang, M. Osterberg, A. Khursheed, A high signal-to-noise ratio toroidal electron spectrometer for the SEM, Ultramicroscopy, 111 (2011) 1093 – 1100.
[1.12] H. Q. Hoang, A. Khursheed, A toroidal spectrometer for signal detection in scanning ion/electron microscopes, Journal of Vacuum Science and Technology B, 27 (2009) 3256.
[1.13] H.Z. Sar-El, Cylindrical Capacitor as an Analyzer I. Nonrelativistic Part, Rev. Sci. Instrum., 38 (1967) 1210.
[1.14] P.W. Palmberg, G.K. Bohn, J.C. Tracy, High sensitivity auger electron spectrometer, Appl. Phys. Lett., 15 (1969) 254.
[1.15] H. Hafner, J. A. Simpson, C. E. Kuyatt, Comparison of the Spherical Deflector and the Cylindrical Mirror Analyzers, Rev. Sci. Instrum., 39 (1968).
[1.16] J.S. Risley, Design parameters for the cylindrical mirror energy analyzer, Rev. Sci. Instrum., 43 (1972) 95.
[1.17] H.Z. Sar-El, Criterion for Comparing Analyzers, Rev. of Sci. Instrum., 41 (1970) 561.
[1.18] E. Granneman, M. Van Der Wiel, Transport, dipersion and detection of electrons, ions and neutrals, chapter 6 of Handbook on Synchrotron Radiation, North Holland publishing company, 1983.
[1.19] M. Prutton, M. Gomati, Scanning Auger Electron Microscopy, John Wiley and Sons Ltd, UK, 2006.
[1.20] E. P. Benis, T. M. Zouros, The hemispherical deflector analyser revisited II. Electron-optical properties, Journal of Electron Spectroscopy and Related Phenomena, 163 (2008) 28 - 39.

[1.21] H.Q. Hoang, M. Osterberg, A. Khursheed, Experimental results from a second-order focusing electron toroidal spectrometer attachment for the scanning electron microscope, Nuclear Instrument and Methods in Physics Research A, 645 (2011) 241-244.
[1.22] A. Srinivasan, A. Khursheed, Probing and Analyzing Buried Interfaces of Multifunctional Oxides Using a Secondary Electron Energy Analyzer, Microscopy and Microanalysis, (2014).
[1.23] A. Khursheed, H.Q. Hoang, A. Srinivasan, A wide-range Parallel Radial Mirror Analyzer for scanning electron/ion microscopes, Journal of Electron Spectroscopy and Related Phenomena, 184 (2012) 525-532.
[1.24] J. Orloff, Handbook of Charged Particle Optics, Second Edition, CRC Press, 2008.
[1.25] G. V. Tendeloo, D. V. Dyck, S. J. Pennycook, Handbook of Nanoscopy, Weinheim : Wiley-VCH, 2012.
[1.26] E.G. Johnson, A.O. Nier, Angular aberrations in sector shaped electromagnetic lenses for focusing beams of charged particles, Phys. Rev., 91 (1953) 10-17.
[1.27] P.W. Hawkes, Optics of charged paticle analyzers, Academic Press, 2009.
[1.28] M. Jacka, Scanning Anger microscopy: recent progress in data analysis and instrumentation, Journal of Electron Spectroscopy and Related Phenomena, 114 (2001) 277-282.
[1.29] A. Khursheed, A.R. Dinnis, A time-of-flight voltage contrast detector for measurements on VLSI circuits, Measurement Science and Technology, 1 (1990) 581 - 591.
[1.30] P. Kruit, F.H. Read, Magnetic field paralleliser for 2p electronspectrometer and image magnifier, Journal of Physics E: Scientific Instruments, 16 (1983) 313 - 324.
[1.31] M. Kienle, E. Plies, An off-axis multi-channel analyzer for secondary electrons, Nuclear Instruments and Methods in Physics Research Section A: Accelerators, Spectrometers, Detectors and Associated Equipment, 519 (2004) 325 - 330.
[1.32] X. Zha, C.G.H. Walker, M.M. El-Gomati, A magnetic electron energy analyser for fast data acquisition, Nuclear Instruments and Methods in Physics Research Section A: Accelerators, Spectrometers, Detectors and Associated Equipment, 645 (2011) 257-259.
[1.33] M.M. El Gomati, C.G.H. Walker, X. Zha, Towards quantitative scanning electron microscopy: Applications to nano-scale analysis, Nuclear Instruments and Methods in Physics Research Section A: Accelerators, Spectrometers, Detectors and Associated Equipment, 645 (2011) 68-73.
[1.34] M. Jacka, M. Kirk, M.M. El Gomati, M. Prutton, A fast, parallel acquisition, electron energy analyzer: The hyperbolic field analyzer, Review of Scientific Instruments, 70 (1999) 2282.
[1.35] M. Jacka, A. Kale, N. Traitler, Hyperbolic field electron energy analyzer with second order focusing, Review of Scientific Instruments, 74 (2003) 4298.
[1.36] NanoSIMS 50/50L, in: Cameca (Ed.), http://www.cameca.com/instruments-for-research/nanosims.aspx.
[1.37] CAMECA NanoSIMS, in: http://presolar.wustl.edu/laboratory_for_space_sciences/NanoSIMS_50.html, Laboratory for Space Science Washington University.
[1.38] A. Khursheed, K. Nelliyan, F. Chao, First-order focusing parallel electron energy magnetic sector analyzer designs, Nuclear Instruments and Methods in Physics Research Section A: Accelerators, Spectrometers, Detectors and Associated Equipment, 645 (2011) 248-252.
[1.39] A. Khursheed, Design of a parallel magnetic box energy analyzer attachment for electron microscopes, Journal of Electron Spectroscopy and Related Phenomena, 184 (2011) 57-61.
[1.40] D.C. Joy, The basic principles of electron energy loss spectroscopy, in Introduction to analytical electron microscopy, Plenum Press, New York and London, 1979.
[1.41] Lorentz-2EM, Integrated Engineering Software Inc., Canada, 2011.

Chapter 2 : Direct ray tracing simulation methods and least-squares optimisation

2.1 Introduction

Computer simulation enables one to study various problems which are intractable analytically, highly non-linear, or for which it is cumbersome to perform experiments to verify the design. Recently, Khursheed introduced a more general numerical simulation approach to designing and optimising analysers, in contrast to the traditional approach of deriving analyser designs from analytical formulas for the field distribution [2.1]. His approach consists of numerically solving for the field distribution and using direct ray tracing of electrons/ions to determine their trajectory paths through the analyser. There are several charged particle optics simulation software which can do this, the software used for all simulation done in this thesis are the Lorentz 2/3-EM (Electric/Magnetic) field versions of the commercial program called Lorentz, written and made available by the company, Integrated Engineering Software [2.2, 2.3].

Lorentz 2/3-EM is a hybrid software that combines boundary element and finite element methods (BEM and FEM) to solve for electrostatic and magnetic field distributions in 3D. Complicated magnetic circuits will require special treatment and the FEM module is formulated in terms of the magnetic vector potential, which takes into account properties of materials, magnetic saturation and even fringe field effects at complex boundary shapes (eg. entrance slit of the spectrometer). For 2D and 3D electrostatic problems, the BEM solves for the equivalent charge distribution on electrode boundaries with a finite number of segments [2.4]. A method of adaptive segment allocation is used, where the number of segments vary according to the local electric field strength, more segments are allocated to areas of greater electric field strength. This method saves on memory and computation time when improving on the accuracy of the field distribution solution, and is particularly well suited to problems

that have strong localised field regions.

In Lorentz, the FEM and BEM techniques are coupled together and can be utilised according to their relative strengths. For instance, FEM may be more appropriate when it comes to non-linear field solutions, such as those that arise in the presence of magnetic saturation. A 5th order Runge–Kutta method variable-step method is used for direct ray tracing of charged particle trajectories, where the trajectory step is adjusted according to the local truncation error, so that it is automatically reduced in regions of high field strength and increased in regions of low field strength.

The accuracy of all simulations were continually checked by repeating all results with smaller boundary segments and trajectory step sizes, ensuring that important ray tracing parameters, such as the final focal spot-size of the electron beam at the spectrometer exit did not change significantly (by less than 1%). Apart from estimating the energy resolution visually by observing simulated electron ray paths around the focal plane, it was calculated numerically from trace-width and energy dispersion characteristics along the detection plane as a function of electron energy. Finally, the commercial software, Lorentz has a user-friendly interface with CAD tools that allows for designing complex boundaries.

The multi-channel electron energy spectrometer designs that are developed in this thesis are composed of an array of electrodes/magnets whose voltage/excitation strengths need to be changed and optimised. A small change in the array or other parameters in the design may lead to a good result in one part of the analyser, and an undesired effect in another part. Some form of optimisation method is required. Optimisation methods can be broadly classified into 2 groups: (1) classical optimisation methods which include the Damped least-squares (DLS)

method, the Gauss-Newton algorithm (GNA) and the method of gradient descent, and (2) modern optimisation methods based on analogies found in nature, like the genetic algorithm (GA) [2.5]. In the following work, a Damped least-squares (DLS) module was developed for the Lorentz software and found to converge reliably. The optimisation program was written in Python, to optimise for key parameters in the spectrometer design, such as achieving a horizontal flat output focal (detection) plane, and/or minimising the average output relative energy resolution on the detector plane over a wide energy range. In principle, the optimisation program can also be integrated with other charged particle optics simulation software.

The DLS method was successfully applied in optimising the focusing properties of various multi-channel electron energy spectrometer designs, such as the Khursheed parallel energy magnetic box spectrometer [2.6] and electric Parallel Radial Mirror Analyser (PRMA) [2.7]. The results are promising and demonstrate that the DLS method is a powerful supplement to accurate direct ray tracing for multi-channel spectrometer design, especially for the designs where the analyser is made up of a large array of electrodes/excitation plates (say, over ten), in which manual optimisation is impractical.

2.2 Principles of the Damped least-squares (DLS) method

The DLS method had previously been used by Munro and Chu in the subject of optimisation of electron optical systems for electron beam lithography [2.8]. Suppose we have a system consisting of m dependent variables Y_i and n independent variables X_i. For each dependent variable, there is a target value that we wish to achieve. The difference between each dependent variable and their target value is defined as ε_i, also known as the errors. The sum of the squared errors ϕ, is given in terms of an error function, $\phi = \sum_{i=1}^{m} \varepsilon_i^2$. The DLS method starts by defining a merit function,

$$\varphi = \phi + \lambda |\Delta X|^2 \qquad (2.1)$$

which is to be minimised. λ is known as the damping factor and ΔX is the required change to be made to the independent variables X in the system such that φ is minimised. It is clear from equation (2.1) that the damping factor prevents the change factor ΔX from growing too large. The new values of the variables are then used as a starting point for another iteration in the optimisation procedure; in this way, the solution proceeds iteratively until the optimum design is achieved. More details on the DLS method can be found in [2.8, 2.9]. The DLS method works by interpolating between the GNA and the method of gradient descent, depending on the choice of damping factor. The damping factor provides the DLS method with much more robustness than the GNA, whilst being faster than the gradient descent method.

2.3 Implementation details of the DLS method optimisation program

Figure 2.1 shows the flow diagram of the optimisation program starting from the first iteration to the end of the optimisation process. The lack of scripting option in Lorentz to support the iterative nature of DLS has been overcome by the Graphical User Interface (GUI) automation

library in Python. The full capability of the optimisation program, together with details of the GUI automation library can be found in Appendix A.

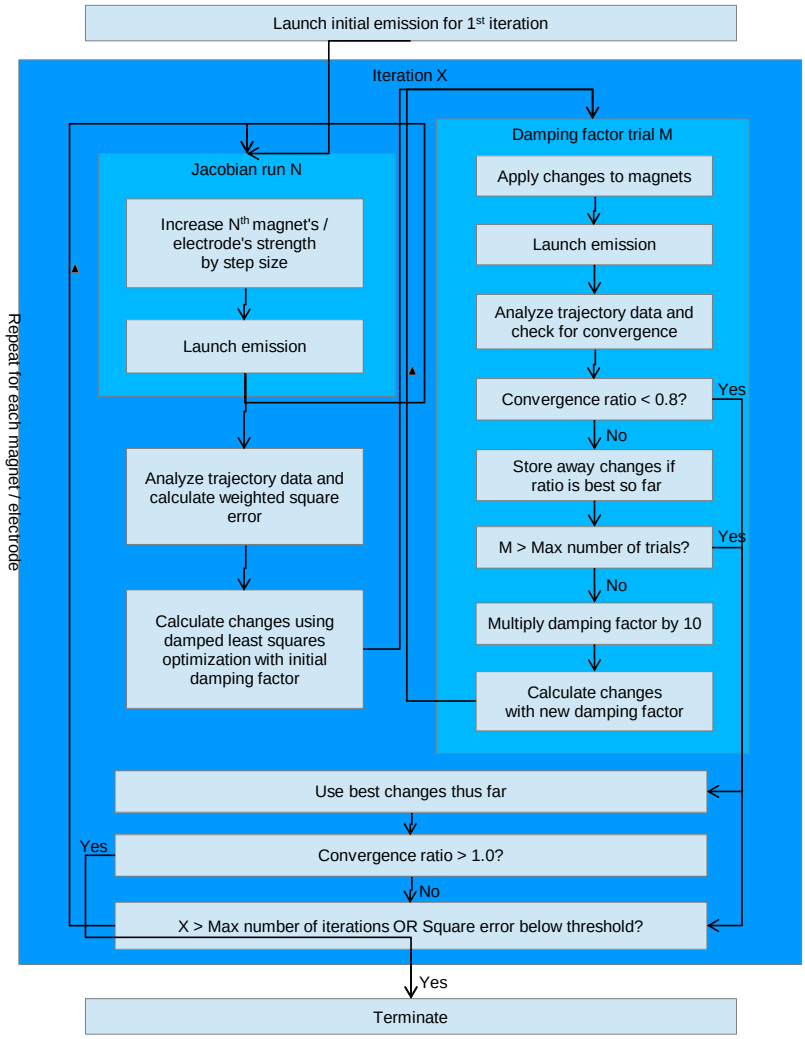

Figure 2.1: Flow diagram of the DLS optimisation program. An example is given here in optimising a parallel energy magnetic spectrometer.

2.3.1 An illustrative example

In this section, some results obtained with the optimisation program will be presented. The radial mirror analyser (RMA) [2.10] was chosen as an illustrative example due to its simple design. The RMA is designed to be an add-on energy analyser for the SEM, and functions by

creating a rotationally symmetric electric retarding mirror field, like the well-known fountain spectrometer [2.11]. However, it makes provision for a central conical shaped field-free region, whose walls have a tilt angle of 45º, in which the pole-pieces/electrodes of an objective lens can fit, and through which a focused primary electron beam can pass [2.10]. The analyser rotationally symmetric electric field distribution transports electrons/ions emitted from a central point source in a radial direction on to a ring-shaped collection/detection area, as shown in Figure 2.2.

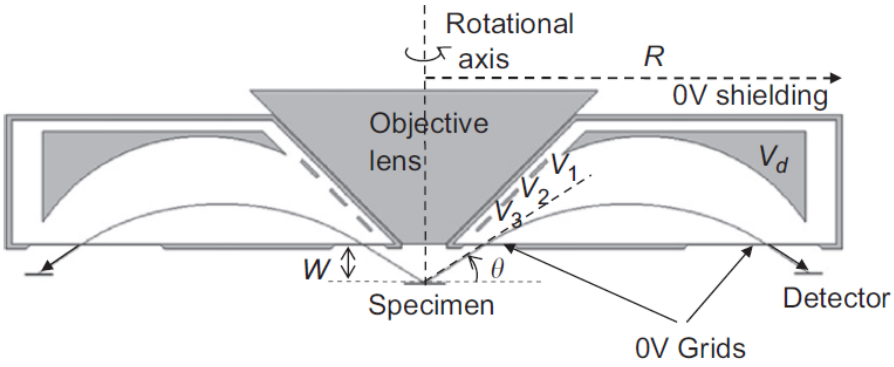

Figure 2.2: Schematic diagram of a simulated radial mirror analyser (RMA) for use inside the SEM. The segmented electrodes are biased by V_1, V_2, and V_3, and the top curved deflecting electrode is biased at V_d. Parameter W defines the working distance between the primary beam and the specimen [2.10].

Instead of the main top deflector (at voltage V_d) having a concave curved shape (in the cross-sectional plane) as shown in Figure 2.3(a) [2.10], Khursheed et al. have modified it to consist of two straight segments shown in Figure 2.3(b) [2.7].

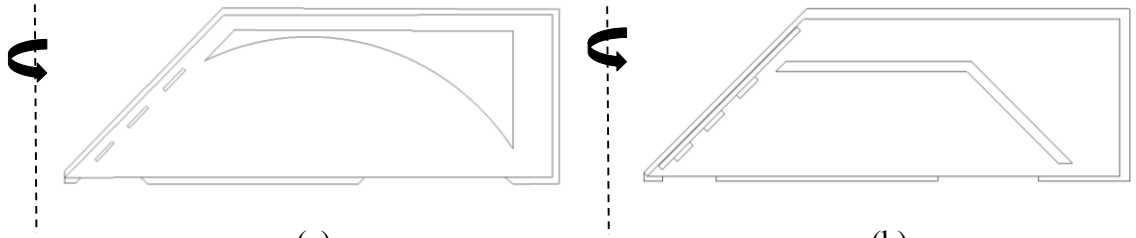

Figure 2.3: Schematic diagram of a simulated radial mirror analyser (RMA). (a) Layout of the initial RMA design [2.10] (b) Layout of the modified RMA design [2.7].

After modifying the layout of the initial RMA design, the DLS method was used to find new electrode voltage values, V_1, V_2, V_3, and V_d (in order to minimise the average energy resolution at the detector plane). For no change in the electrode voltages, simulation results indicate that the relative energy resolution is approximately 0.030% (degraded from 0.025%). Figure 2.4 shows the simulated ray paths through the analyser for an angular spread of ±6º at the energies of $E_p-0.1\%E_p$, E_p and $E_p+0.1\%E_p$, where E_p is the pass energy of the analyser.

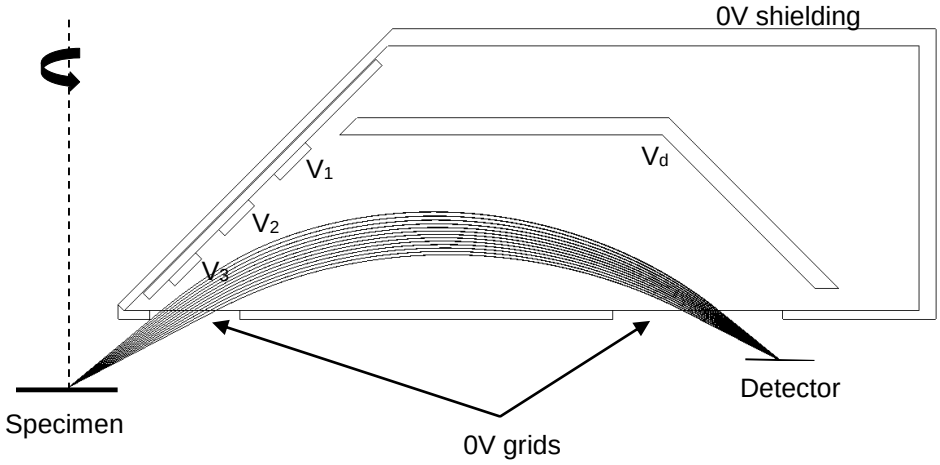

Figure 2.4: Simulated ray paths of electrons through the modified RMA at $E_p-0.1\%E_p$, E_p and $E_p+0.1\%$ E_p, where E_p is the pass energy of the analyser. The central ray enters the analyser at 32.6º and 13 trajectories are plot over uniform steps for an input angular spread varying from -6º to +6º. The layout had been modified to consist of two straight segments instead of a concave curved shape but analyser conditions of V_1, V_2, V_3, V_d = $-0.571E_p$, $-0.406E_p$, $-0.172E_p$, and $-0.571E_p$ respectively were retained from the previous model.

The simulated relative energy resolution is monitored by numerically calculating the trace-width and energy dispersion characteristics along the detection plane. The set of relative energy resolution values, each corresponding to particular energy, is represented as a vector **Y**, and it is the sum of squares of the members of this vector, ΣY_i^2, that DLS optimization seeks to minimise. In the case of this simple example, only three energies are required, $E_p - 0.1\%E_p$, E_p and $E_p + 0.1\% E_p$, so the vector **Y** will has 3 entries. For the more general case of multi-channel analysers, the number of entries in **Y** will be set to the number of energy channels in the analyser.

In order to perform optimisation, the Jacobian matrix **J** of the system must first be determined, where the independent variables are the voltages of the 4 electrodes of the RMA, represented as a vector **X**, such that in the local linear approximation, $\mathbf{Y}-\mathbf{Y}_0 = \mathbf{J}(\mathbf{X}-\mathbf{X}_0)$, where $\mathbf{Y}_0$ and $\mathbf{X}_0$ are the initial values of **X** and **Y**. This process is done by tracing electron trajectory paths through the RMA model multiple times, each time modifying the model from the original one by increasing the voltage of one of the electrodes, X_j, by a small fixed step size, δ. The corresponding change in the simulated energy resolutions is then monitored, $\Delta Y_i = Y_{i,modified} - Y_{i,original}$, where $Y_{i,modified}$ is the value after the RMA model has been modified and $Y_{i,original}$ is the value before it was modified. The partial derivative is then computed using $\partial Y_i/\partial X_j \approx \Delta Y_i / \delta$. By repeating this for all *i* and *j,* the Jacobian matrix is determined.

Once the Jacobian matrix is known, the DLS algorithm gives us the appropriate changes to be made to the independent variables (i.e. the electrode voltages) in order to minimize ΣY_i^2, represented as the change vector $\Delta\mathbf{X} = (\mathbf{J}^T\mathbf{J} + \lambda)^{-1}\mathbf{G}_0$, where λ is the damping factor, and $\mathbf{G}_0$ is the initial gradient vector given by $\mathbf{G}_0=\mathbf{J}^T\mathbf{Y}_0$. There is no single method for choosing the damping factor and every design program has its unique way of choosing optimum damping

conditions, which makes each program different from the others [2.12-2.14]. Although the principal use of the damping factor is to accelerate convergence by limiting the magnitude of the change vector, the damping factor can also be used to increase the magnitude of the change vector to escape a local minimum. During the course of minimisation, if the solution stagnates, the program attempts to force the solution into another region by running one or more iterations with reduced damping in which the error function increases. In general, setting λ to higher values results in slower convergence, but provides more stability [2.9]. The calculated changes are then applied to the model by modifying the voltages of the electrodes, and the whole process is repeated, iteration after iteration, until there is no further improvement to the focusing properties of the analyser.

Figure 2.5 shows results of using the DLS method to find the optimal electrode voltages in the RMA design for the modified more practical construction of the top deflector (V_d) shown in Figure 2.3b. The results are given in terms of the output relative energy resolution improving with iteration number. The corresponding analyser conditions are given in Table 2.1.

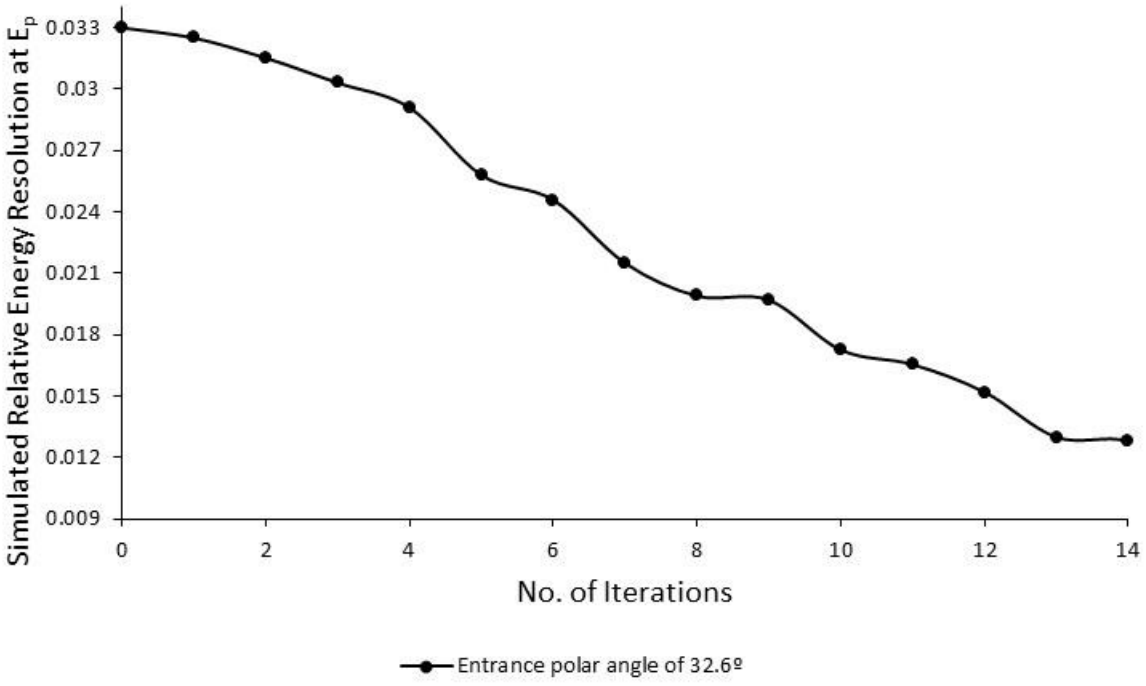

Figure 2.5: The central ray enters the modified RMA at 32.6º at the pass energy of the analyser, E_p for an input angular spread varying from -6º to +6º.

Emission Angle	**Central ray of 32.6°±6°**
V_1	-0.1715 E_p
V_2	-0.4602 E_p
V_3	-0.5700 E_p
V_d	-0.5360 E_p

Table 2.1: Optimised parameters corresponding to the central ray of 32.6º at the pass energy of the analyser, E_p for an input angular spread varying from -6º to +6º.

Apart from finding the optimal electrode voltages for changes in the analyser electrode geometry, the DLS method can also to determine optimal conditions for variations in the entrance polar angle. Better analyser optics is often obtained by allowing the entrance angle to change. Three different polar emission angles for the central ray were selected, 32.4º, 33.4º and 34.4º. Figure 2.6 shows similar analyser optics is predicted for these three different conditions after applying DLS optimisation. The corresponding analyser conditions are given in Table 2.2.

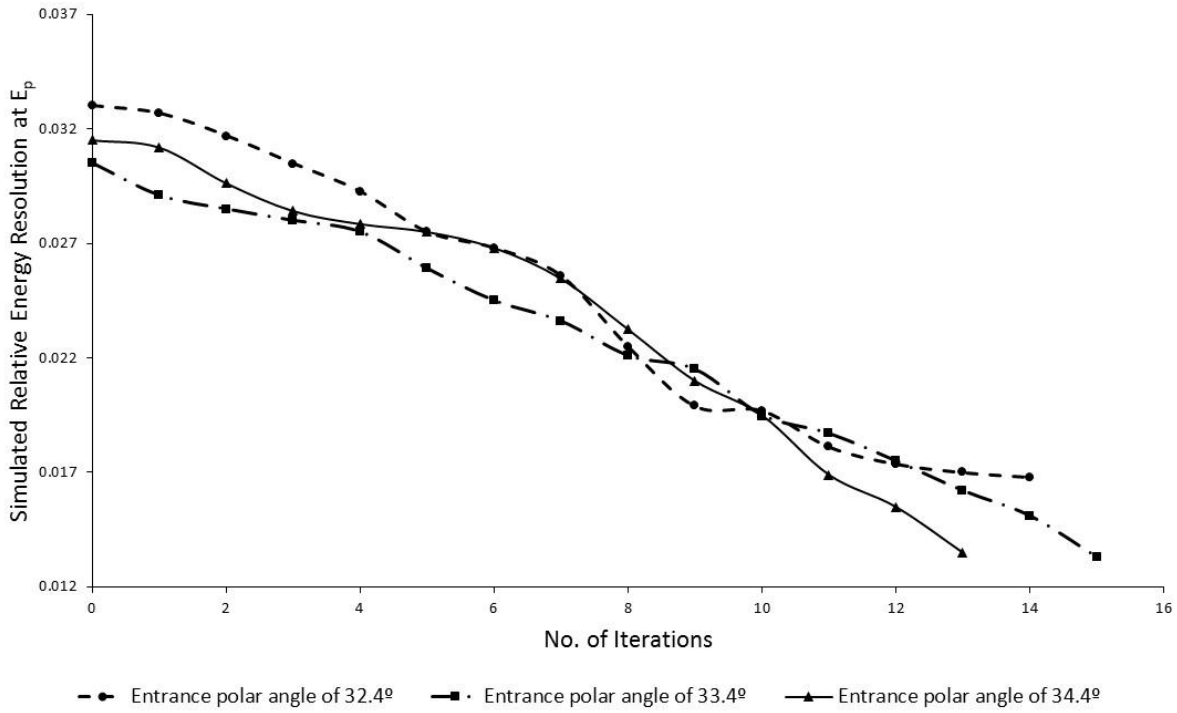

Figure 2.6: The central ray enters the modified RMA at 3 different emission angles of 32.4º, 33.4º and 34.4º at the pass energy of the analyser, E_p for an input angular spread varying from -6º to +6º.

Emission Angle	**Central ray of 32.4°±6°**	**Central ray of 33.4°±6°**	**Central ray of 34.4°±6°**
$\mathbf{V_1}$	-0.1725 E_p	-0.1720 E_p	-0.1742 E_p
$\mathbf{V_2}$	-0.4696 E_p	-0.4711 E_p	-0.4699 E_p
$\mathbf{V_3}$	-0.5700 E_p	-0.5702 E_p	-0.5699 E_p
$\mathbf{V_d}$	-0.5401 E_p	-0.5405 E_p	-0.5396 E_p

Table 2.2: Optimised parameters corresponding to the central ray of 32.4º, 33.4º and 34.4º at the pass energy, E_p for an input angular spread varying from -6º to +6º.

2.5 Conclusions

In this chapter, the principles of the DLS method and its application to the design and optimisation of multi-channel electron energy spectrometer have been discussed. A Python program based on this technique has been developed as a module for Lorentz 2/3 EM programs. The program has been used to optimise a simple RMA test electron energy spectrometer design, and the results show that reliable optimisation can be achieved.

References

[2.1] A. Khursheed, K. Nelliyan, F. Chao, First-order focusing parallel electron energy magnetic sector analyzer designs, Nuclear Instruments and Methods in Physics Research Section A: Accelerators, Spectrometers, Detectors and Associated Equipment, 645 (2011) 248-252.
[2.2] Lorentz-2EM, Integrated Engineering Software Inc., Canada, 2011.
[2.3] Lorentz-3EM, Integrated Engineering Software Inc., Canada, 2011.
[2.4] A. Asi, Boundary element method (BEM) for charged particle optics, Proc. SPIE 4510, Charged Particle Detection, Diagnostics, and Imaging, (2001) 138-147.
[2.5] D. Vasiljevic, J. Golobic, Comparison of the classical damped least squares and genertic algorithm in the optimization of the doublet, Proceedings of the First Workshop on Soft Computing, Nagoya, Japan, (1996) 200-204.
[2.6] A. Khursheed, Design of a parallel magnetic box energy analyzer attachment for electron microscopes, Journal of Electron Spectroscopy and Related Phenomena, 184 (2011) 57-61.
[2.7] A. Khursheed, H.Q. Hoang, A. Srinivasan, A wide-range Parallel Radial Mirror Analyzer for scanning electron/ion microscopes, Journal of Electron Spectroscopy and Related Phenomena, 184 (2012) 525-532.
[2.8] E. Munro, H. Chu, Numerical analysis of electron beam lithography systems. Part IV: Computerized optimization of the electron optical performance of electron beam lithography systems using the Damped least squares method, Optik, 61 (1982) 213-236.
[2.9] K. Levenberg, A Method for the Solution of Certain Non-Linear Problems in Least Squares, Quarterly of Applied Mathematics, 2 (1944) 164 – 168.
[2.10] H.Q. Hoang, A. Khursheed, A radial mirror analyzer for scanning electron/ion microscopes, Nuclear Instruments and Methods in Physics Research Section A: Accelerators, Spectrometers, Detectors and Associated Equipment, 635 (2011) 64-68.
[2.11] W. Schmitz , W. Mehlhorn, Parallel plate analyser with second order focusing property, Journal of Physics E: Scientific Instruments, 5 (1972) doi:10.1088/0022-3735/1085/1081/1023.
[2.12] H. Matsui, K. Tanaka, Determination method of an initial damping factor in the Damped-least-squares problem, Applied Optics, 33 (1994) 2411 - 2418.
[2.13] M. Lampton, Damping–undamping strategies for the Levenberg–Marquardt nonlinear least-squares method, Computers in Physics, 2 (1997) 110-115.
[2.14] L. Lia, C. Liua, Q. Wang, Three-step method for optimization of optical thin film, Optik - International Journal for Light and Electron Optics, 124 (2013) 1796-1799.

Chapter 3 : The parallel energy magnetic box spectrometer

3.1 Introduction

The parallel 45º entrance angle magnetic box energy analyser reported by Khursheed (described in chapter 1, shown in Figure 1.18b) [3.1] forms the starting point for the energy analyser development work to be carried out here. Although its predicted average relative energy resolution of 0.33% (minimum of 0.147% and maximum of 0.622%) is promising, a factor of around 5 better than the simulated values taken for the HFA (minimum of 1.337% and maximum of 2.246%) reported by Khursheed et al. [3.2], the numerical model used to make these predictions has several important limitations, most of which come from the use of a single magnetic scalar potential model, where the scalar potential on excitation plates define fixed boundary values. These simulation results were generated by Finite Element Programs and ray tracing programs written by Khursheed [3.3]. This means that modelling of excitation sources, whether they be in the form of permanent magnets or solenoid coils was not explicitly included in the model. Another limitation is that a scalar potential representation cannot account for saturation effects in the iron or fringe fields that exist in the analyser entrance aperture or exit slot. Additionally, the rectangular box shape of the analyser is not well suited as an add-on attachment for the SEM, it does not fit well into the relatively small space (30- 40 mm high) between the lower objective lens conical pole-piece and the specimen, necessitating the use of impractically large working distances.

The aim of this chapter is to develop a practical design and prototype of the 45º entrance multi-channel magnetic box energy spectrometer presented by Khursheed so that it can be used as an Auger electron spectroscopy (AES) attachment for SEMs, to be operated in combination with a low voltage ion flood beam. This allows quantitative spectral information to be obtained, in

addition to the topographical information provided by the SEM's existing SE and BSE detectors.

More realistic simulation of the magnetic box analyser design was carried out by use of the Lorentz 3EM [3.4] simulation program, which can solve for magnetic vector field distributions in three dimensions, taking into account the B-H curve characteristics of iron/permanent magnetics. The Lorentz 3EM software is able to calculate the fringe fields in and around small entrance/exit apertures in iron walls. The Lorentz 3EM software also has the capability of modeling a wide variety of different boundary shapes, making it possible to specify a slanted entrance analyser wall that fits into the small space under the conically shaped lower pole-pieces of the SEM objective lens. For each design variation, the DLS optimise technique was used to minimise the energy resolution over a wide energy range.

3.2 The effect of Fringe fields

The 3D schematic model for solving magnetic field distributions with the Lorentz program is shown in Figure 3.1. For the source excitation, permanent alnico magnets were modelled. Figure 3.1(a) indicates the presence of alnico magnets (rectangular blocks) of differing heights in the z-direction, only half the box is shown. Figure 3.1(b) shows the B-H curve characteristics specified for the alnico magnet.

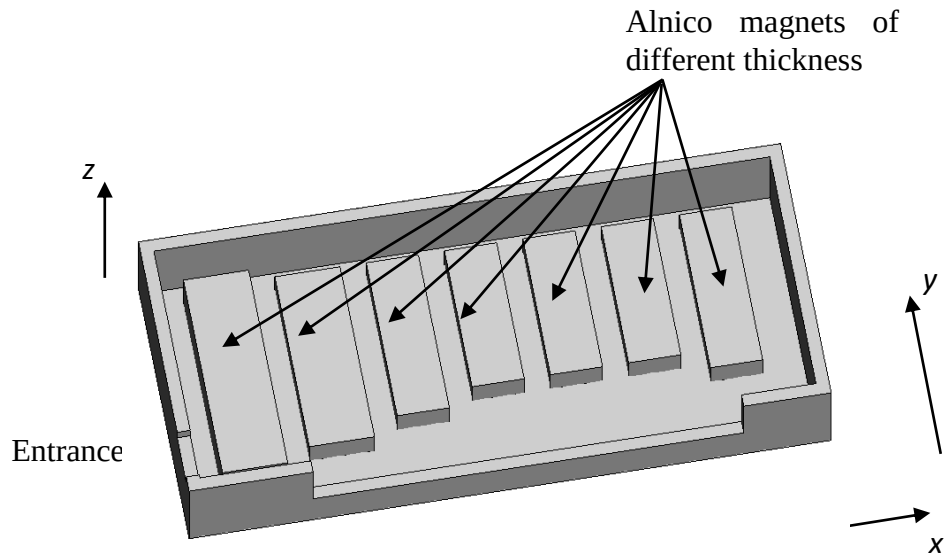

(a)

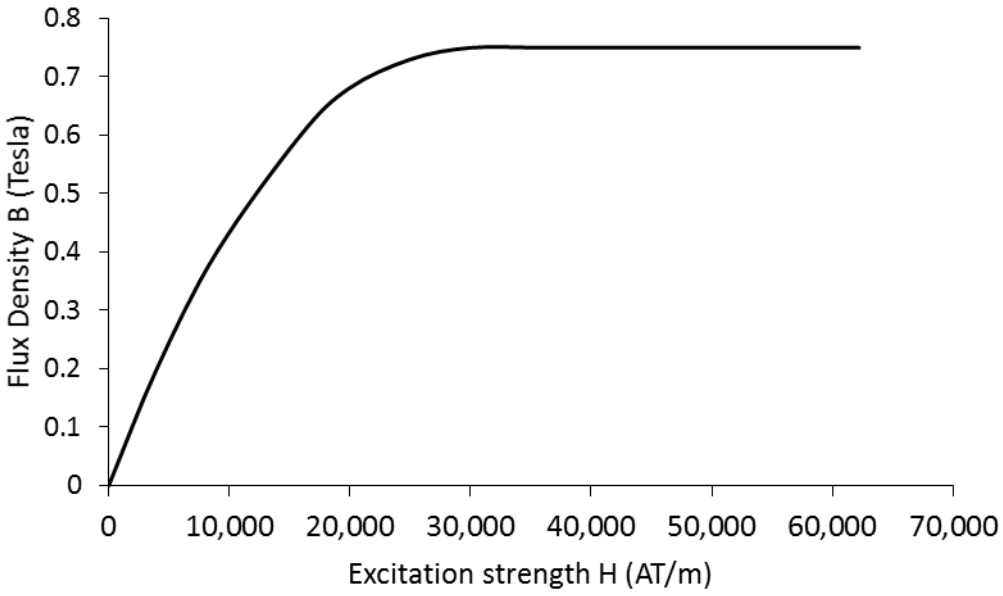

(b)

Figure 3.1: 3D simulation model for the 3D magnetic field solving Lorentz program that takes into account permanent magnet/iron B-H curve characteristics. (a) Magnetic sector box analyzer (only half of box shown in the z-direction) (b) B-H curve specified for the alnico magnet.

Figure 3.2 shows the cross-sectional diagrams of the analyser simulation model used in the 3D magnetic field solving Lorentz program.

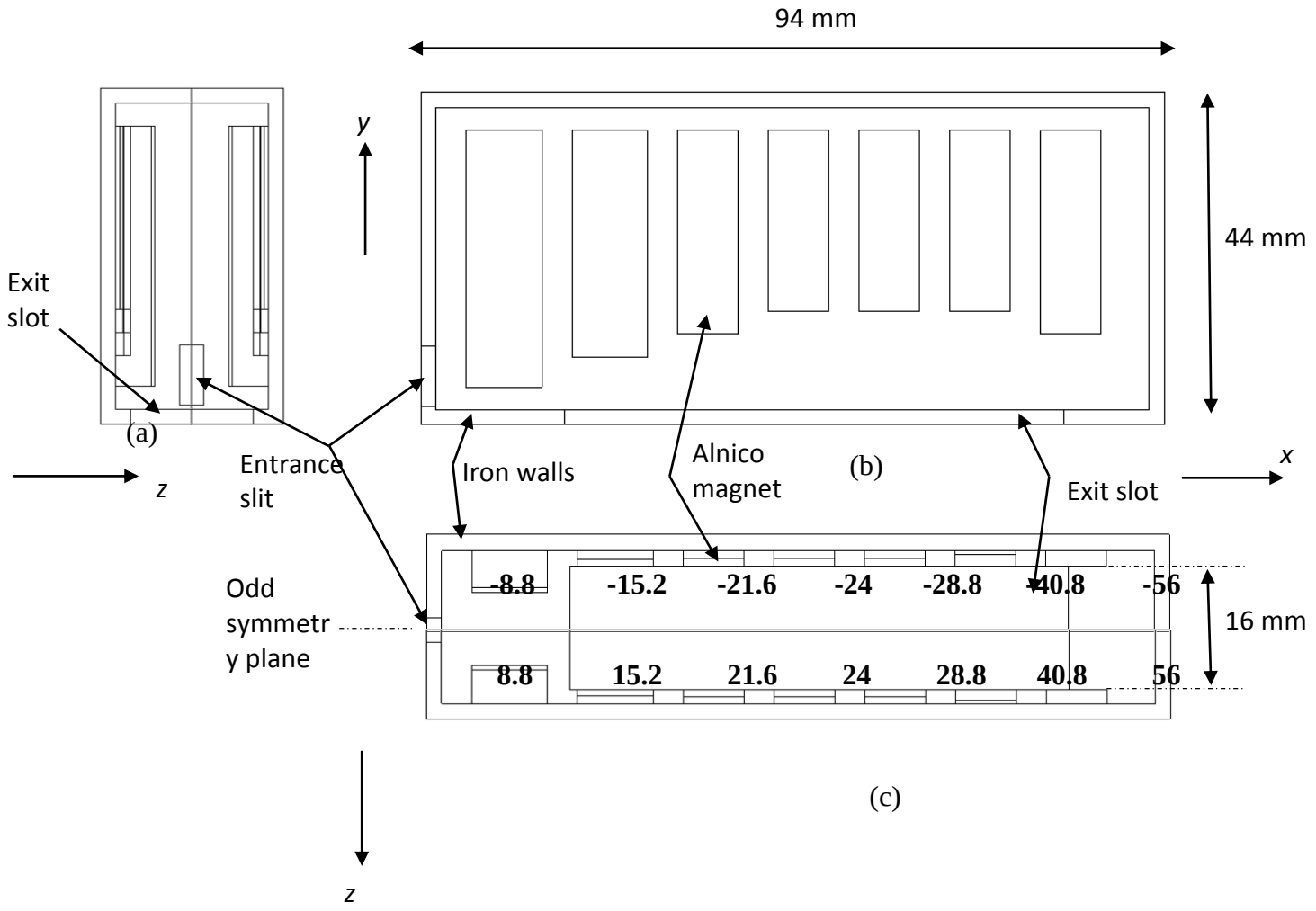

Figure 3.2: Cross-sectional diagrams of the analyser simulation model. (a) End view (y-z plane) (b) Side view (x-y plane) (c) Plan view (x-z plane)

Initial ray tracing of electrons through the parallel magnetic box analyser carried out using the Lorentz 3EM software with similar excitation strengths and geometry to the original magnetic scalar potential model [3.1] was carried out, and is shown in Figure 3.3. In keeping to the original design [3.1], an exit slot was specified at the bottom of the box. The rays are plot for electron emission energies of 50, 100, 200, 500, 1000, 1500, 2000, and 2500 eV. The central entry polar angle is 45º with respect to x-axis and the in-plane polar angular spread uniformly ranges between −50 mrad and +50 mrad.

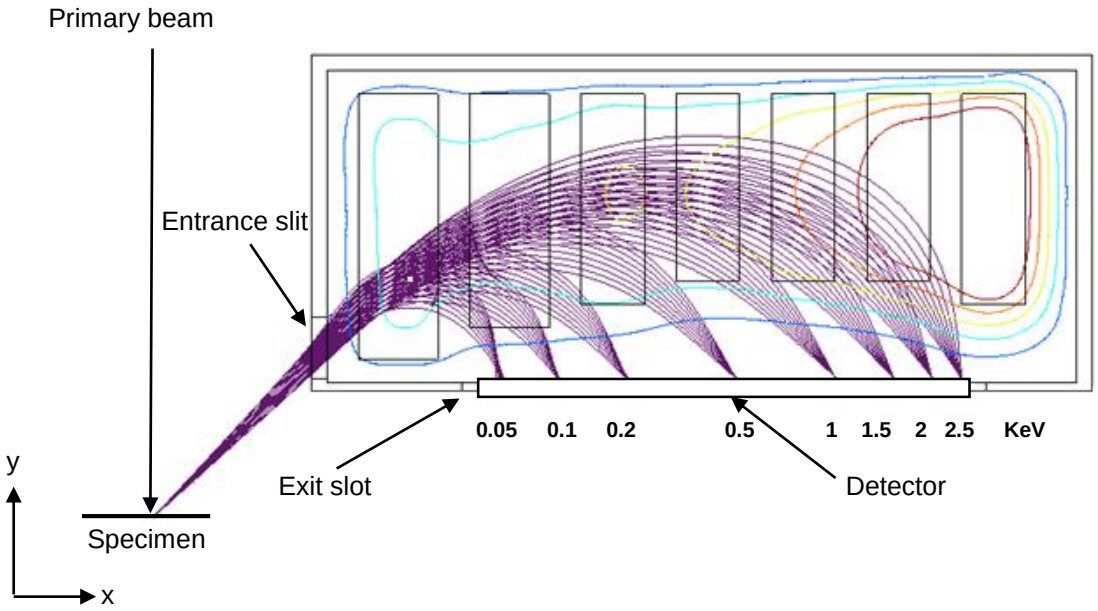

Figure 3.3: Simulated in-plane electron trajectory paths by the Lorentz 3EM software through the parallel magnetic box analyser design with an exit slot at the bottom plate. Trajectories are plot for emission energies of 0.05, 0.1, 0.2, 0.5 1, 1.5, 2 and 2.5 keV, where the polar angular spread uniformly ranges between −50 mrad and +50 mrad. Equipotential lines plot from 1.2mT to 6mT in uniform steps 1.2mT are also indicated.

A significant difference between the trajectory paths obtained by the Lorentz 3EM software and the previous magnetic scalar potential simulation occurs for the lower energy electrons (< 200 eV), which are deflected upwards as they travel through the entrance slit. Figure 3.4 shows a magnified view of the simulated electron trajectory paths shown in Figure 3.3 around the entrance slit region. These preliminary simulation results indicate the presence of a fringe field that was absent in the previous magnetic scalar potential simulations.

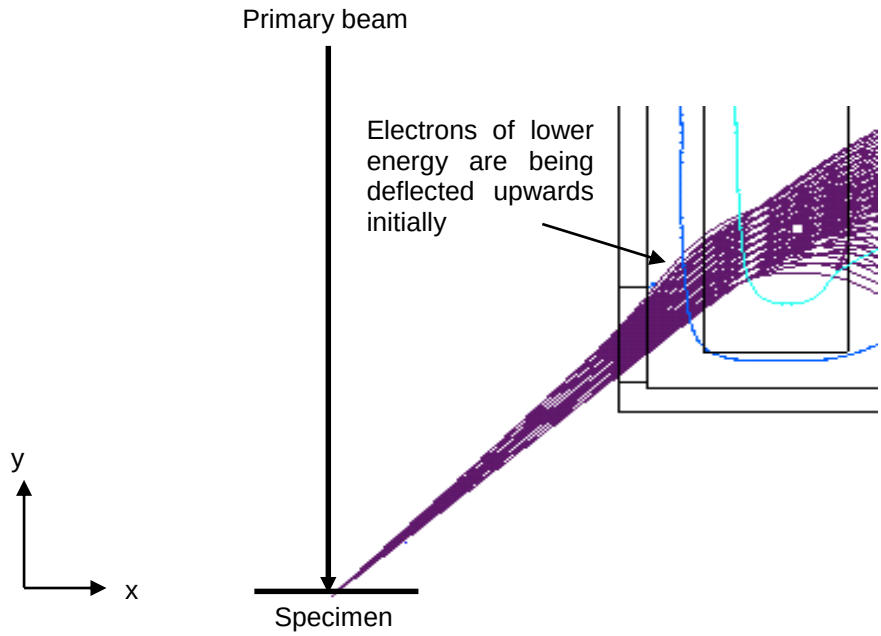

Figure 3.4: Magnified view of the electron trajectories across the rectangular entrance slit suitable for polar angular spread ranging between −50 mrad and +50 mrad. Electrons of lower energy are being deflected upwards initially.

The size of the entrance slit was systematically varied in order to quantify the effects of the fringe field on the simulated electron trajectories. Figure 3.5 shows a graph of the simulated magnetic leakage field z-component along the central ray at the mid-plane (x-y) symmetry plane as a function of x-axis for the cases of: without entrance slit (idealised case), rectangular entrance slits that define polar angular spreads of ±50, ± 60 and ±70 mrad and a parallelogram entrance slit that defines a polar angular spread of ±50 mrad. The negative leakage field is

caused by the return path of the magnetic flux in the iron walls of the analyser and the graph in Figure 3.5 predicts that the effect of magnetic leakage field is more pronounced when the size of the entrance slit is increased.

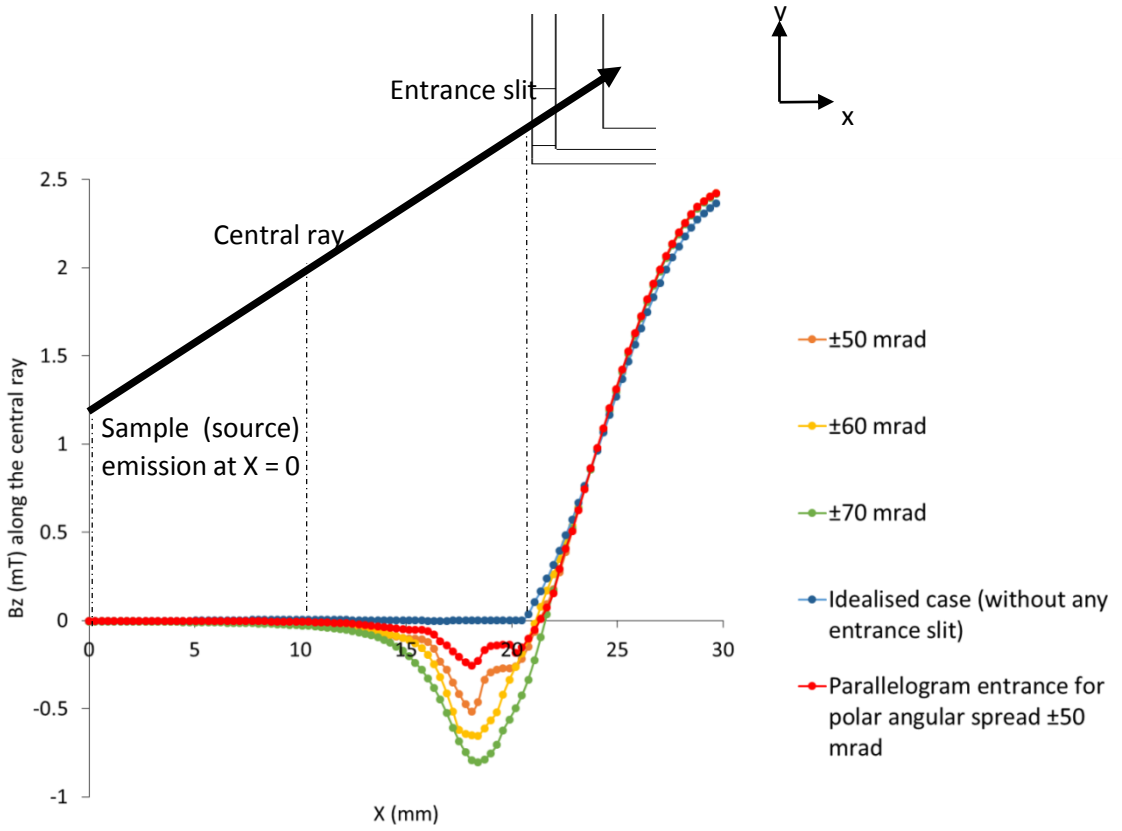

Figure 3.5: Graph of the simulated magnetic leakage field z-component along the central ray in the mid-plane (x-y) symmetry plane as a function of x-axis for the cases of: without entrance slit (idealised case), rectangular entrance slits that define polar angular spreads of ±50, ±60 and ±70 mrad and parallelogram entrance slit that defines a polar angular spread of ±50 mrad. Diagram is not drawn to scale.

A magnified view of simulated trajectory paths through the entrance slit and detector plane for the lower energy simulated electrons (50, 100 and 200 eV) with a polar angular spread of ±50 mrad is shown in Figure 3.6. This figure illustrates how the presence of fringe fields in the entrance slit causes defocusing on the detector plane for both rectangular and parallelogram slit shapes. Since the smaller parallelogram slit generates less fringe fields (Figure 3.5), it is able to provide for sharper focusing (better energy resolution), while for the case of the rectangular

slit, the fringe fields cause electrons to be deflected upwards into a higher magnetic field region, causing them to over-focus at the detection plane. The simulation model was therefore changed to incorporate a parallelogram entrance slit shape.

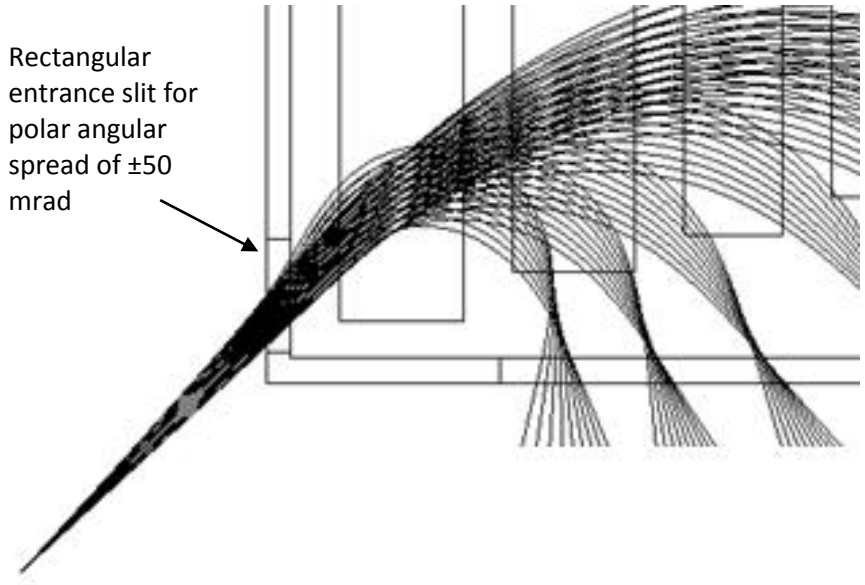

(a)

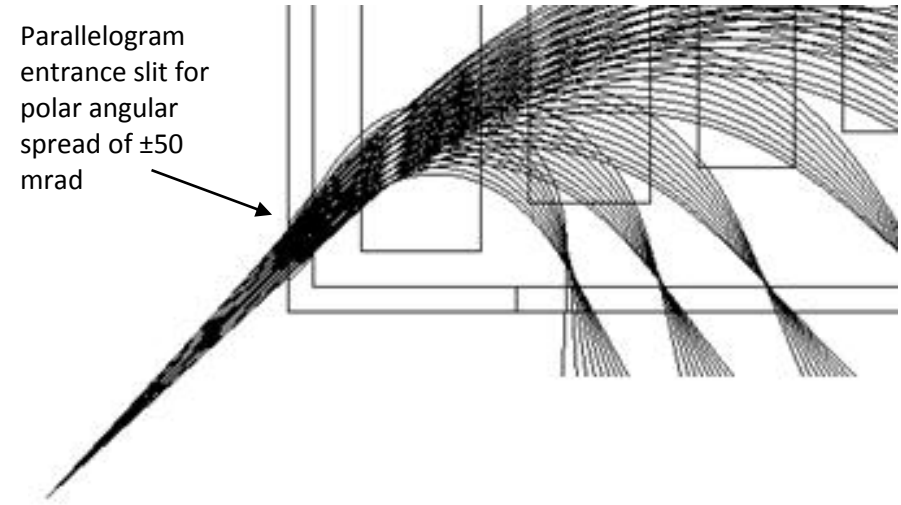

(b)

Figure 3.6: Trajectory paths for lower energy of 50, 100 and 200 eV for the case of: (a) Rectangular entrance slit that defines polar angular spreads of ±50 mrad; (b) Parallelogram entrance slit that define polar angular spreads of ±50 mrad.

Various sizes of the exit slot were investigated for their influence on the focusing properties of the analyser (including the case with no exit slot). Figure 3.7 shows the graph of the simulated magnetic leakage field z-component at a height of 5mm above the centre of the exit slot (located at the base of the box) as a function of x-axis. These initial simulation results predict that there will be a region of negative leakage field along the centre of the exit slot, which reduces as the slot width decreases.

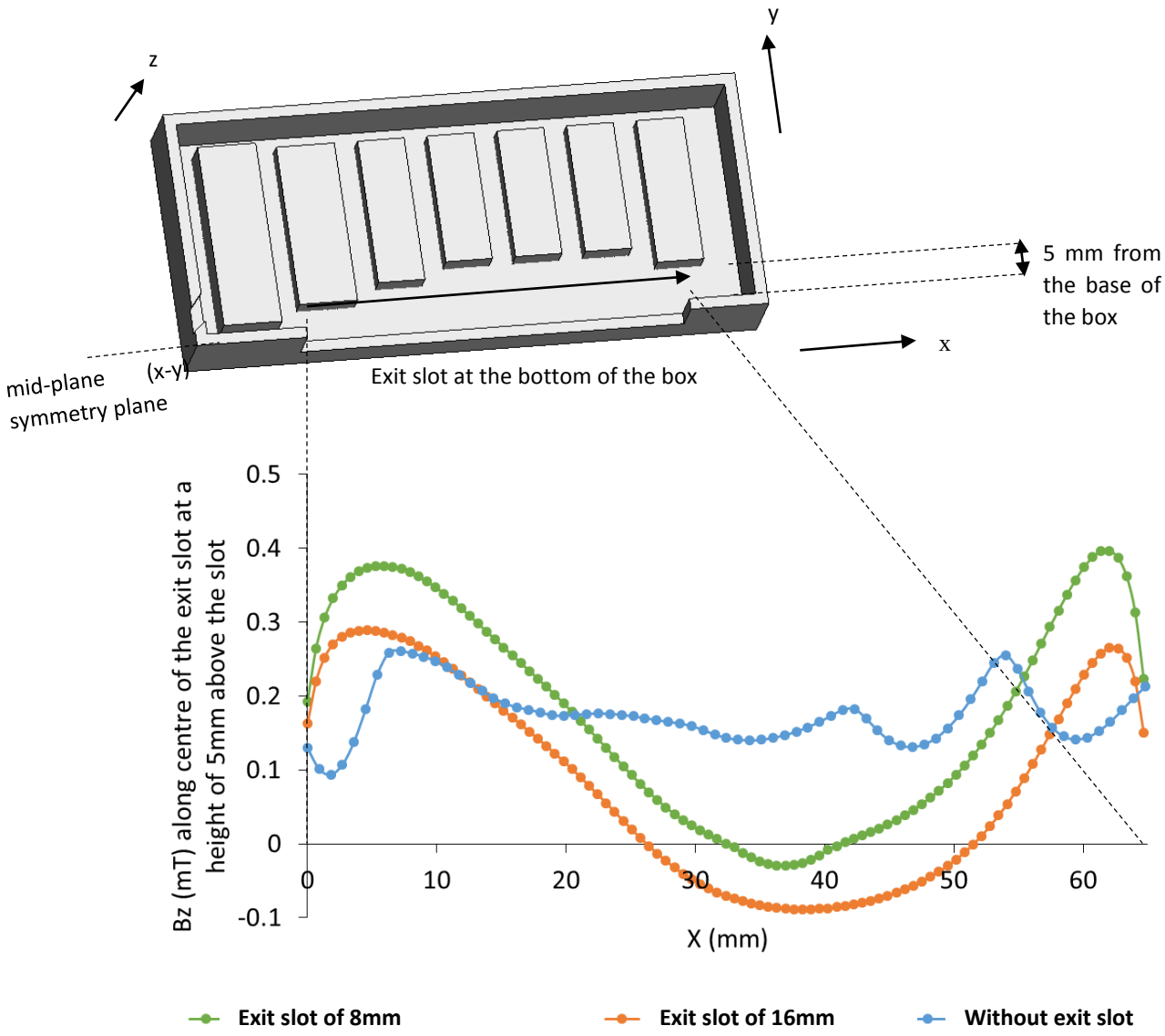

Figure 3.7: Graph of the magnetic leakage field along the centre of the exit slot at a height of 5mm above the slot (located at the base of the box) as a function of x-axis for cases of: original exit slot of width 16 mm, exit slot of width 8 mm and without exit slot. Diagram is not drawn to scale.

As electrons travel close to the exit slot, they will experience a deflection force caused by the leakage fields, which degrades their focusing properties on a horizontal detector plane. Direct ray tracing was carried out to quantify this effect and is shown in Figure 3.8. Figure 3.8(a) shows the electron trajectories through a modified parallel magnetic box analyser with no exit slot (height of the box is extended slightly by 5mm) while Figure 3.8(b) shows the box with an exit slot at the bottom plate. The emission energies are 50, 100, 200, 500, 1000, 1500, 2000, and 2500 eV. The entry polar angle is 45˚ with respect to x-axis, and the in-plane angular spread uniformly ranges between −50 mrad and +50 mrad. It can be seen from Figure 3.8 that the general shape of the resultant magnetic contours from the field distribution resemble those obtained from the previous scalar potential solution in [3.1].

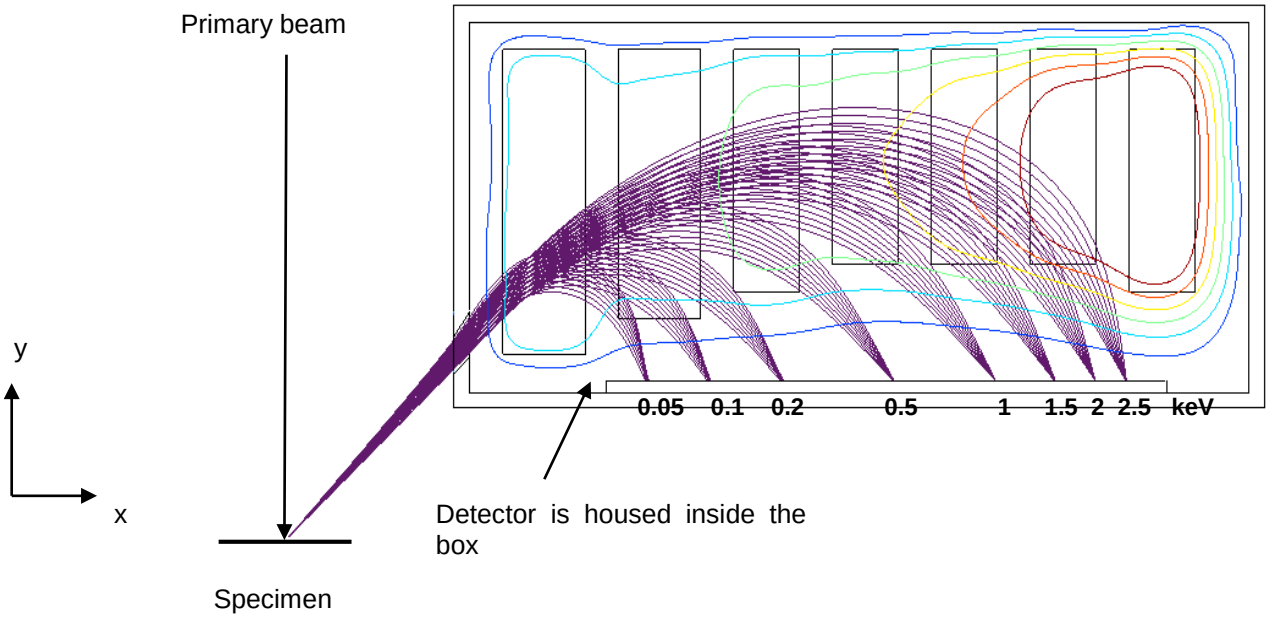

(a)

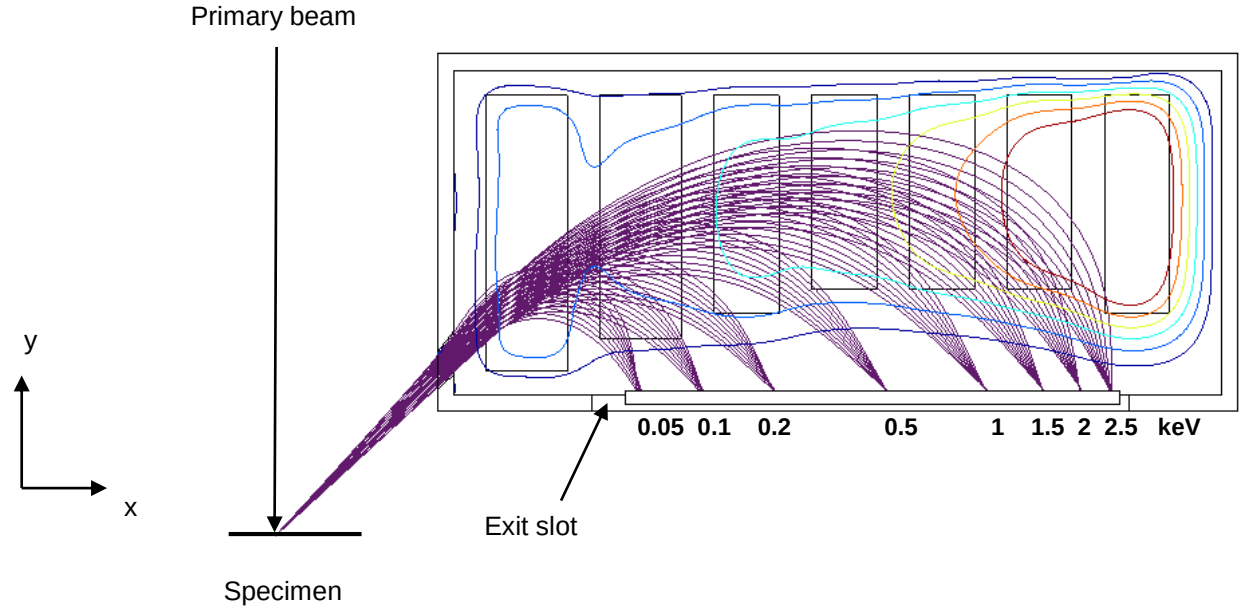

(b)

Figure 3.8: Simulated in-plane electron trajectory paths through the parallel magnetic box analyser model with the Lorentz software. Trajectories are plot for emission energies of 0.05, 0.1, 0.2, 0.5 1, 1.5, 2 and 2.5 keV, where the polar angular spread uniformly ranges between −50 mrad and +50 mrad. Equipotential lines plot from 1.2mT to 6mT in uniform steps 1.2mT are also indicated. (a) Box with no exit slot (height of the box is extended by 5mm) (b) Box with an exit slot at the base.

Figure 3.9 shows the predicted relative energy resolution on a horizontal detector plane for the parallel magnetic box analyser design without an exit hole as a function of energy as compared to the case of an exit slot at the bottom. These simulation results predict that the exit hole will have an adverse effect on the focusing properties of the analyser. In particular, the predicted average relative energy resolution for the analyser design without an exit hole, is a factor of around 1.4 better than the design with an exit hole. An improvement of up to a factor of 1.7 in terms of its relative energy resolution is observed for electron energies below 500 eV. Based upon these results, the analyser geometry has been redesigned to eliminate the need for an exit slot, where the height of the analyser is increased so that the detector can be placed within the box.

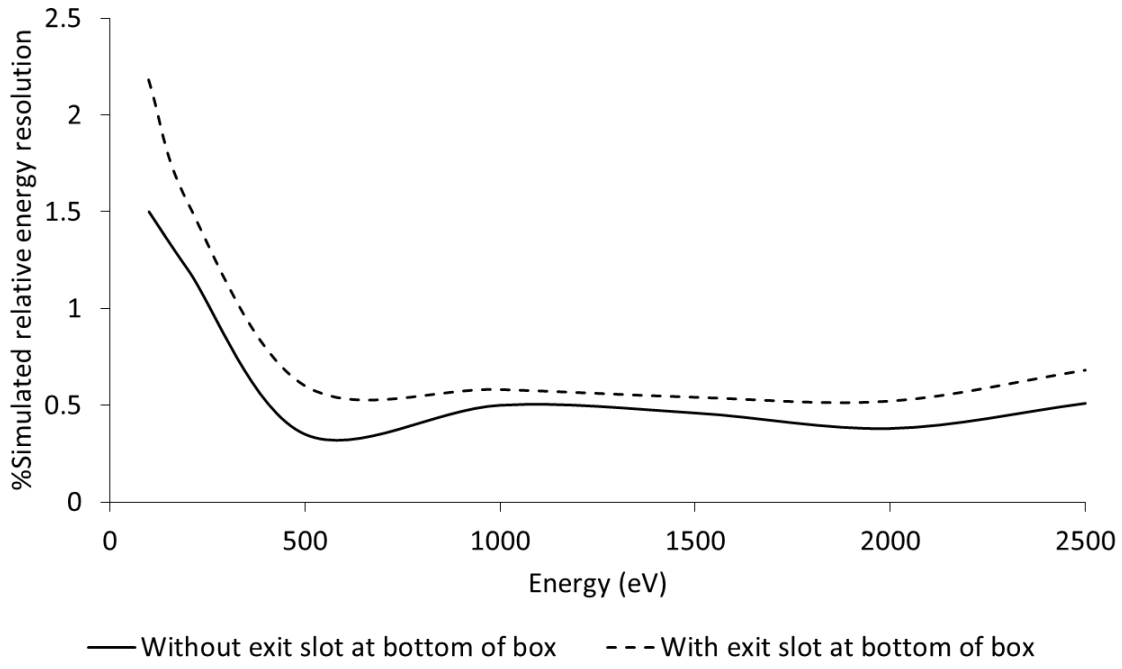

Figure 3.9: Predicted relative energy resolution of the parallel magnetic box analyser design on a horizontal detector plane as a function of energy for the case without an exit hole and with exit hole at the base of box.

3.3 Energy resolution improvements on a more practical analyser design

Redesign of the analyser box has so far been based upon using the more accurate Lorentz 3EM software to calculate fringe fields that were not predicted by the previous magnetic scalar model. These simulations have kept to the same overall geometry and relative source excitation strengths reported by Khursheed. However, in order to make further progress, more substantial changes to the analyser design are required.

The current rectangular box design makes it difficult to place the analyser close to the specimen within the SEM chamber due to the conical shape of the objective lens pole-piece. The working distance, the distance from the specimen to the objective lower pole-piece is usually less than 30mm in order to prevent the on-axis aberrations of the primary beam spot from becoming unmanageably large [3.5]. The rectangular box shape will not fit into this space unless the whole box is scaled down to impractically small dimensions. The simplest way to achieve a small working distance, typically under 30 mm, is to modify the front entrance portion of the analyser, making sloping upper part that fits under the conical objective pole-piece.

Significant changes to the analyser are also necessary in order to find the design that maximises the analyser's energy resolution on a horizontal detector plane. This was a question not addressed by Khursheed. Khursheed's work was mainly confined to pointing out the possibility of achieving parallel wide-band energy analysis with a multi-excitation plate magnetic box analyser design, but there was no indication whether his particular design was the optimal one. Simulations carried out here, will address the question of how key parameters, such as the entrance angle or number of excitation magnets within the box might be changed in order to improve the overall energy resolution at the detection plane. All these changes were

only made possible through the application of the DLS method. The DLS method ensured that for each change in the analyser's geometry, optimal magnet excitation strengths were found.

Figure 3.10 shows simulated electron trajectory paths through a modified parallel magnetic box analyser design with a conical shaped upper corner after applying DLS optimisation. The slanting upper entrance portion of the analyser now makes it possible to achieve a working distance of less than 20 mm. The emission energies are 50, 100, 200, 400, 600, 1000, 1500, 2000 and 2500 eV and trajectory paths are traced in both the in-plane (x-y) and out-of-plane (x-z). The in-plane angular spread uniformly ranges between −50 mrad and +50 mrad and the two out-of-plane angles are −30 mrad and +30 mrad. The DLS method was applied to optimise the overall energy resolution on a flat horizontal detector plane.

At first, only seven pairs of magnet were tried, but much greater control of the output focal plane shape was obtained after increasing it to nine pairs. These extra pairs of magnets were found to improve the effectiveness of DLS optimisation, providing it a greater degree of freedom in searching for better solutions. Iron pieces were used to connect the magnets to the wall of the box so as to increase the total width of the box (in the z-direction) to about 35 mm to house the detector. The magnetic contours of B_z on the central odd-symmetry plane are also indicated in Figure 3.10 for the optimal solution. Unlike the parallel energy magnetic box spectrometers reported by Khursheed [3.1, 3.6], the optimised parallel magnetic box analyser design (indicated in Figure 3.10) does not have the excitation strengths of the magnets increase in ascending order along the electron trajectory paths. The strength of the second pair of magnets is lower than the strength of the first pair of magnets. This solution was automatically found by the DLS method, and most likely comes from mitigating the effect of fringe field effects at the entrance slit. In this case, the lower energy electrons do not experience any upward

deflection (like that shown in Figure 3.6a). Since the trajectory paths of the higher energy electrons are not greatly affected by the low strength deflection fields at the front part of the analyser, the optimal strengths of the subsequent magnets are of ascending order. Instead of using a 45º entrance angle (relative to the x-axis), as in the original design, the entrance angle was allowed to vary as a free parameter. The optimised entrance angle was found to be 44.86º.

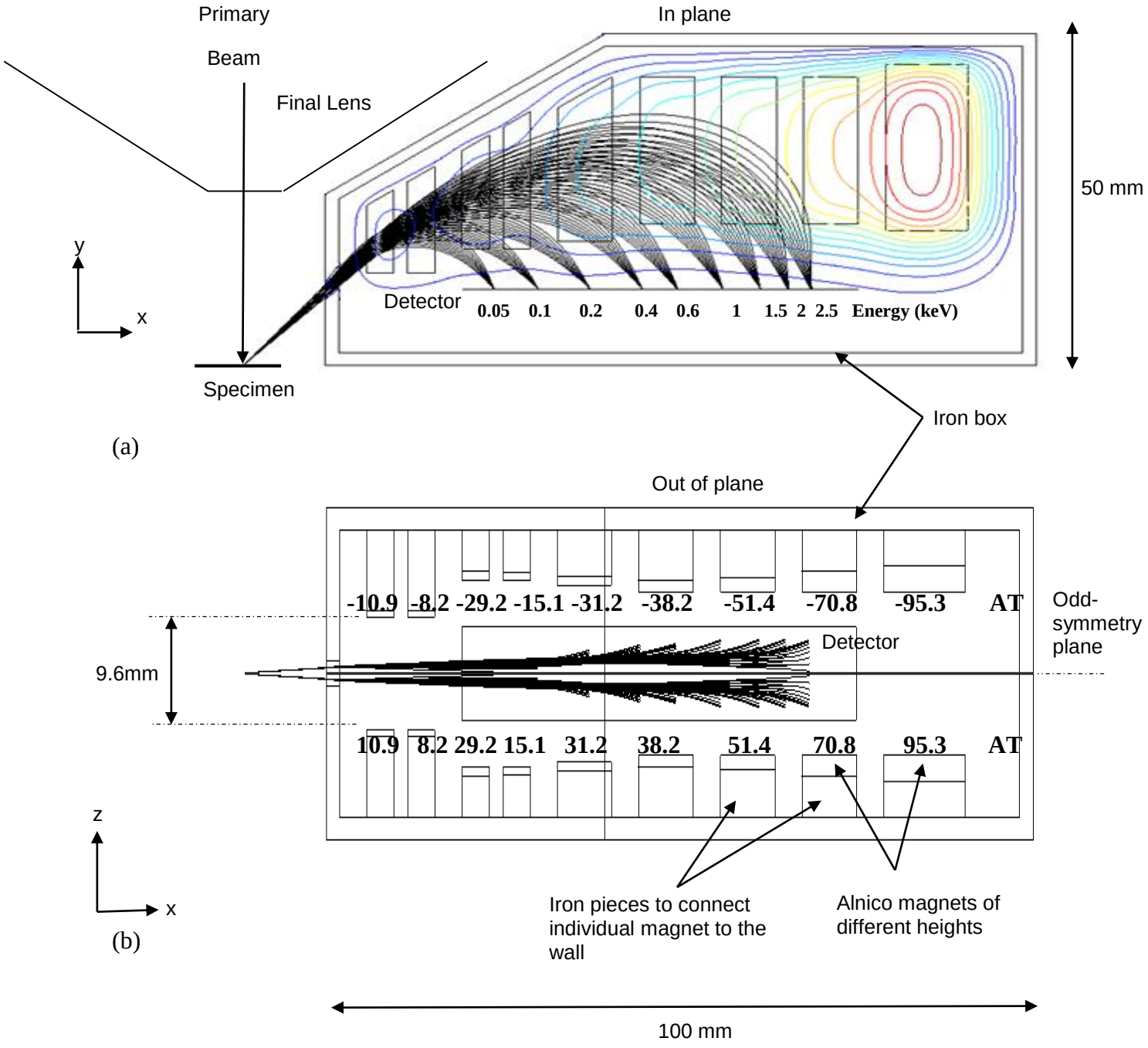

Figure 3.10: Simulated electron trajectory paths through the modified parallel magnetic box analyser design on a horizontal detector plane, trajectories are plot for emission energies of 0.05, 0.1, 0.2, 0.4, 0.6, 1, 1.5, 2 and 2.5 keV.(a) In-plane polar angular spread uniformly ranges between −50 mrad and +50 mrad. B_z contours on the central odd-symmetry plane are plot between 1 and 14 mT in steps of 1 mT (b) For −30 mrad and +30 mrad angular spread in the out-of-plane.

Figure 3.11 shows the simulated relative energy resolution on a horizontal detector plane as a function of energy for the modified parallel energy magnetic box analyser design at a polar angular spread of ±50 mrad and an out-of-plane angle of 30 mrad. Since the relative energy resolution does not degrade significantly (except at extreme energies below 250 eV and above 2250 eV), these simulation results indicate that an acceptable out-of-plane angular range for the analyser typically lies between −30 mrad and +30 mrad.

Another important aspect of the simulation results depicted in Figure 3.11 is that they predict a significant improvement in the overall energy resolution of the modified analyser design (9 pairs of magnets, inclusion of fringe fields, slanting upper entrance and entrance angle of 44.86º) optimised through the DLS technique than for the design shown in Figure 3.8a (not optimised by DLS), this can be seen by comparing their respective energy resolutions shown in Figure 3.11 and Figure 3.9. The average in-plane relative energy resolution for the new modified analyser design optimised through DLS is about 0.32%, which represents an improvement of over 1.5 times of the unoptimised design *(*shown in Figure 3.9). These results illustrate the critical role played by the DLS method in finding an improved analyser design.

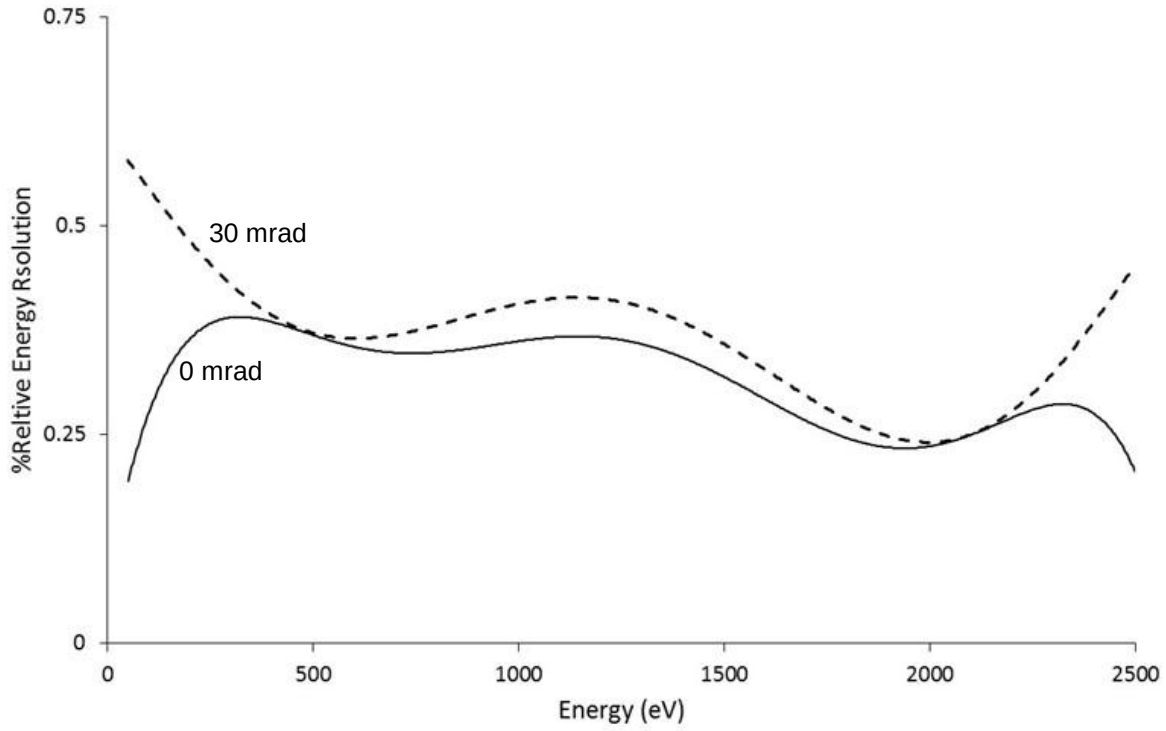

Figure 3.11: Predicted relative energy resolution as a function of energy on a horizontal detector plane for the modified parallel energy magnetic box analyser at a polar angular spread of ± 50 mrad. The simulated energy resolution for an out-of-plane angle of 30 mrad is also shown.

The DLS method has so far, been used to optimise the energy resolution on a flat horizontal detector, and this naturally brings up the question, of how much better the energy resolution would be if the focal plane is not constrained to be horizontal. What shape would the focal plane need to take in order to minimise the overall energy resolution? The following set of simulations set out to answer these questions by allowing the height of focal points to vary as a free parameters. Their DLS optimised focal point positions will be referred to here as intrinsic focal points, and lines connecting these points together across the energy range will be referred to as the intrinsic output focal plane.

Figure 3.12 shows simulated electron trajectory paths through the modified parallel magnetic box analyser design after applying DLS optimisation to the intrinsic output focal plane across the entire energy range. The emission energies are 50, 100, 200, 400, 600, 1000, 1500, 2000 and 2500 eV with the entry polar angle at 44.86º with respect to x-axis. The in-plane angular spread uniformly ranges between −50 mrad and +50 mrad and the two out-of-plane angles are −30 mrad and +30 mrad. The magnetic contours of B_z for the optimized field solution on the central odd-symmetry plane are also indicated in Figure 3.12.

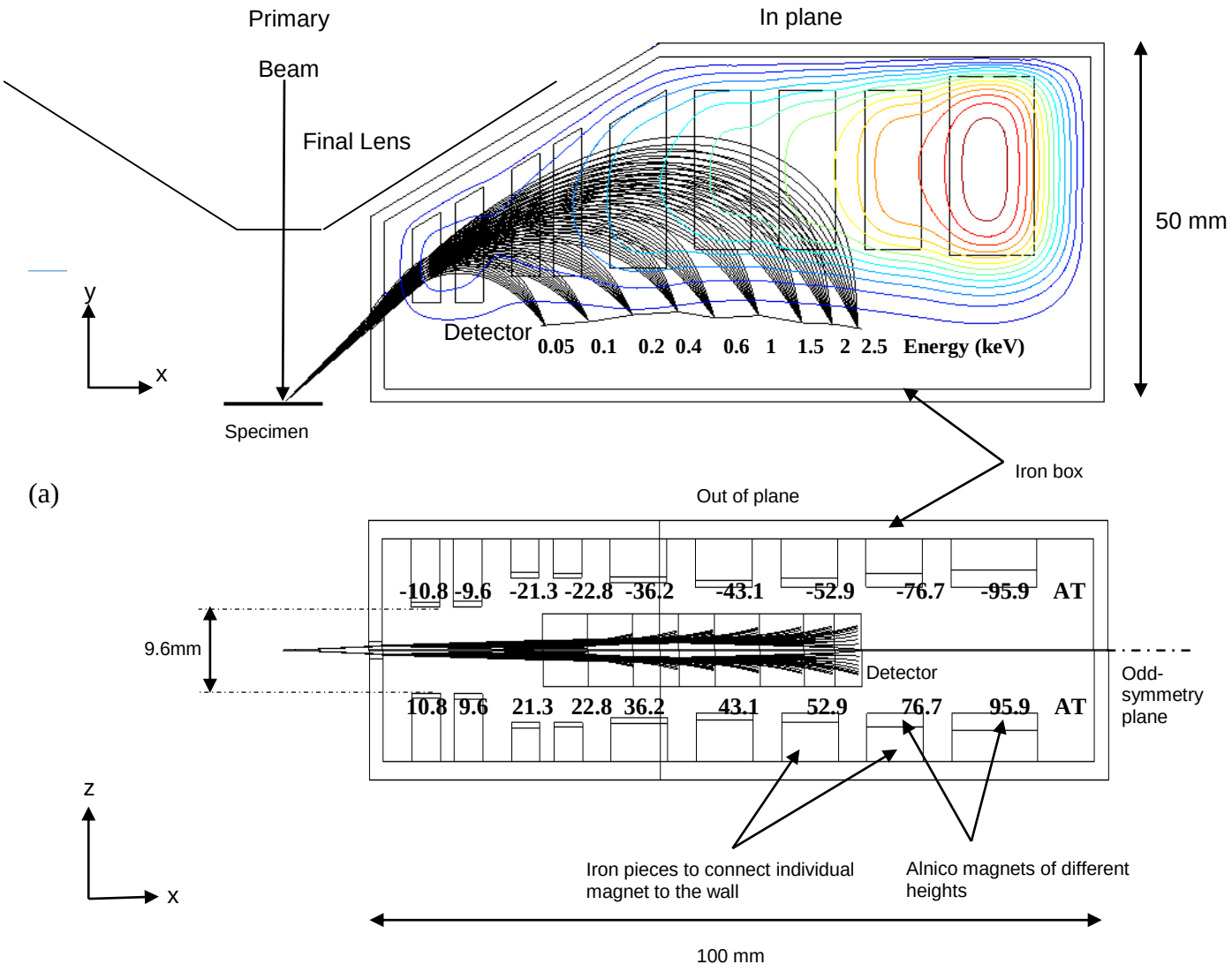

(b)

Figure 3.12: Simulated electron trajectory paths through the modified parallel magnetic box analyser design on its output focal plane (best intrinsic performance), trajectories are plot for emission energies of 0.05, 0.1, 0.2, 0.4, 0.6, 1, 1.5, 2 and 2.5 keV. (a) In-plane, where the polar angular spread uniformly ranges between −50 mrad and +50 mrad. B_z contours on the central odd-symmetry plane are plot between 1 and 14 mT in steps of 1 mT (b) Out-of-plane, for the azimuthal angles of −30 mrad and +30 mrad.

Figure 3.13 shows the magnified view of the simulated ray paths focusing on to the intrinsic output focal plane, indicating that points of sharper focus can be obtained by allowing for focal point height variations for each energy. Confirmation of this is given in Figure 3.14, which plots the simulated relative energy resolution on the intrinsic focal plane across the entire electron energy range. The average in-plane relative energy resolution is now 0.11%, a factor of around 2.5 smaller than its corresponding value on the horizontal detector plane. The simulated energy resolution for the out-of-plane angle of 30 mrad is also shown in Figure 3.14, reduced approximately by the same the same factor.

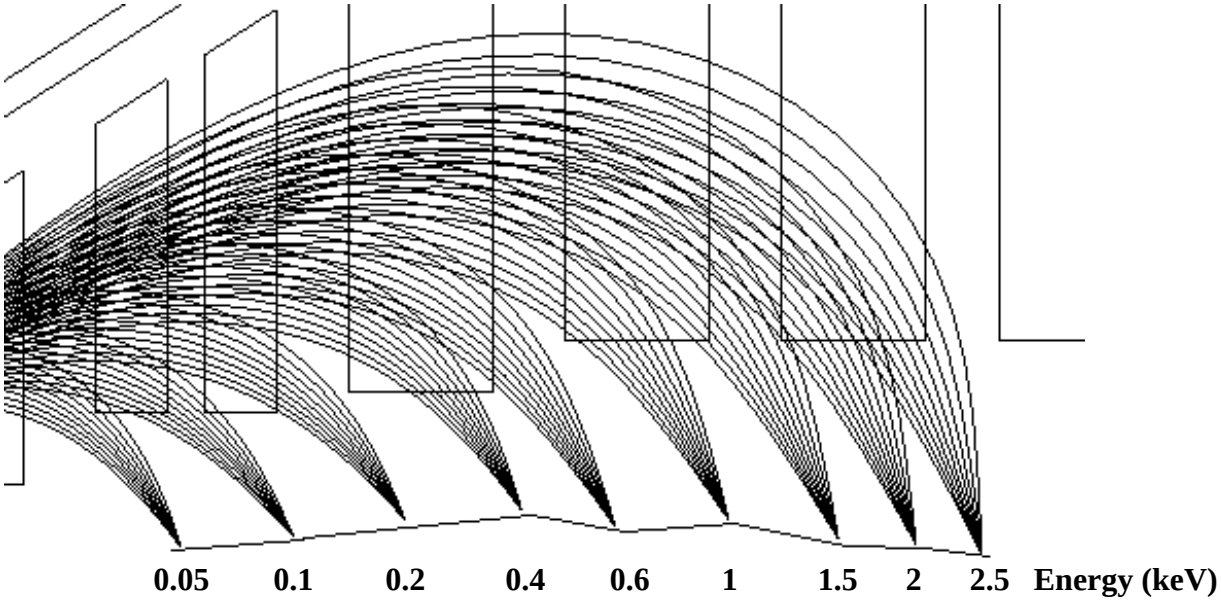

Figure 3.13: Magnified view of trajectory paths on its output focal plane for the parallel magnetic box analyser design.

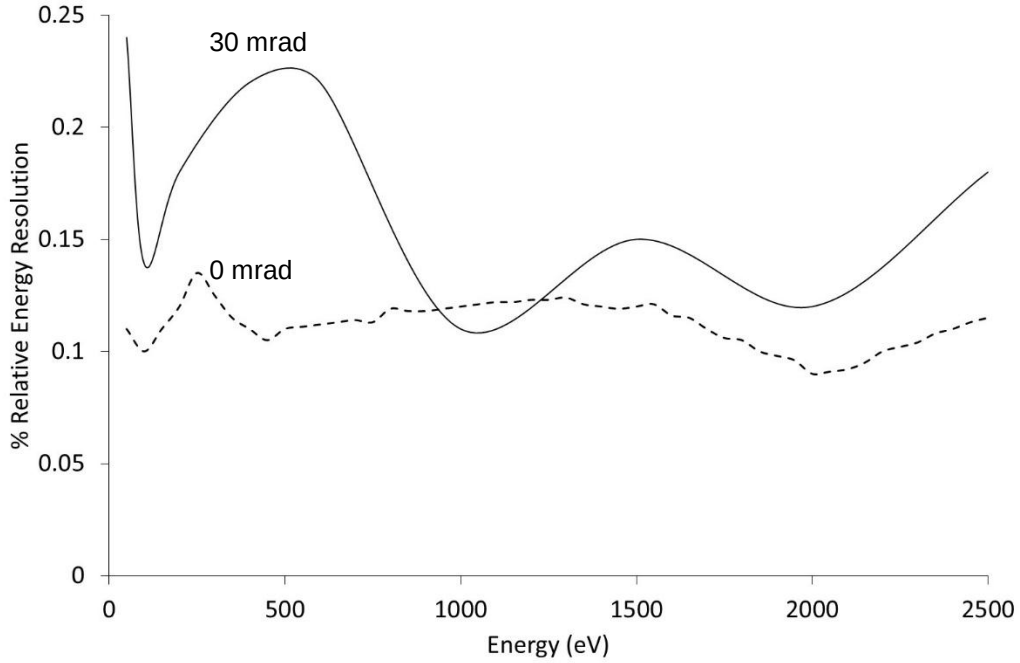

Figure 3.14: Predicted relative energy resolution as a function of energy on its output focal plane for the modified parallel energy magnetic box analyser at a polar angular spread of ± 50 mrad. The simulated energy resolution for an out-of-plane angle of 30 mrad is also shown.

Figure 3.15 shows the simulated trace-width as a function of polar angular spread on the Gaussian focal plane for selected energies. It indicates third-order spherical aberration variations (second-order focusing) obtained for the energies of 50 eV and 2500 eV. The existence of a fourth-order spherical aberration variation (third-order focusing) point is observed at the energies of 200 and 1000 eV, characterized by two local minima in its trace-width distribution. The corresponding dispersion is 150.42 μm at 50 eV, 40.28 μm at 200 eV, 12.56 μm at 1000 eV and 8.04 μm at 2500 eV.

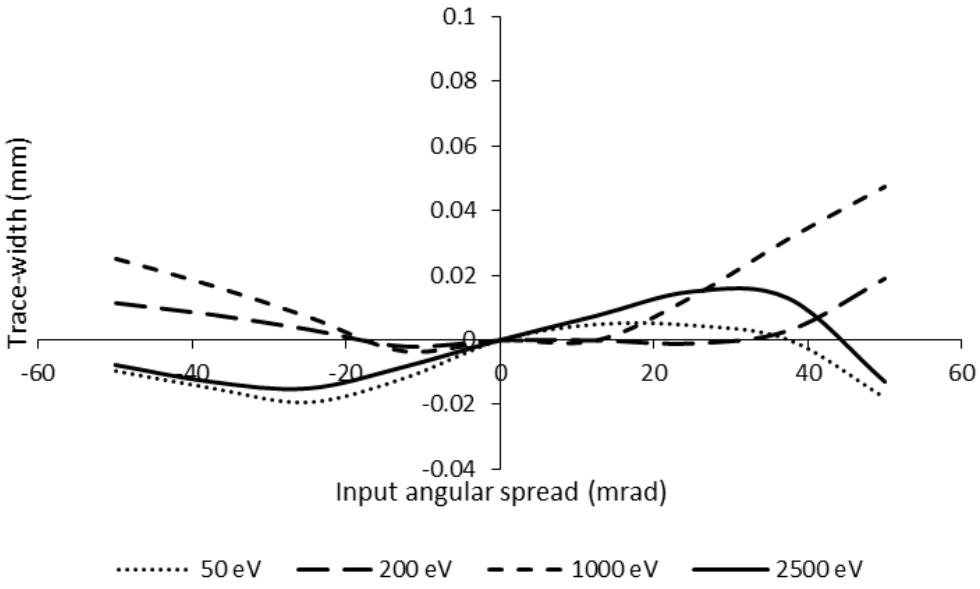

Figure 3.15: Simulated trace-width distributions of the optimised magnetic box analyser design for selected energies.

Figure 3.16 compares the predicted relative energy resolution at a polar angular spread of ±50 mrad for the improved magnetic box analyser design on the horizontal detector plane/intrinsic focal plane together with the HFA, the wide-band parallel energy analyser that had previously been proposed for Auger Electron Spectroscopy (see chapter 1, Figure 1.14). The simulated values taken for the HFA were reported by Khursheed et al. [3.2]. The relative energy resolution as a function of energy on its output intrinsic focal plane for the improved parallel magnetic box analyser design is predicted to be better than one order of magnitude of than those simulated for the HFA.

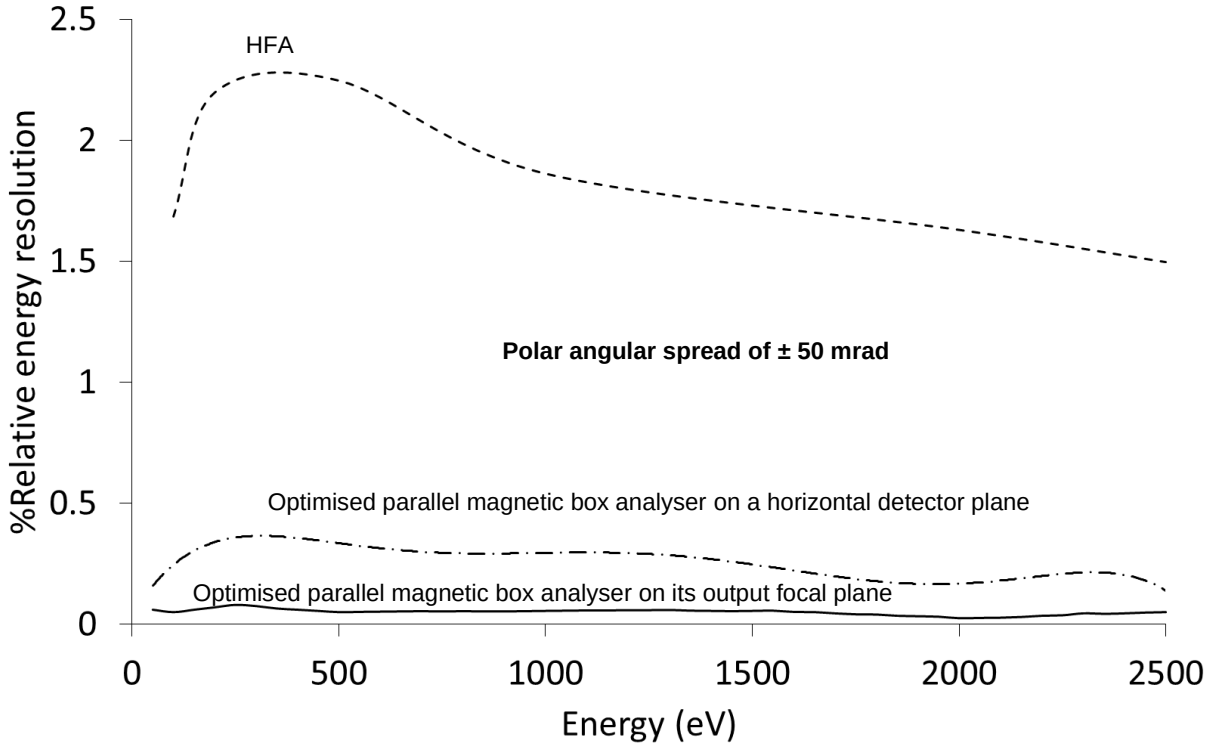

Figure 3.16: Predicted relative energy resolution for the optimised magnetic box analyser design as a function of energy in comparison with the HFA at a polar angular spread of ±50 mrad: (a) horizontal detector plane and (b) output focal plane (best intrinsic).

3.4 Experimental Magnetic field measurements on a prototype

The experimental measurement of the magnetic field distribution within the prototype was carried out through the use of a F. W. Bell Series 9550 Teslameter setup [3.7]. Nine pairs of magnet were fabricated according to the simulation model shown in Figure 3.12. Similar magnets with slightly different thickness (±1, ±3 and ±5%) were also fabricated to help obtain close agreement between experimental and simulated results. The first experiment carried out was the measurement of the magnetic field z-component of each magnet along its height (y-axis) in the xy-plane without the influence of other magnets, as illustrated in Figure 3.17, in which an iron block connects the magnet to the iron wall.

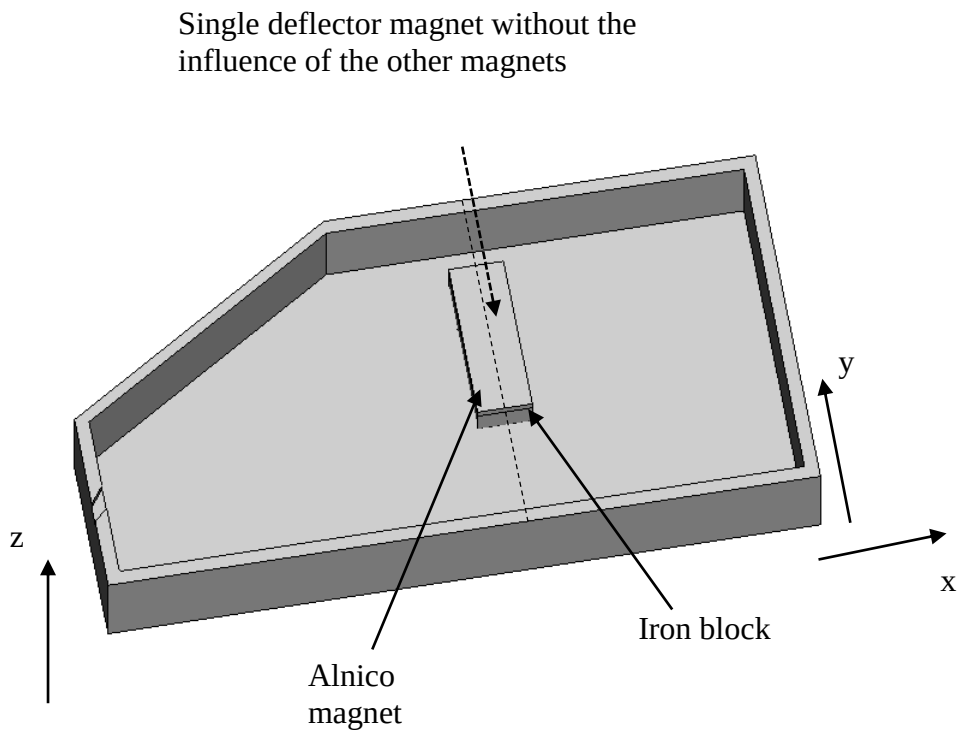

Figure 3.17: Schematic showing the measurement of the magnetic field z-component along the height (y-axis) a magnet in the xy-plane (z = 0) without the influence of other magnets. Only half of the box is shown.

The experimentally measured magnetic field strength was then compared with the simulated magnetic field strength from simulation. The thickness of the magnet which provided the closest agreement to the simulated model was then selected. This was done for each pair of magnetic deflectors, and the results are given in Table 3.1.

	Magnet 1 (nearest to entrance)	**Magnet 2**	**Magnet 3**	**Magnet 4**	**Magnet 5**	**Magnet 6**	**Magnet 7**	**Magnet 8**	**Magnet 9 (furthest from entrance)**
Material of magnet	"Alnico 4/1"	"Alnico 4/1"	"Alnico 4/1"	"Alnico 4/1"	"Alnico 3"	"Alnico 3"	"Alnico 3"	"Alnico 3"	"Alnico 3"
Thickness of magnet (mm)	1.2	1.0	1.6	1.6	2.0	1.9	2.5	3.0	5.0

Table 3.1: Materials and thicknesses of the magnets used in the prototype.

With all the iron blocks and magnets assembled together, the magnetic field strength along the odd symmetry plane boundary (z = 0) was then experimentally measured. Systematic adjustment of the air gap in each magnet pair was achieved by proportionally increasing/decreasing the thickness of the individual iron blocks, so that simulated and experimentally measured magnetic contour plots were as close as possible. The results are shown in Table 3.2.

	Magnet 1 (nearest to entrance)	**Magnet 2**	**Magnet 3**	**Magnet 4**	**Magnet 5**	**Magnet 6**	**Magnet 7**	**Magnet 8**	**Magnet 9 (furthest from entrance)**
Material of magnet	"Alnico 4/1"	"Alnico 4/1"	"Alnico 4/1"	"Alnico 4/1"	"Alnico 3"	"Alnico 3"	"Alnico 3"	"Alnico 3"	"Alnico 3"
Thickness of magnet (mm)	1.2	1.0	1.6	1.6	2.0	1.9	2.5	3.0	5.0
Thickness of accompanying iron block (mm)	6.00	6.25	3.35	3.35	3.50	4.10	3.50	3.00	1.50

Table 3.2: Magnets and Iron block thicknesses for the best match between simulated and experimentally measured contours of deflector magnetic field along the mid-plane symmetry line.

Figure 3.18 (a) shows a photograph of the finalised prototype spectrometer with the nine pairs of alnico magnet and iron pieces in the iron box. Figure 3.18 (b) shows lines of constant magnetic field strength along the odd symmetry plane boundary (z = 0) for both simulated field values and experimentally measured ones. They show good agreement and demonstrate that it is, in principle, feasible to build a compact parallel energy magnetic spectrometer box.

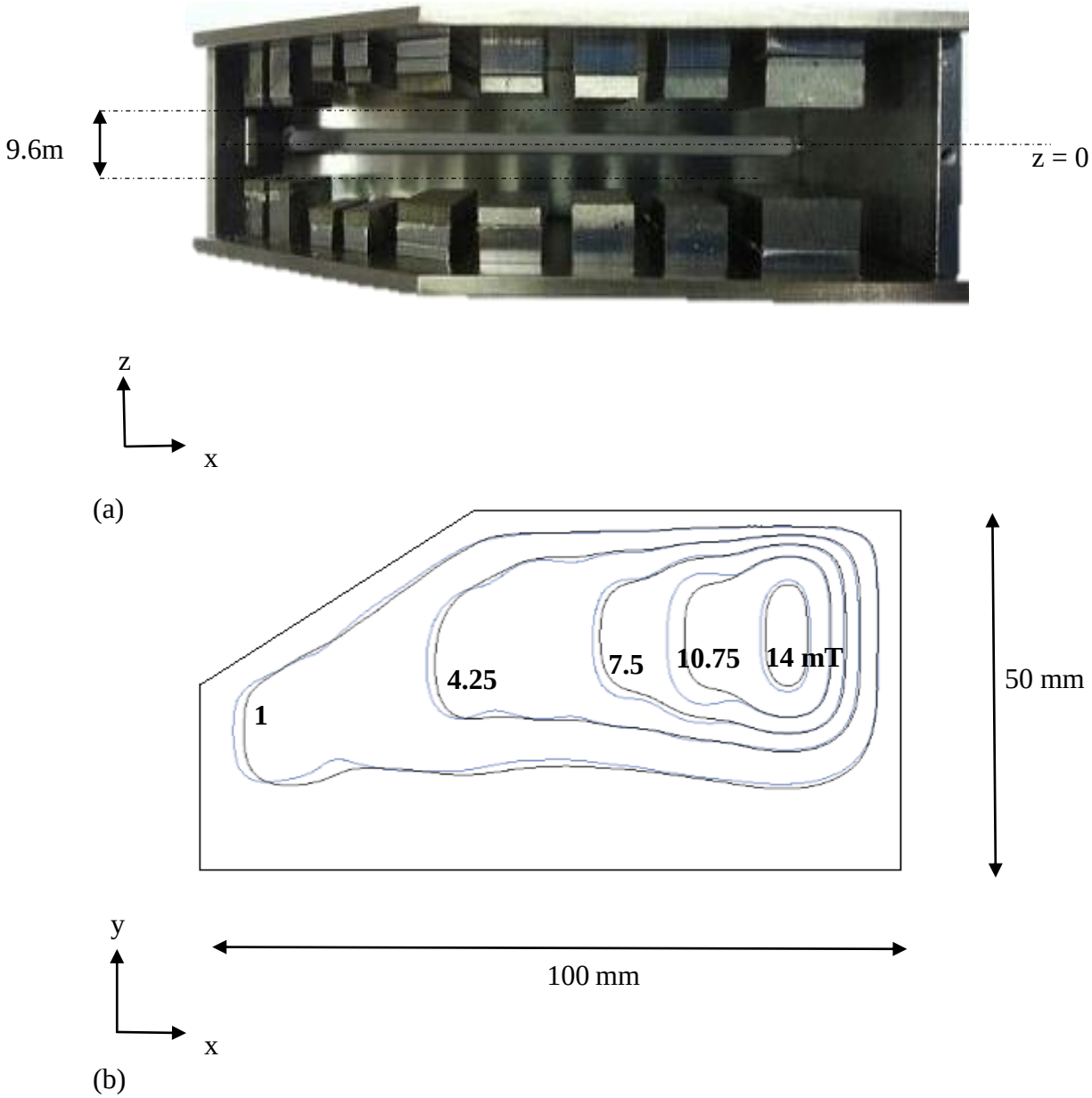

Figure 3.18: Prototype box spectrometer. (a) Plan view photograph (b) Comparison of experimental and simulated contour lines of constant magnetic field strength B_z (x,y) at the mid-odd symmetry plane (z=0). Blue lines are from experiment and black lines are from simulation.

The small adjustments in the prototype analyser required to achieve a good match with the simulated field distribution highlight the need for some means of fine-tuning the excitation strengths electronically. An electromagnet can be constructed around the iron block attached to each alnico magnet (e.g. by winding wire around the iron block and passing current through the wire). In order to achieve proportional ramping of the overall magnetic field that maintains the contours of the field, the ratios of the strengths of the electromagnets to each other must be equal to the ratios of the strengths of the alnico magnets that they are attached to. In this way, in addition to making small adjustments to the magnetic field distribution shape, the whole strength of the magnetic field distribution can also be scaled up and down, which is useful for changing the energy range of detection. In principle, the whole set-up can also be replaced by electromagnets, however, the advantage of an electromagnet/permanent magnet combination is that the electromagnet allows for ease of tuning (i.e. making small changes to the magnetic field to adjust the focusing of the electron beams) whilst the permanent magnet maintains the overall stability of the field.

3.5 A parallel array energy detection system

A flat horizontal position sensitive detector is required for the parallel energy magnetic box analyser design. An array of magnetic box analyser/detectors can be used in the azimuthal direction (around the specimen). Although there are one dimensional rectangular shaped position sensitive detectors for this purpose, they have their limitations. One limitation comes from the fact that the number of pixels in a position sensitive detector needs to be relatively large, so that the energy resolution is not limited by the spacing between pixels. The dispersion created on the detector plane at the minimum energy of 100 eV determines the minimum spacing which pixels need to have in order to avoid degradation of the final energy resolution by the finite number of pixels in the position sensitive detector. Assuming the pixels are spaced uniformly, the number of pixels required is therefore given by dividing the distance between the highest energy (2500 eV) and the lowest energy (100eV) by the pixel spacing, which is, in this case, for around 0.2% relative energy resolution, is 743. A typical position sensitive detector used for this application is the Hamamatsu NMOS linear image sensor S3901/3904 which has 1024 pixels [3.8].

It is impractical from an electronics systems point of view to capture and process such a high number of channels (pixels) in parallel, which is why most position sensitive detectors operate in a time multiplexing mode, where the current in each pixel is sequentially monitored. For this reason, a hybrid method, where an array of individual channeltron detectors and slit apertures can also be considered. After ramping the strength of the entire magnetic field (eg. by electromagnets mentioned earlier), each channeltron then captures a reduced part of the total energy spectrum. This arrangement is partially sequential, partially parallel, and has the advantage of not requiring a horizontal detection plane, avoiding the problems of time-multiplexing and reduced energy resolution. The speed up of data acquisition time with respect

to a single detector is directly proportional to the number of channeltron/slit apertures used. Provision to adjust the height of each slit aperture to the optimum heights shown in Figure 3.19 will be required (indicated by black squares). The optimum heights only vary by a maximum of about 0.5 mm between consecutive focal points, and is therefore something which can easily be achieved in practice.

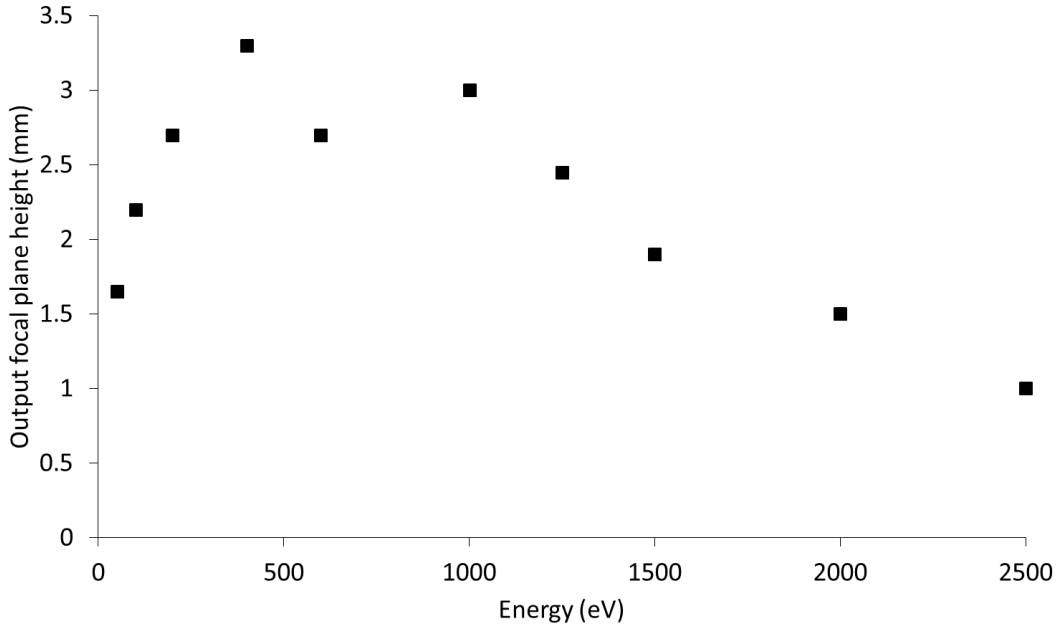

Figure 3.19: Output focal plane height as a function of energy for select energies. The difference in vertical height between each channeltron at select energies is around 0.5mm.

Figure 3.20 shows the simulated average relative energy resolution for corresponding vertical misplacement of each slit-aperture position. The simulation results in Figure 3.20 assumes the worst case scenario in which all slit-apertures are misplaced by up to ± 0.1 mm. The average energy resolution is predicted to lie below 0.16% when all of the slit-apertures are misplaced vertically by ± 0.05 mm. These simulation results indicate that the precision to which each slit-aperture is to be positioned is something that can easily be achieved in practice.

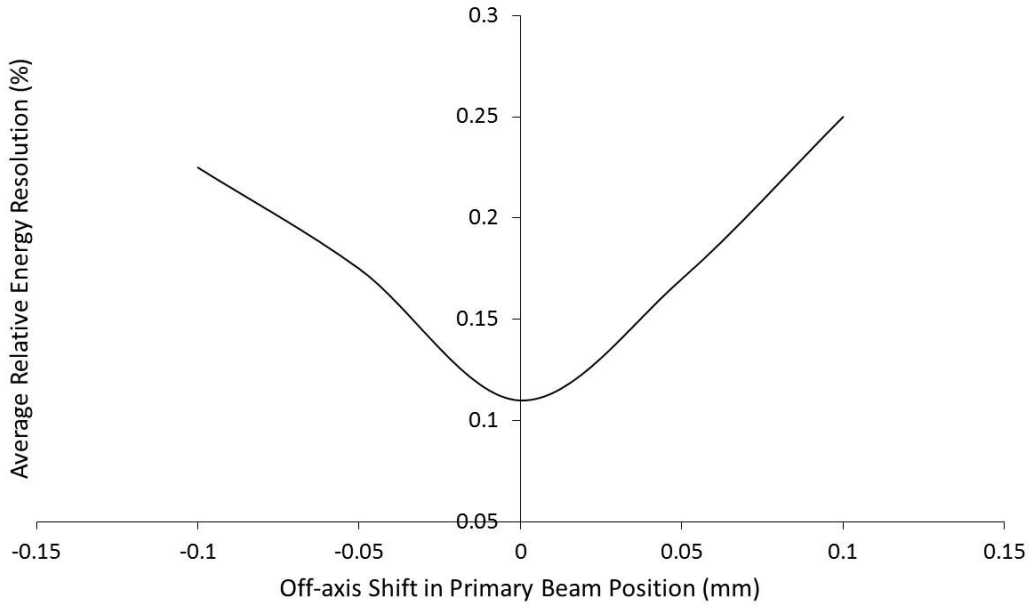

Figure 3.20: Simulated average relative energy resolution for corresponding vertical misplacement of the slit aperture's position.

3.6 Conclusions

In this chapter, the design of the parallel energy magnetic box spectrometer proposed by Khursheed has been revised based upon simulations carried out by the Lorentz 3EM software, which is more realistic and accurate than the original magnetic scalar potential ones. The simulation results predict that the analyser will have a relative energy resolution of below 0.13% for a polar angular spread of ±50 mrad on its output intrinsic focal plane across its entire energy of detection after DLS optimisation. An array of such units can be used in the azimuthal direction, thereby increasing the effective transmittance. A proof-of-concept prototype was constructed based on the design arrived at by simulation. Both simulated field values and experimentally measured ones show good agreement and demonstrate that it is in principle feasible to build a compact parallel energy magnetic spectrometer box of this kind. The optimised parallel magnetic box analyser can potentially be used as an add-on attachment inside the specimen chamber of scanning Auger electron microscopes (SAMs) and SEMs to be operated in combination with a low voltage ion flood beam, where the energy of detection varies from 50 eV to 2500 eV.

References

[3.1] A. Khursheed, Design of a parallel magnetic box energy analyzer attachment for electron microscopes, Journal of Electron Spectroscopy and Related Phenomena, 184 (2011) 57-61.
[3.2] A. Khursheed, H.Q. Hoang, A. Srinivasan, A wide-range Parallel Radial Mirror Analyzer for scanning electron/ion microscopes, Journal of Electron Spectroscopy and Related Phenomena, 184 (2012) 525-532.
[3.3] A. Khursheed, The Finite Element Method in Charged Particle Optics, 1999.
[3.4] Lorentz-3EM, Integrated Engineering Software Inc., Canada, 2011.
[3.5] J. Golstein, D. E. Newbury, D. C. Joy, C. E. Lyman, P. Echlin, E. Lifshin, L. Sawyer, J.R. Michael, Scanning Electron microscopy and x-ray microanalysis, 3rd edition ed., Springer, 2003.
[3.6] A. Khursheed, K. Nelliyan, F. Chao, First-order focusing parallel electron energy magnetic sector analyzer designs, Nuclear Instruments and Methods in Physics Research Section A: Accelerators, Spectrometers, Detectors and Associated Equipment, 645 (2011) 248-252.
[3.7] OECO, Gaussmeter Manuals, Pacific Scientific, in: http://fwbell.com/downloads/manuals/9500-Manual.pdf.

Chapter 4 : A parallel magnetic box mass analyser for FIBs

4.1 Introduction

The possibility of combining Focused Ion Beam (FIB) columns with Secondary Ion Mass Spectrometry (SIMS) techniques has many potential benefits for the nanofabrication of semiconductor devices. The relatively high probe resolution of FIBs (compared to conventional SIMS instruments), if combined with SIMS analysis, will enable it to gather material information on the nano-scale, a useful companion to its milling/deposition capability.

A recent success with techniques that implant the specimen with reactive species such as oxygen and/or cesium or use oxygen flooding is able to increase the FIB-SIMS yield by over two orders of magnitude [4.1]. Coupled by the good focusing properties demonstrated by the parallel energy magnetic box spectrometer design by Khursheed et al. [4.2] for electron energy spectroscopy, the same kind of analyser design is re-developed here for mass spectroscopy applications. The main advantage of magnetic electron energy spectrometers over electrostatic spectrometers is that they avoid the use of high voltages and are able to deflect and focus ions according to their charge-to-mass ratios.

There are several points to consider for a FIB parallel magnetic box mass spectrometer design. Firstly, ions are much heavier than electrons, hence a mass analyser will require larger deflection field strengths than an energy analyser in order to maintain the same turning radius. In order for H^- ions of 2,000 eV to have the same turning radius in a magnetic sector as electrons of 100 eV, the magnetic field in the former case needs to be scaled up by a factor of around 1823. Since the parallel magnetic box energy analyser is able to accept a wide energy range (maximum energy/minimum energy), the mass analyser will similarly be able to accept a wide range of mass defined by the same ratio after the magnetic field has been scaled up. Secondly,

in order to reduce magnetic saturation limitations, keeping the maximum deflection field strength to say around 1 Tesla, the analyser dimensions may need to be scaled up. Thirdly, both energy and angular dispersion on the secondary ions leaving the specimen will need to be suppressed, so that landing positions on the detector are primarily determined by a secondary ion's charge-to-mass ratio. All these design considerations point towards the use of the double-focusing electric sector/magnetic box analyser concept which has been discussed in chapter 1.

The simulated results presented in this chapter predict that it is possible to develop feasible FIB parallel mass spectrometer designs based upon Khursheed et al.'s magnetic box energy analyser designs, and therefore perform SIMS analysis on the nano-scale range. A model based upon the magnetic scalar potential model was first used by numerical field distribution software and ray tracing integration routines written by Khursheed [4.3]. The finite-element method was used to solve for linear magnetic field distributions and 4^{th}-order Runge-Kutta techniques were used to plot trajectory paths of charged particles through all field distributions. Simulation parameters such as the size of a numerical mesh or trajectory step were systematically adjusted in order to minimize the influence of numerical errors on important optical parameters, such as spectrometer energy dispersion, trace-width and mass resolution. The simulation was later improved by using Lorentz-3EM [4.4], which uses the magnetic vector potential in three-dimensions and is capable of taking into account non-linear effects of material properties and magnetic saturation. Details of Lorentz-3EM have been given in chapter 2.

4.2 An analytically generated deflection field distribution

The magnetic deflection field strength inside magnetic sector spectrometers is usually kept constant. By allowing the deflection field strength to increase in the path of incoming electrons/ions, Khursheed et al. demonstrated through simulation [4.5], that charged particles

having a wide range of different energies/masses can be deflected and focused simultaneously. Figure 4.1 shows such simulated trajectory ray paths for selected ions leaving a source located 1cm from the left-hand edge of the deflection field distribution with an energy of 2 keV, and having an angular spread of ±25 mrad, through an asymmetric Gaussian deflection field distribution, $B_{z0}(x,y)$, given by

$$B_{z0}(x,y) = B_0 \exp\left[-\left(\frac{x - x_0}{\sigma_x(x)} \right)^2 - \left(\frac{y - y_0}{\sigma_y(y)} \right)^2 \right], \qquad (4.1)$$

where x_0 and y_0 are the x and y coordinates that define the position of maximum field strength, B_0, and $\sigma_x(x)$ and $\sigma_y(y)$ are standard deviations that describe how the function falls on either side of it in the x and y directions respectively. Ions are deflected in the x-y plane, and the magnetic deflection field is applied in the z- direction. Dotted lines in Figure 4.1 represent contour lines of constant magnetic field strength, essentially oval in shape.

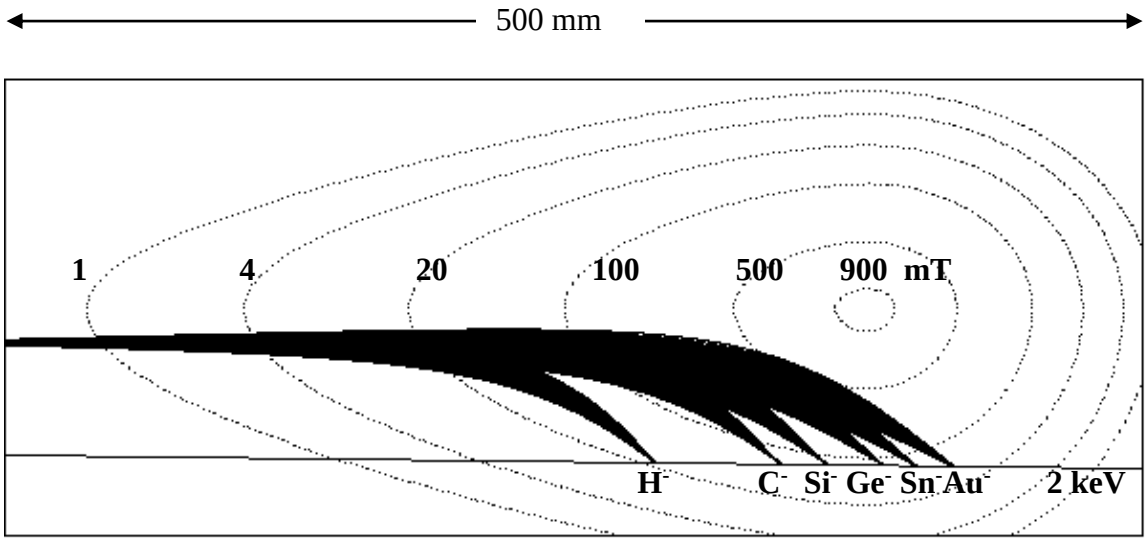

Figure 4.1: Simulated ion trajectories through an analytical asymmetric Gaussian magnetic field distribution. The source is located 5 cm from the left hand edge of the diagram, ions have an energy of 2 keV, and an angular spread of ± 25 mrad. The dotted lines indicate contours of equal magnetic field strength (pointing normal to the page). The entry height of 95 mm.

Table 4.1 gives the field parameters required to generate the magnetic field distribution shown in Figure 4.1, where the outer boundaries of the analyser field distribution are defined by $x_1 < x < x_2$ and $y_1 < y < y_2$ in the x-y plane, which in this case, extends from 0 to 500 mm in the x-direction and 0 to 200 mm in the y-direction.

B_0 = 0.95 T, x_0 = 380 mm, y_0 = 100 mm
σ_x (x) = 47.5 mm for $x_0 < x < x_2$,
σ_x (x) = σ_{x0} [4.1+ 0.195 ($x_0 - x$)/ σ_{x0}] for $x_1 < x < x_0$, where σ_{x0} = 62.5 mm,
σ_y (y) = 36.25 mm for $y_1 < y < y_2$

Table 4.1: Parameters in Equation (4.1) for analytical field distribution depicted in Figure 4.1.

In Figure 4.2, a magnified view of the simulated trajectory paths around the output focal plane is shown, indicating that it is slightly curved in shape and a straight-line detection plane approximation is also shown.

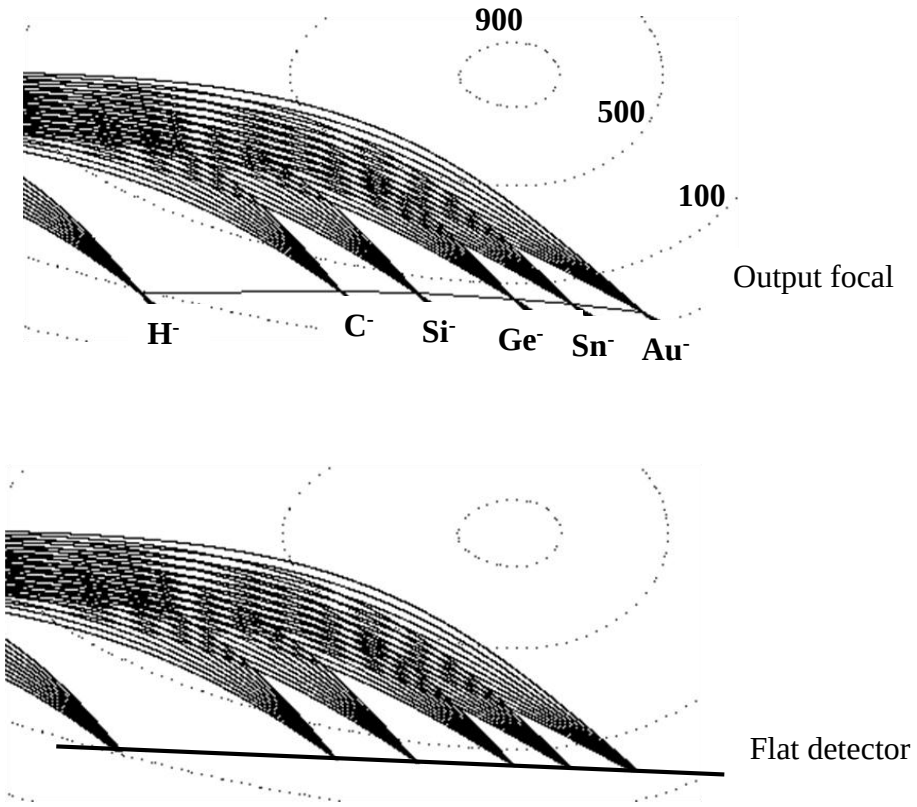

Figure 4.2: Simulated rays paths around detector plane for analytical asymmetric Gaussian deflection field distribution. Ions leave a source located 1 cm from the box entrance with an energy of 2 keV and angular spread of ± 25 mrad.

Figure 4.3 shows the calculated relative mass resolution based upon plotting the kind of ray paths shown in Figures 4.1 and 4.2, for the fixed single energy of 2 keV. In this case, 17 different masses over the range of 1 – 260 amu were used. The mass resolution along the output focal plane is, as expected, higher than the predicted one for the straight-line detection plane. The analyser is predicted to have an average mass resolution limited by spherical aberration of

205 for an input angular spread of ± 25 mrad along its output focal plane, which when projected on to the horizontal detection plane, drops to 100. The curves in Figure 4.3 reach a maximum value between 100 and 130 amu.

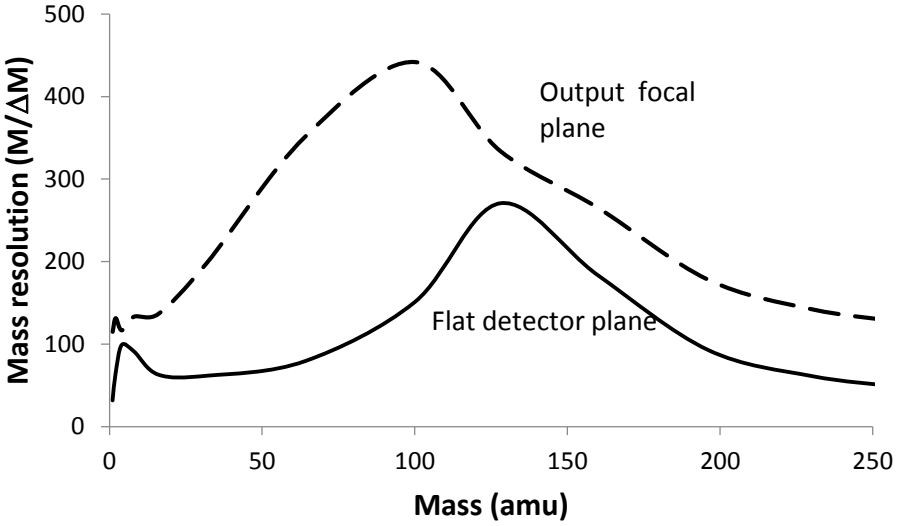

Figure 4.3: Simulated mass resolution for an analytical asymmetric Gaussian deflection field distribution. Ions have an energy of 2 keV and an angular spread of ± 25 mrad.

4.3 A parallel magnetic box mass analyser design

There are many ways to create the required magnetic field distribution for the Gaussian field analyser. One approach is to use permanent magnets placed behind iron plates inside an iron box, as shown in Figure 4.4. The strength of each pair of permanent magnets was progressively increased in the *x*-direction, modelled here in terms of increasing magnetic scalar potential magnitudes.

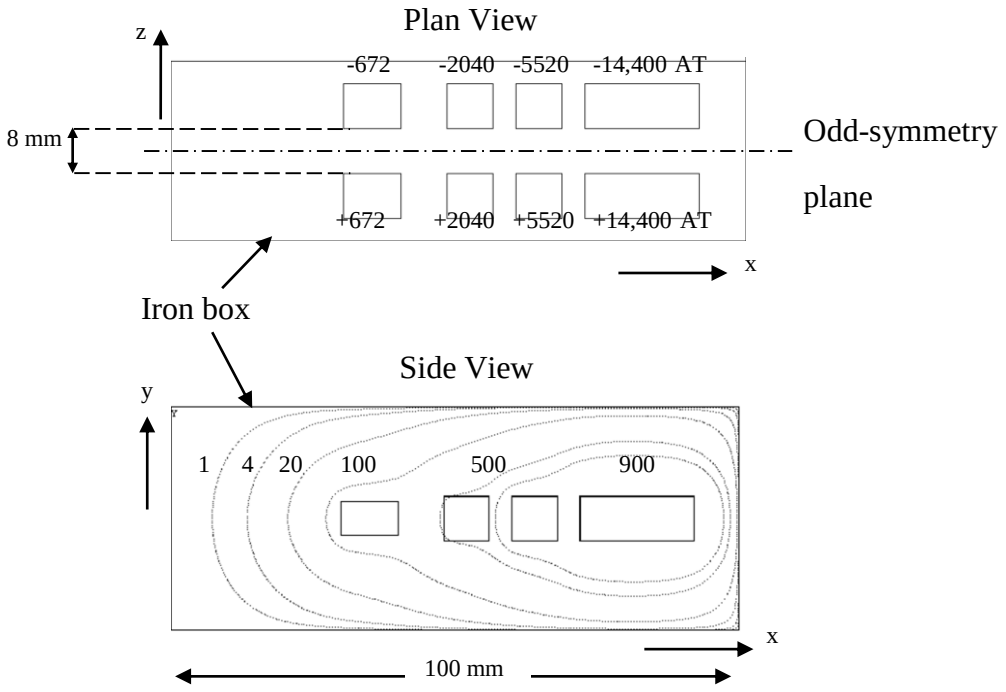

Figure 4.4: Simulated field distribution simulation of the Gaussian field analyser box. Dotted lines indicate contours of equal magnetic field strength along the central odd-symmetry plane.

Figure 4.5 shows simulated 2 keV ion trajectories of positive and negative ions through the Gaussian field analyser box design, predicting that they can be simultaneously focused on to a horizontal detector. The ion source, in this case, is located at the left hand side of the box.

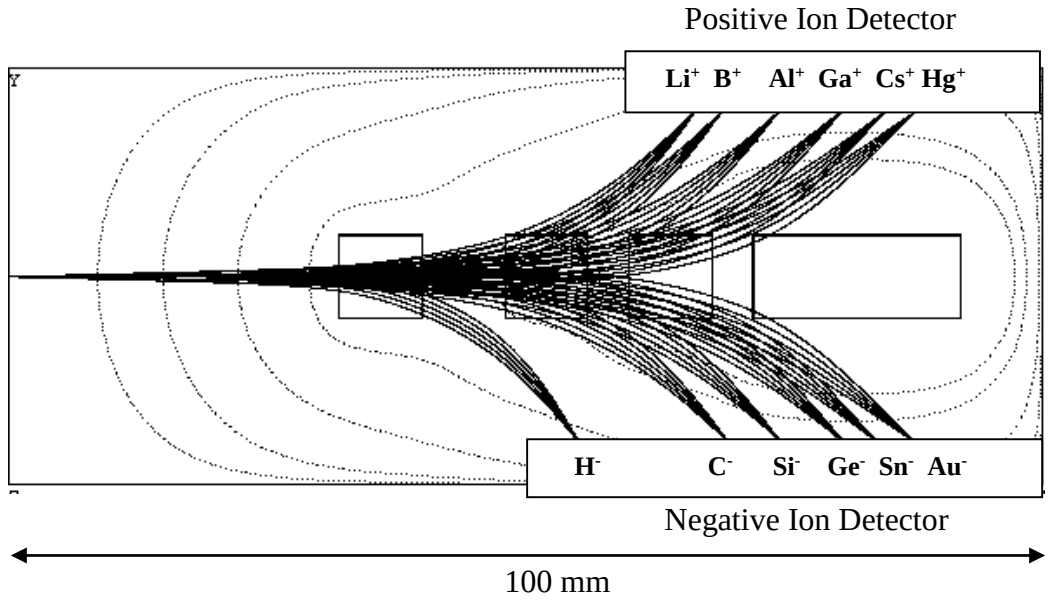

Figure 4.5: Simulated 2 keV ion trajectories through the Gaussian field analyser box design with an input angular spread ranging from -25 to 25 mrad. The ion source (not shown) is located outside the box spectrometer, 1 cm from the left hand side of the outer box.

An indication of how well ions can be focused by the Gaussian field box analyser design is shown in Figure 4.6, which presents an estimate of the relative mass resolution limited by spherical aberration, as a function of relative atomic mass.

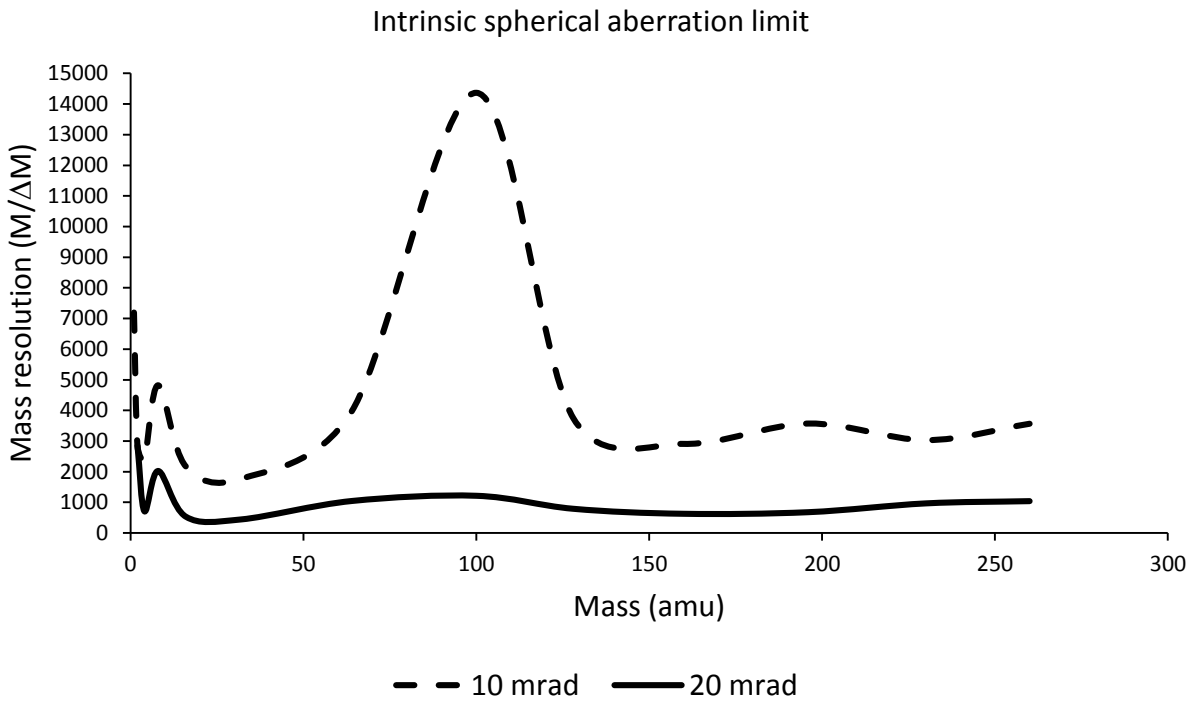

Figure 4.6: Simulated mass resolution limited by intrinsic spherical aberration as a function of relative atomic mass and input angular spread for the Gaussian field box spectrometer design.

This graph in Figure 4.6 was obtained by monitoring the trace-width created by angular dispersion and by comparing it with the change in distance created by mass dispersion and the mass resolution taken to be half the total trace-width. Figure 4.6 displays the intrinsic mass resolution and not the mass resolution projected onto the horizontal detector plane. For the most part, the calculated mass resolution increases by around a factor of 4 as the angular spread changes from ±20 to ±10 mrad, indicating the presence of a second-order spherical aberration (first-order focusing optics); however, at 100 amu, it increases by around a factor of 12, showing that there is at least one point of higher-order focusing predicted.

4.3.1 The electric sector deflector and acceleration transfer lens

Figure 4.7 shows how the Gaussian field analyser box design might be used inside a FIB specimen chamber as a mass spectrometer attachment. Ions are first extracted from the specimen by an accelerating transfer lens, which forms a cross-over point at the entrance of an electric sector deflector.

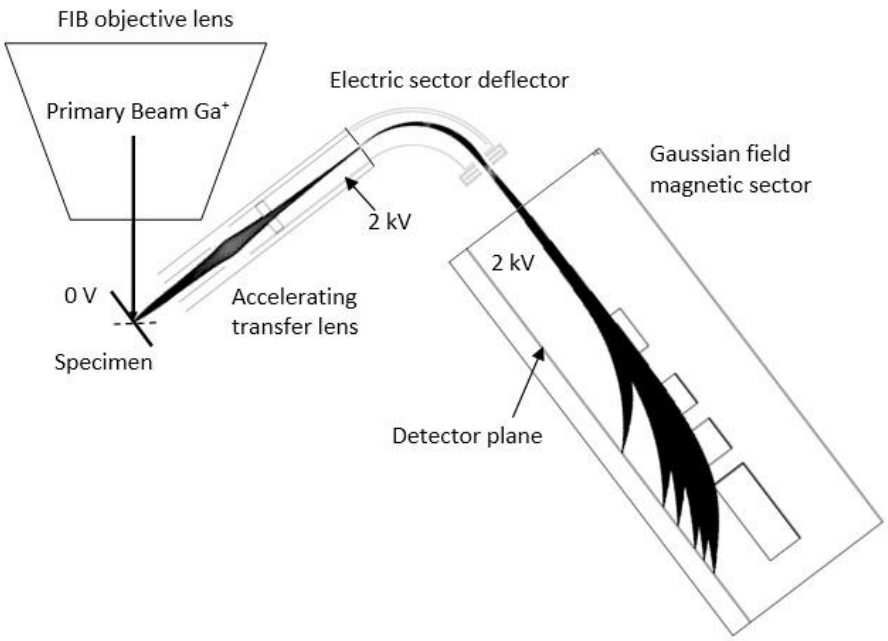

Figure 4.7: A FIB-SIMS mass analyser attachment layout.

It is important to investigate the focusing properties of the present magnetic box analyser design in combination with some form of energy dispersion compensation. The electric sector deflector needs to be designed to compensate for the energy dispersion within the Gaussian field analyser (to the first-order), so that the separation of ions on the detector plane comes primarily from differences in charge-to-mass ratio. The conventional method, of using the energy dispersion of an electric sector to cancel the energy dispersion of a magnetic sector analyser, only usually applies to a relatively small output mass range. In this case, cancellation of energy spread must take place across a wide output mass range, one that vary by three orders

of magnitude. Ideal energy spread compensation characteristics for the magnetic box analyser design can be found by plotting rays having different energies at different input heights, and noting their subsequent positions on the detector plane. A ray entering the box slightly higher than the central ray, will tend to focus a little distance before it on the detection plane, whereas a ray entering the box a little lower than the central ray, will tend to focus a little distance beyond it on the detection plane. Therefore, if there is an energy spread on the incoming ions into the box, they can be made to focus on to the same point on the detection plane (to a first-order approximation) if higher energy electrons enter the analyser above the central ray, and lower energy electrons enter it below the central ray. The required dispersion in the entrance height, Δy is a function of input energy, ΔE, and by tracing rays at different heights and energies, ideal energy dispersion cancellation characteristics can be found for the magnetic box analyser design.

Simulation results show that a 1% variation in energy should be compensated by a corresponding 0.171 mm change in height, and that the change in height should vary approximately linearly with energy spread. Having established this, a suitable electric sector deflector was designed to provide precisely this predicted energy dispersion on its output focal plane. Figure 4.8 shows direct ray tracing of ions for such an electric sector together with the magnetic box analyser design. On its output focal plane, the dispersion of the electric sector can be represented by the following energy and angular dispersion terms,

$$\Delta y = \frac{\Delta E}{E} C_c - C_s \alpha^2 \tag{4.2}$$

where C_c is a chromatic aberration term, and C_s is a second-order spherical aberration term.

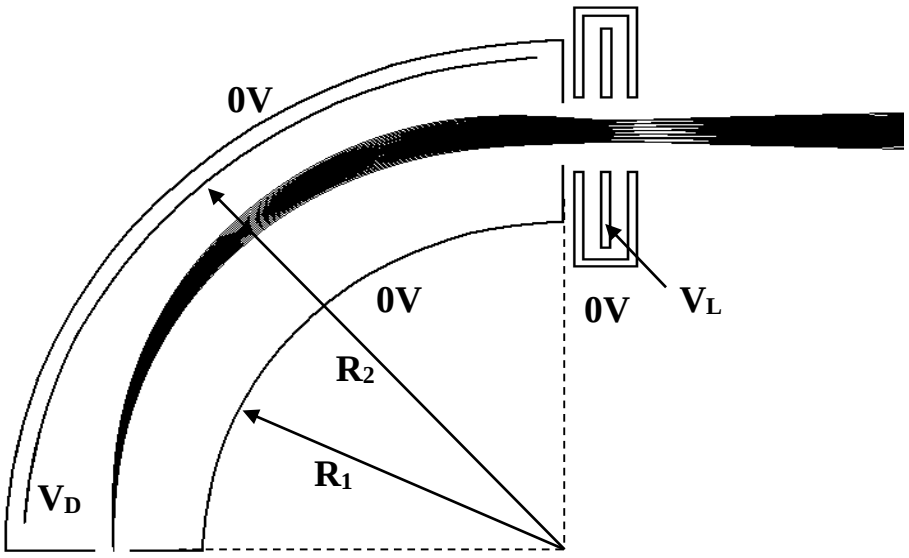

Figure 4.8: Simulated ion trajectories through the electric sector designed to compensate for energy dispersion. Nine trajectories are plot in uniform steps in the angular spread range of -25 to 25 mrad, at the energies of 1940, 2000 and 2060 eV (± 3% spread around the pass energy).

For the electric sector shown in Figure 4.8, C_C = 17.1 mm and C_S = 24.51 mm. The dimensions of the electric sector are R_1 = 6.8 cm and R_2 = 10.25 cm in order to provide the required energy dispersion. The source was placed close to the electric sector entrance in order to have near vertical focal plane at its exit. In addition a lens element was placed at the electric sector exit, in order to control the position of the focal plane in the horizontal direction, providing greater flexibility in creating the required dispersion condition. The internal deflector plate, V_D, was set to be 0.597 times the pass voltage (2 kV), and the middle electrode on the lens, V_L, was set to be 1.2 times the pass voltage.

Figure 4.9 depicts simulated ray paths around the detector plane for a monochromatic input beam, and a beam having a ± 3% energy spread, with and without energy spread compensation. The mass range was restricted to be between 5 to 50 amu for reasons of clarity, similar results

are obtained for masses between 50 to 260 amu. These simulation results indicate that significant energy spread compensation is predicted for the magnetic box analyser design.

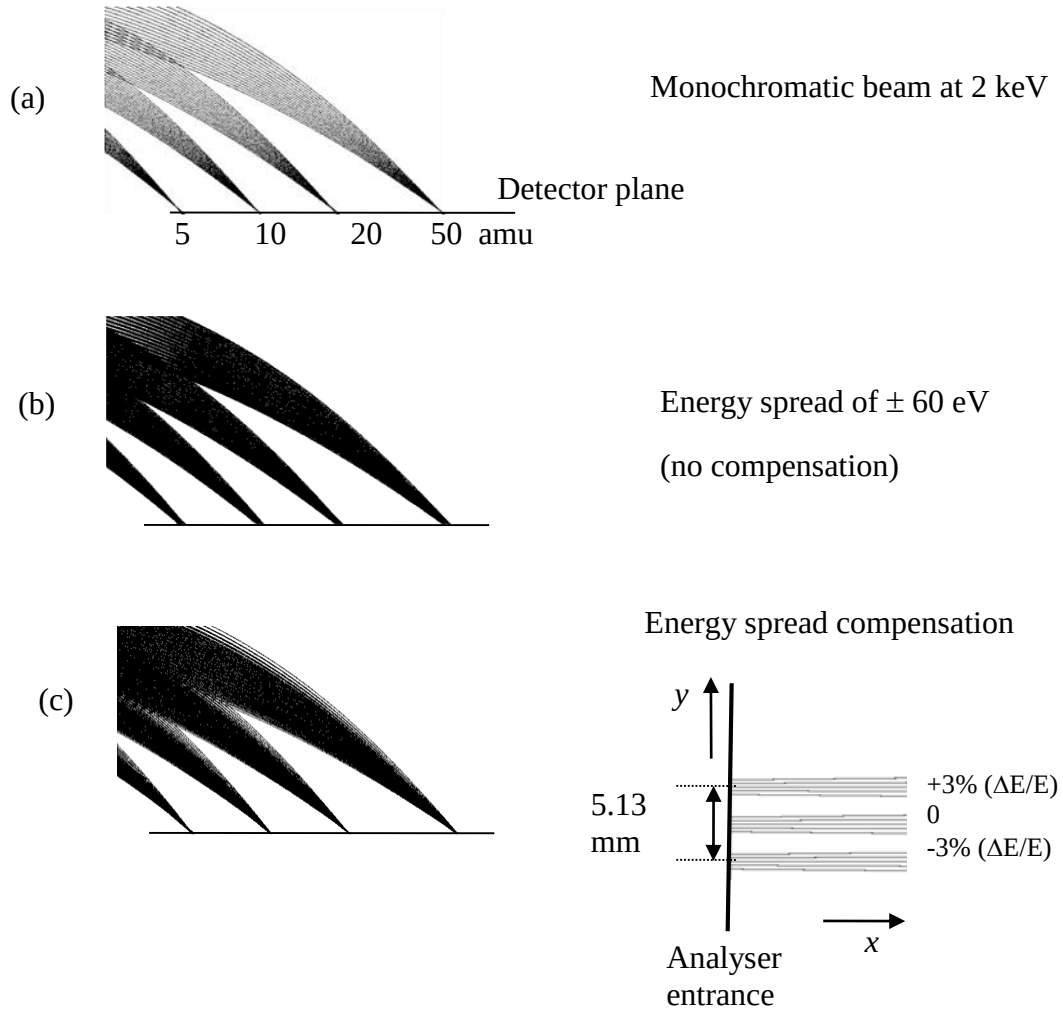

Figure 4.9: Simulated ray paths around the detector plane for the magnetic box scalar potential design for an input angular spread of ± 25 mrad. (a) For a 2 keV monochromatic beam (b) 120 eV (± 60 eV) energy spread with no compensation (c) 120 eV (± 60 eV) electric sector energy spread compensation at analyser entrance.

The simulated trace-width as a function of input angular spread for selected masses is shown in Figure 4.10. The trace-widths corresponding to peaks in the angular spread curve in Figure 4.10, at masses 8, 100 and 230 amu, indicate the presence of second-order focusing (third-order

spherical aberration variations), while at a mass close to its minimum value, say at 32 amu, there is first-order focusing (second-order spherical aberration variations).

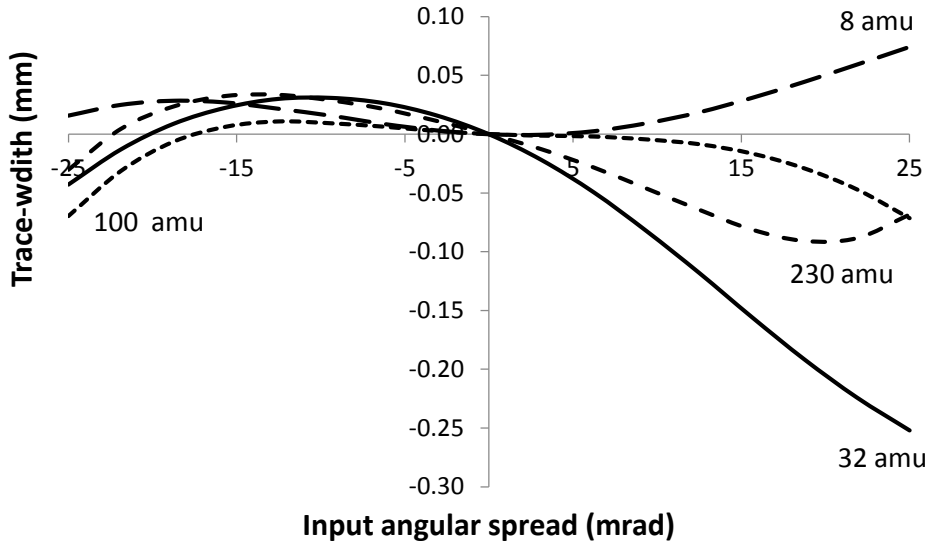

Figure 4.10: Simulated trace-width distribution in the magnetic box scalar potential design for selected ions.

Figure 4.11 demonstrates the use of an acceleration transfer lens to extract ions from the specimen. The simulated electric potential distribution and trajectory ray paths for the accelerating transfer lens are also shown in Figure 4.11. A 1.2 mm aperture was used within the lens to filter out wide-angle scattered ions, so that the final exit angles lie within ± 20 mrad of the central ray. This naturally reduces the transmission of scattered ions at higher emission energies. Table 4.2 presents simulation predictions of how the transmission falls with emission energy. The transmission estimate is based upon assuming that there is a cosine polar angular distribution, and comparing the number of secondary ions reaching the detector to those emitted over a small hemispherical region above the specimen. The results in Table 4.2 indicate how the aperture within the accelerating transfer lens can be used to change the energy and angular spread of the ions that reach the detector, effectively controlling the spectrometer's mass resolution.

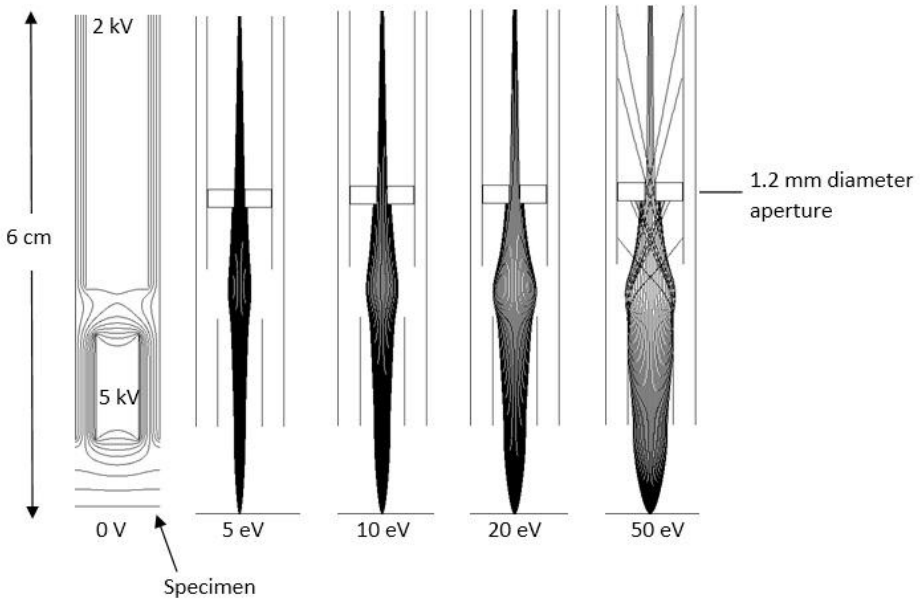

Figure 4.11: Simulation of the accelerating transfer lens with a 1.2 mm diameter aperture.

Emission energy (eV)	Emission cut-off angle (rad)	Estimated transmission (%)	Maximum exit angle (mrad)
5	0.59	30.8	20.0
10	0.4	15.1	18.9
20	0.26	6.6	16.9
50	0.13	1.7	11.2

Table 4.2: Transmission characteristics of accelerating transfer lens for a 1.2 mm diameter aperture.

4.3.2 Extraction field effect on the FIB primary beam optics

The extraction electric field created by the accelerating transfer lens will naturally affect the FIB primary beam optics. To assess how significant an effect this is expected to be, direct ray tracing of a 20 keV Gallium ion beam travelling through the accelerating lens fringe field was

carried out for different incident angles/angular spreads. Simulated equipotentials of the accelerating transfer lens fringe field distribution are shown in Figure 4.12a. As shown in the diagram, the primary beam travels through a relatively weak part of the fringe field, and therefore the effect on the primary beam is expected to be small. Simulated results based upon direct ray tracing show that the effect of the fringe field is both to displace the primary beam position along the specimen and to slightly focus/defocus it. Single rays with incident angles of 25° to 60° relative to the specimen plane were plotted in order to determine a possible minimum shift at the specimen. The optimum incident angle was found to be 45° in which we observe a minimum shift at the specimen to range from only 0.2 to 0.3 mm (the value depends on the sign of the extraction field). This small shift at the specimen may be easily compensated by deflection plates within the FIB primary beam column. Figure 4.12b shows the simulated aberration width at the specimen as a function of angular spread around an incident angle of 45° with the angular spreads of ± 10 mrad and ± 20 mrad. This was done for the extraction electrode being –5kV and +5 kV (necessary to capture positive and negative secondary ions respectively). A quadratic fit to the trace-width variation for both the extraction electrode being -5 kV and +5 kV was found to be adequate, indicating an increase in aberration width due to the fringe field effect. The angular spread of a FIB beam is usually 1 mrad or less (produced by say a 20 mm focal length objective lens and a 20 μm radius final aperture), which when projected on to the graph shown in Figure 4.12b, translates into an estimated trace-width of around 0.2 nm along the specimen plane. Since the FIB probe resolution usually lies between 5 to 20 nm, these simulated results indicate that the extraction field of the accelerating transfer lens will not significantly degrade the FIB primary beam probe resolution. A conservative estimate places this degrade at a mere 1.6%.

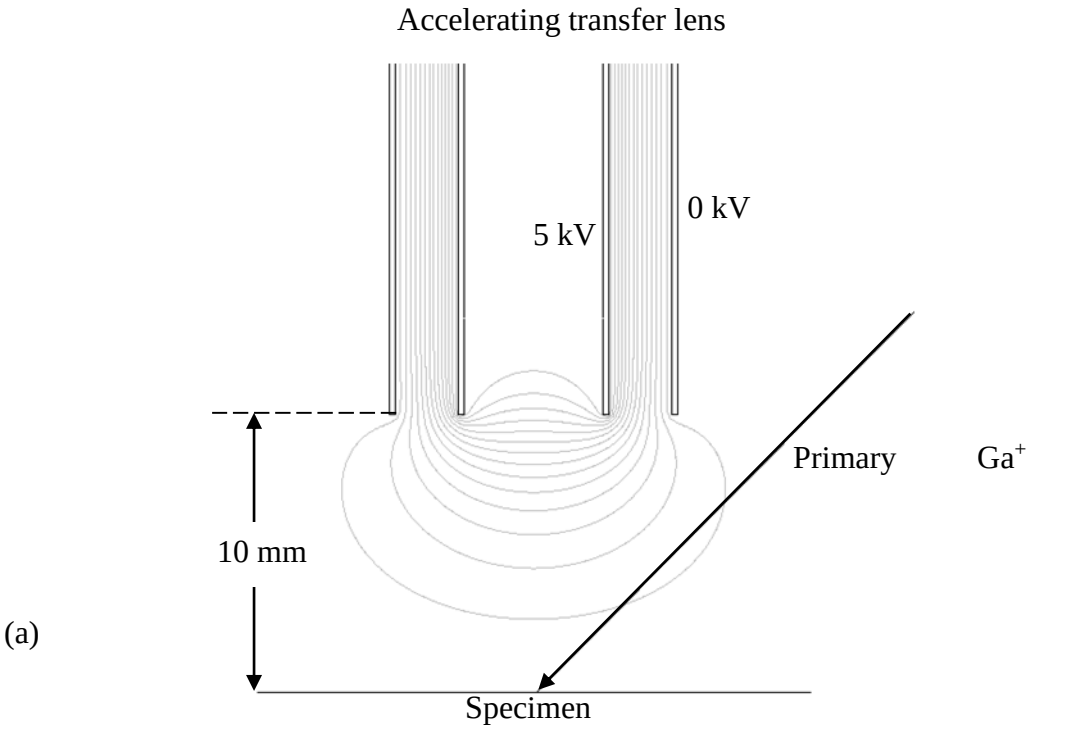

(a)

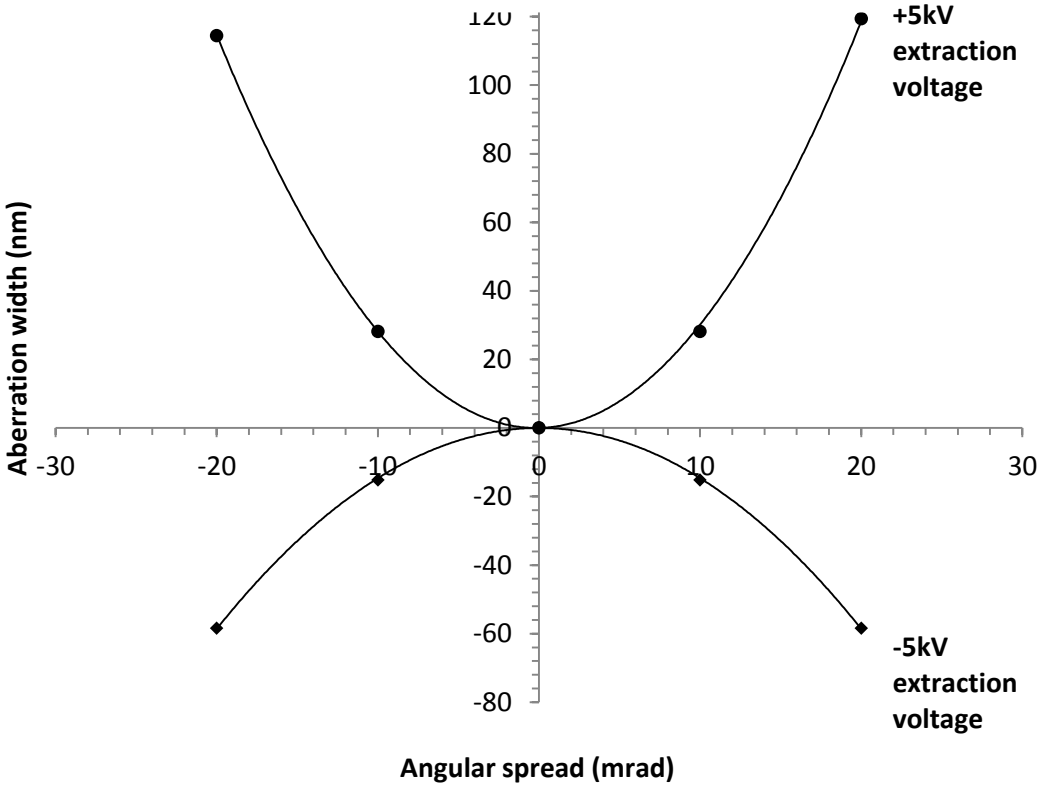

(b)

Figure 4.12: Simulation of the fringe field effect created by a ± 5 kV extraction voltage on a 20 keV Gallium ion primary beam (a) Simulated equipotential lines of the fringe field in uniform steps (b) Simulated aberration width at the specimen as a function of angular spread in the primary beam.

4.3.3 Mass resolution predictions for the mass analyser design

Figure 4.13 shows that the simulated mass resolution limited by an energy spread of ±3%, is more than a magnitude better with compensation, than for the case of no compensation. The predicted mass resolution limited by ± 3% energy dispersion with compensation is 592, and is 33 without compensation. The average predicted mass resolution limited by spherical aberration (± 25 mrad angular spread) on the horizontal detector plane is 415, better than the flat detector plane monochromatic case, which has an average of 371, indicating that there is some degree of spherical aberration cancellation also taking place.

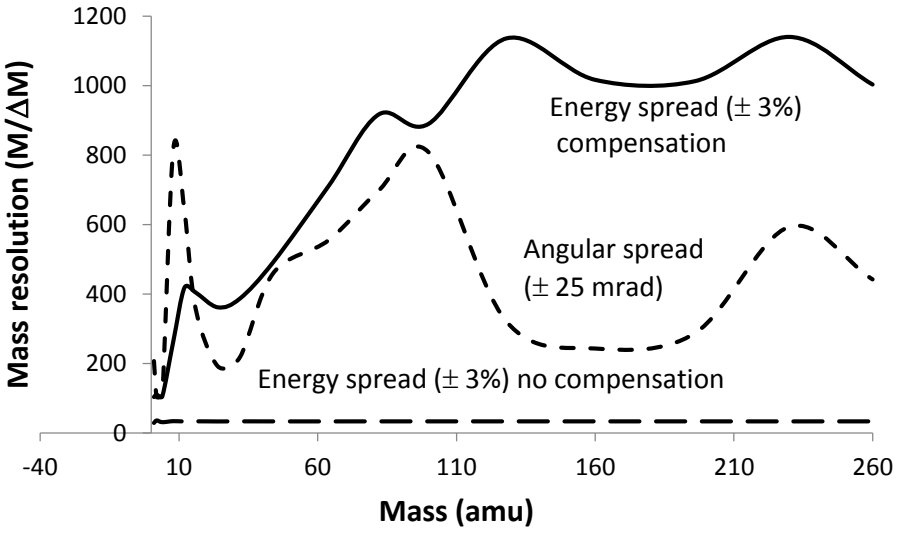

Figure 4.13: Simulated mass resolution for the magnetic box scalar potential design for an angular spread ± 25 mrad with and without energy spread compensation.

The Nano SIMS reported by Cameca [4.6] is the only commercial SIMS that is able to perform parallel mass spectrometry at present. It utilizes a co-axial arrangement of deflection for the secondary ions, where the primary beam and secondary ions travel in opposite directions along the same axis and have opposite charge, in this way, the secondary ions are deflected away from the primary beam axis. This arrangement has the advantage of being able to place the primary beam column closer to the specimen than in the conventional SIMS system, where the primary beam travels on to the specimen from one side (as in Figure 4.12a). After deflection, the secondary ions go through an electrostatic sector deflector and then on to a Mattauch-Herzog (parallel) spectrometer design. It is not possible to make a direct comparison of the present parallel magnetic box spectrometer predictions with the Nano SIMS design, since the present simulations have been performed for quite different field conditions above the specimen, they do not model the co-axial system of deflection. It is in principle possible for the Nano SIMS system to use the parallel magnetic spectrometer as reported here. The Nano SIMS spans a mass range of 21 times (maximum mass/minimum mass) and 7 masses can be measured in parallel. The current box analyser is able to achieve a much wider maximum to minimum mass ratio (of 260 times), and there may be advantages in considering it for an instrument such as the Nano SIMS instrument, however more simulations are required before a valid comparison can be made, simulations which need to include the deflection action of the co-axial unit.

One disadvantage of proposing the present parallel magnetic box spectrometer as an attachment for FIB instruments is that the secondary ion sputtering yield for a Gallium beam is around two orders of magnitude lower than conventional SIMS primary beams (Cesium or Oxygen ions), however, this can be compensated by using oxygen flooding [4.1].

4.4 An engineering prototype for the parallel magnetic box mass analyser design

A more realistic model of the magnetic box analyser design was carried out by using the simulation program Lorentz 3EM [4.4], which can solve for magnetic field distributions in three dimensions, taking into account magnetic saturation effects. The schmeatic of the 3D simulation model used in this case is shown in Figure 4.14 with details given in Figure 4.15.

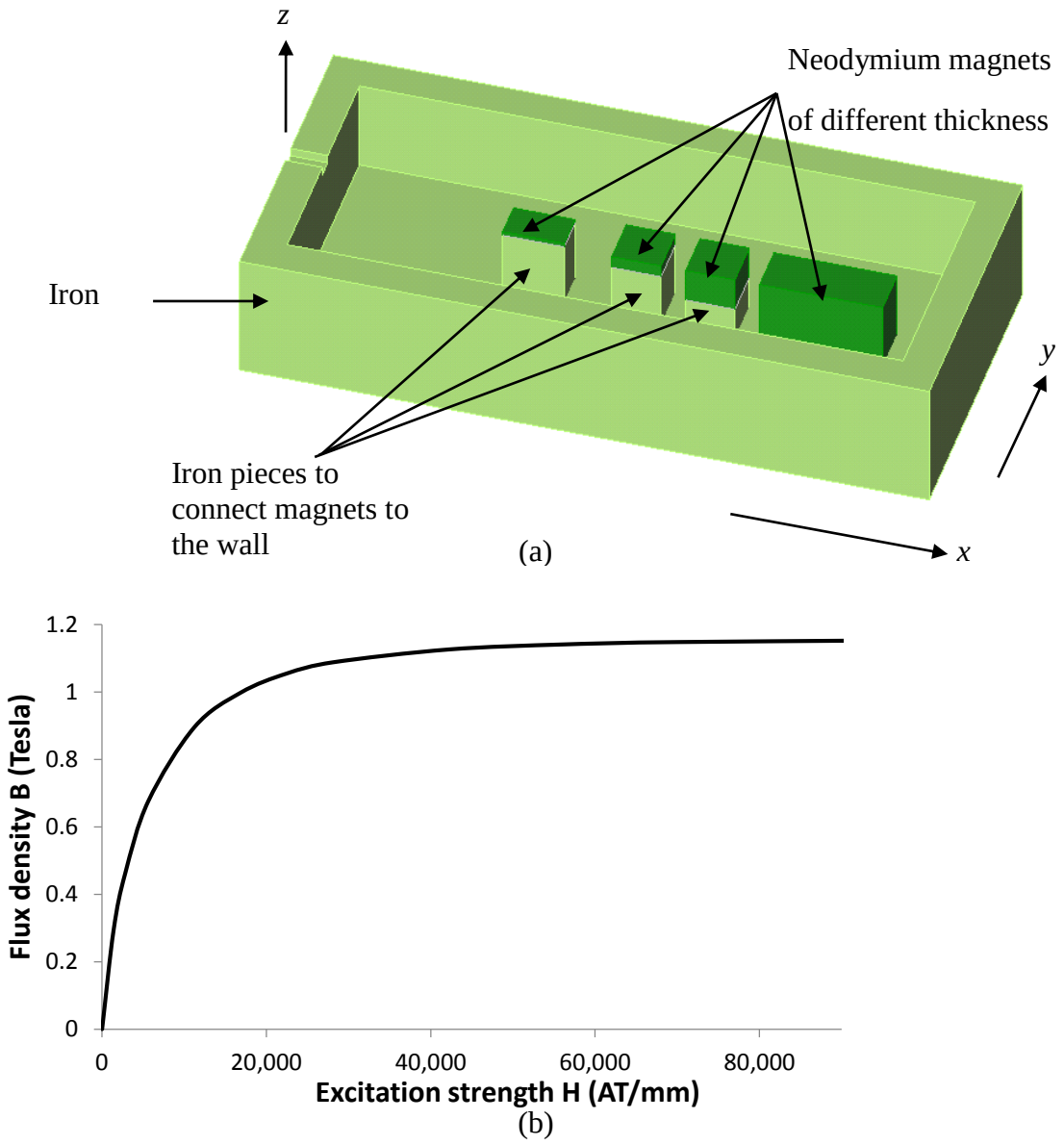

Figure 4.14: Schematic of the 3D simulation model solved in Lorentz program that takes into account permanent magnet/iron B-H curves. (a) Magnetic sector box analyser (only half of box shown in the z-direction) (b) B-H curve specified for the permanent magnets.

Figure 4.14a indicates the presence of Neodymium permanent magnets (darker regions) of differing heights in the z-direction, only half the box is shown. The coercive force (H_c) for these magnets was set to 11,250 AT/cm, and their B-H curve characteristic as specified in the Lorentz 3EM program is shown in Figure 4.14b. The B-H curve of all iron regions was also taken into account (by the commonly known "1018 mild steel" material). The height of each permanent magnet was adjusted to provide the same excitation strength set in the previous magnetic scalar potential design, shown in Figure 4.4. In order for the contour plots to closely resemble those obtained from the previous scalar potential solution, the dimensions of the box had to be scaled up by a factor of 5 in order to circumvent the effects of material saturation. Lorentz simulated results also indicated that the maximum field strength obtained by the inclusion of magnetic saturation is around 23% lower than the one obtained with the scalar potential model. To compensate for this, the height of the strongest pair of magnets was increased, changing its excitation strength from 14,400 AT to 20,000 AT, as shown in Figure 4.15.

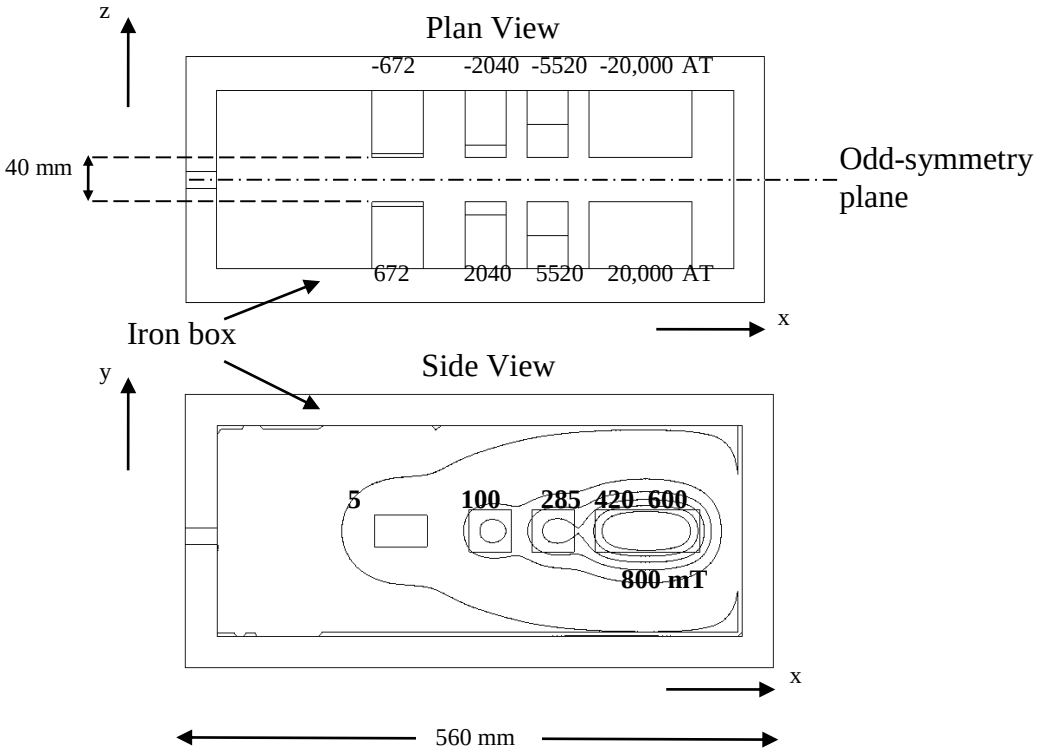

Figure 4.15: Simulated field distribution of box analyser design with B-H curves of permanent magnets and the iron material taken into account. Dotted lines indicate contours of equal magnetic field strength along the central odd-symmetry plane.

Various attempts of making a smaller magnetic box analyser keeping the original magnetic scalar potential layout were tried by tweaking the magnetic configuration. The simulation results indicated that scaling down the box size naturally led to poorer predicted output resolution, the effects of magnetic saturation were difficult to circumvent when the dimensions of the magnetic box analyser was made smaller. One such smaller box design, 190 mm long, is shown in Figure 4.16.

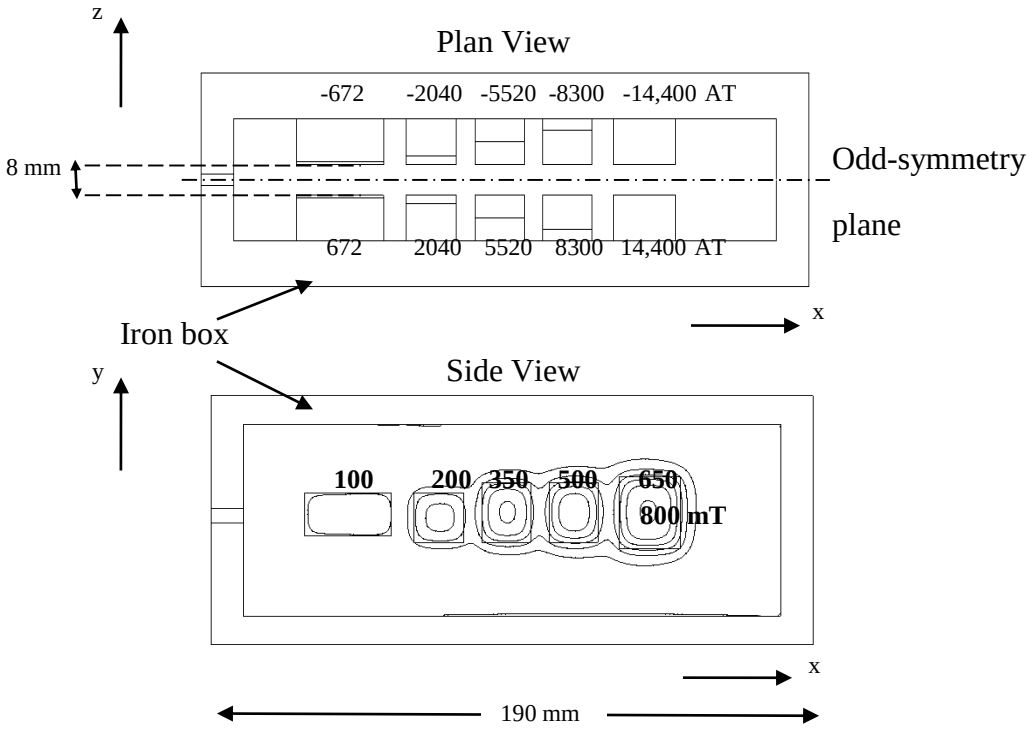

Figure 4.16: Simulated field distribution of a smaller magnetic box analyser design.

Although the dimensions of the box are over a factor of 2.5 times smaller than the box of 560 mm in length, the maximum field strength still lies below 1 Tesla. The dimensions and positions of the permanent magnets were changed, in order to obtain focusing on an approximately straight detector plane. The magnets were also placed closer together in the *x*-direction, and an additional pair of magnets were inserted at the end of the box to improve the focusing properties of the magnetic box analyser. Figure 4.17 shows simulated ray paths of selected 1 keV ions through the smaller analyser box design, indicating that the detector plane is now tilted.

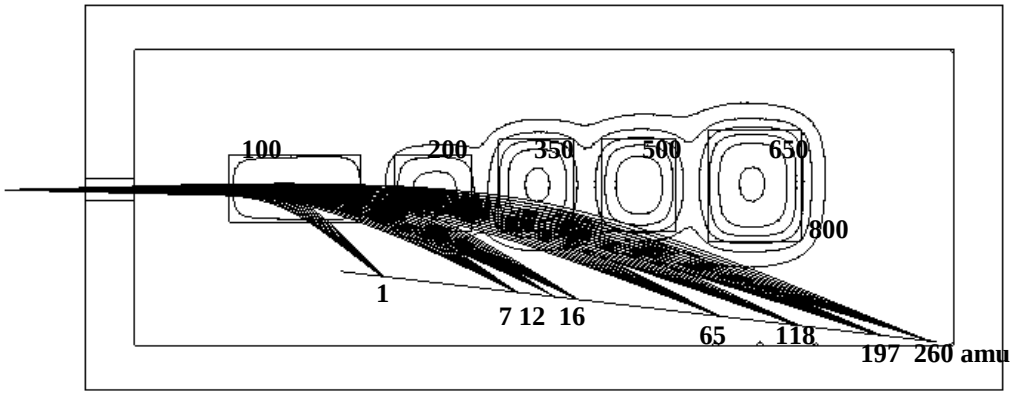

Figure 4.17: Simulated 1 keV ion trajectories through a 190 mm long magnetic box analyser design. The input angular spread ranges from -25 to 25 mrad.

The focusing optics of the smaller 190 mm long analyser box design are predicted to be considerably worse than for the 550 mm long box. Figure 4.18 shows simulated rays paths of 7, 8, 200 and 210 amu around the detector plane for an input angular spread of ± 25 mrad.

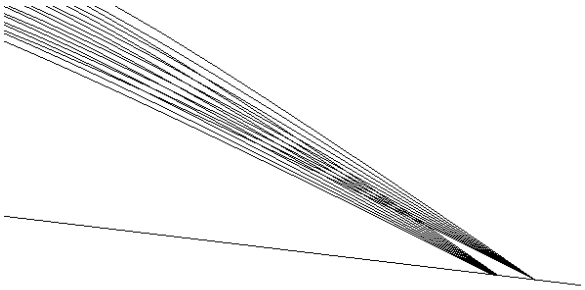

7 8 amu

(a)

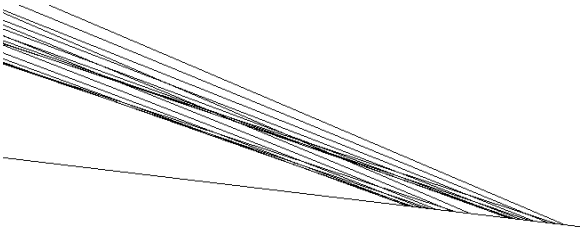

200 210 amu

(b)

Figure 4.18: Simulated ray paths around the detector plane in the smaller magnetic box analyser design for selected ions. (a) 7 and 8 amu (b) 200 and 210 amu.

The calculated mass resolution from the 7/8 amu trajectories is 166, while for the 200/210 amu trajectories, it is 103. In general, the mass resolution varies between a minimum value of 62.5

to a maximum value of 200 for the mass range of 1 to 260 amu. The average predicted mass resolution limited by spherical aberration (± 25 mrad angular spread) on the straight detector plane is 112. This value is over a factor of 3 times worse than the mass resolution of the 550 mm long box design, which has an average mass resolution of 371 for the same mass range. While the simulated results show that smaller parallel magnetic box analyser designs (190 mm long) may be possible, they also reveal that their focusing properties are worse than the bigger box analyser designs (560 mm long).

The more accurate Lorentz simulation results indicated that a FIB mass spectrometer based upon the Khursheed et al. parallel magnetic box energy analyser design cannot be small enough to fit into a FIB specimen chamber as an add-on attachment, as originally proposed [4.7]. It typically needs to be around half a meter long, and this therefore points towards it being an external attachment that fits onto the FIB specimen chamber. It is also of interest for creating a dedicated wide-range parallel mass SIMS instrument.

4.5 Limitations of Secondary Ion Mass Spectrometry (SIMS) on the nano-scale

Any proposal for performing SIMS on the nano-scale needs to take into account the inevitable reduction of the output signal strength due to the irradiation area on the specimen being smaller and whether a statistically significant number of secondary ions can be detected, so that the results are meaningful. If the probe size for instance, is smaller than conventional SIMS by a factor of ten, there will naturally be 100 times less secondary ions to form the output signal. A sample of area 10 nm square will contain ~2000 surface atoms, not all of which will be atoms of interest. Assuming that the probability of ionization is 10% (with a boost from O or Cs), then 30 ions will be transmitted. If 10% of the atoms in the surface are unknowns that need to be analysed, then only about 3 of them will reach the detection plane per 10 nm square area. To obtain a statistically meaningful number of detected ions would require an order of one hundred 10 nm square areas (an area of 100 nm by 100 nm), or the willingness to penetrate many tens of nm deep into the sample. Although this is an important restriction, there are some possibilities to overcome it.

The data from one pixel is usually not considered on its own. It is the data from an array of pixels (an image) that is assessed in relating statistical significance, usually by correlation methods. This might mean the correlation of two images from secondary ions that would be expected from a single compound, for example Al^+ and AlO^+ produced on the sputtering of alumina. As SIMS information is often acquired over an image, therefore the final signal may be averaged over many similar features. Levi-Setti et al. successfully applied a Ga^+ probe of around 50 nm used to sputter Ca+ and 44 Ca+ on imaging chromosomes structures, 31 chromosome samples in a single image were used to form the output signal [4.8]. The images contain very familiar chromosome shapes and data from several (10 to 20) similar shapes have been isolated and averaged to produce isotopic abundances with errors of 5% or less. It is also

possible to use correlation methods over several images. The parallel SIMS signal detection adds to this advantage by producing these images simultaneously, greatly speeding up data-acquisition times, as compared to conventional SIMS systems.

4.6 Conclusions

This chapter has presented parallel magnetic sector mass analyser designs in which ions are simultaneously detected on a straight detector plane for a mass range of 1 to 260 amu. Simulation results predict that second-order focusing can be achieved for several regions in the detected mass spectrum. The analyser is predicted to have an average mass resolution limited by spherical aberration of 611 for an input angular spread of ± 25 mrad along its intrinsic focal plane, which when projected on a horizontal detector plane, drops to 371. For energy dispersion correction via the use of an electric sector, the average predicted mass resolution limited by spherical aberration (± 25 mrad angular spread) on the horizontal detector plane is 415. The predicted mass resolution limited by chromatic aberration is 592 where the energy spread is ± 60 eV around an emission energy of 2 keV (± 3%). The simulation results predict that it should be possible to perform secondary ion mass spectroscopy analysis on the nanoscale range with the proposed mass spectrometer attachment. They predict that for a 560 mm long parallel magnetic box analyser design, saturation effects can be compensated by readjustment of magnet excitation strengths. Simulation results also indicate that although it may be possible to design a smaller parallel magnetic box analyser (190 mm long), its focusing properties are likely to be worse than the bigger parallel magnetic box analyser.

References

[4.1] L. Li, D.S. McPhail, N. Yakovlev, H. Seng, Strategies for improving the sensitivity of FIB-SIMS, Surface and Interface Analysis, 43 (2011) 495-497.

[4.2] A. Khursheed, K. Nelliyan, F. Chao, First-order focusing parallel electron energy magnetic sector analyzer designs, Nuclear Instruments and Methods in Physics Research Section A: Accelerators, Spectrometers, Detectors and Associated Equipment, 645 (2011) 248-252.

[4.3] A. Khursheed, Khursheed Electron Optics Software (KEOS), in, Electrical and Computer Engineering Department, National University of Singapore.

[4.4] Lorentz-3EM, Integrated Engineering Software Inc., Canada, 2011.

[4.5] A. Khursheed, K.H. Cheong, H.Q. Hoang, Design of a parallel mass spectrometer for focused ion beam columns, Journal of Vacuum Science & Technology B: Microelectronics and Nanometer Structures, 28 (2010) C6F10.

[4.6] NanoSIMS 50/50L, in: Cameca (Ed.), http://www.cameca.com/instruments-for-research/nanosims.aspx.

[4.7] K.H. Cheong, A. Khursheed, A parallel magnetic sector mass analyzer design, Nuclear Instruments and Methods in Physics Research Section A: Accelerators, Spectrometers, Detectors and Associated Equipment, 645 (2011) 221-226.

[4.8] R. Levi-Setti, K.L. Gavrilov, P.L. Strissel, R. Strick, Ion microprobe imaging of -labeled mammalian chromosomes, Applied Surface Science, 231-232 (2004) 479-484.

Chapter 5 : A Parallel Radial Mirror Analyser (PRMA) attachment for the SEM

5.1 Introduction

In chapter 1, the Parallel Radial Mirror Analyser (PRMA) proposed by Khursheed et al. [5.1] was cited as a promising new wide-band multi-analyser attachment design for the SEM, particularly for carrying out Auger Electron Spectroscopy (AES). It has many advantages over the Hyperbolic Field Analyser (HFA) [5.2], the electric field multi-channel analyser design that had previously been proposed for AES in the SEM (also mentioned in chapter 1). Unlike the HFA, it has a fully rotationally symmetric detection plane (2 π collection in the azimuthal direction) and is predicted to have second-order focusing properties for all electrons that are detected. The HFA was reported to have second-order focusing properties for only one pass energy [5.3], and this is why the PRMA's simulated energy resolution is predicted to be a factor of around 6 times better than the HFA (below 0.2 % for a polar angular spread of $\pm$ 3º). The theoretical transmittance of the PRMA is over two orders of magnitude higher the transmittance of the HFA. This advantage comes from its fully rotationally symmetric detection plane [5.1].

Although the PRMA design has significant transmittance and energy resolution advantages over the HFA, it is a much more complicated analyser design, which poses new problems of its own, both in terms of practical implementation and design optimisation. The purpose of this chapter is to develop a feasible engineering design for the PRMA from which a working prototype can be made.

The first difficulty of the PRMA design is its multi-electrode complexity. Figure 5.1 compares the PRMA electrode layout to the design principle of the HFA.

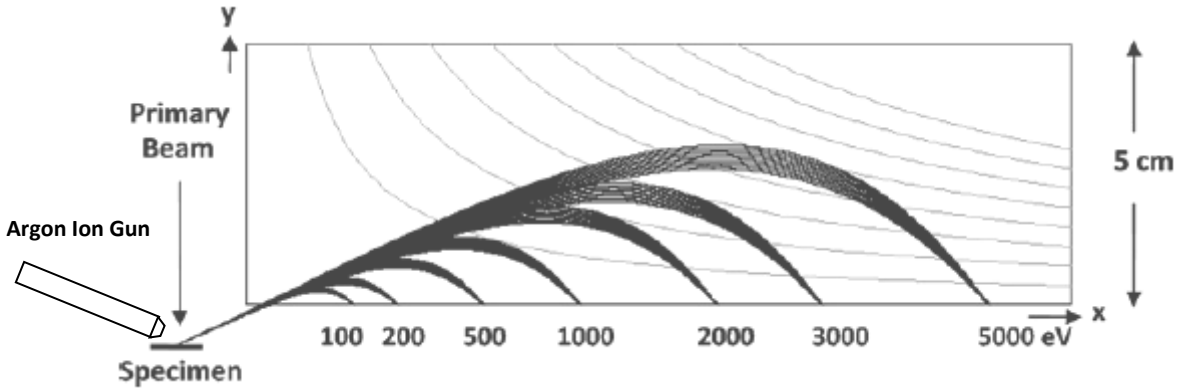

(a)

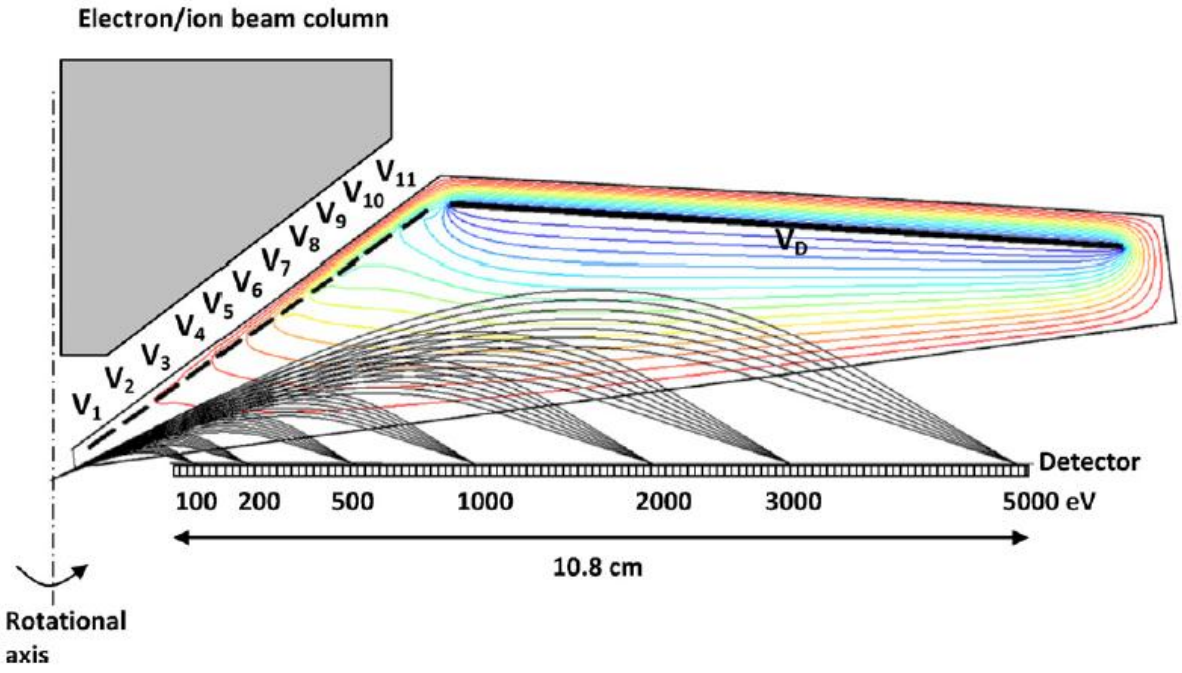

(b)

Figure 5.1: Comparison of the PRMA and HFA designs. (a) Ray tracing simulation of HFA [5.1] (b) Ray tracing simulation of PRMA [5.1].

The potential field distribution within the HFA is described by the following simple analytical equation:

$$V(x,y) = \frac{2V_0}{R_0^2} xy \qquad (5.1)$$

where V_0 is the potential on a curved hyperbolic shaped electrode whose tip (at $x = y$) is located a distance R_0 from the analyser bottom left-hand corner ($x = 0$, $y = 0$). The potential on the bottom and left-hand side boundaries of the analyser are fixed to be zero volts, and an ideal grid or detector is assumed to lie at the bottom boundary. Note that the distance R_0 here, corresponds to $\sqrt{2}$ times the variable *b* used by Jacka et al. [5.3]. The ray tracing here was carried out by Khursheed et al. [5.1]. Eleven trajectories from the specimen (located outside the analyser) are evenly plot over a polar angular spread of −1.1º to 1.1º around a central entrance polar angle of 25º with respect to the *x* axis for the electron energies of 100, 200, 500, 1000, 2000, 3000, and 5000 eV. Equipotential lines of 500–4000 V in 500 V steps are also indicated. The HFA layout shown in Figure 5.1a is similar to the one reported to have a single second-order focusing point at 100 eV, and first-order focusing properties for all other energies [5.2, 5.4], where the energy (E) to voltage ratio (V_0) for R_0 = 14.14 mm is 1.19 (V_0 = −84.03 V). However, Khursheed et al. predict that the second-order focusing occurs instead at 50 eV.

In comparison to the HFA's simple guiding analytical potential distribution (given by equation 1), the PRMA has a numerically solved field distribution that is created by twelve different electrode voltages (V_1 to V_{11} and V_D). Khursheed et al. arrived at the PRMA design by carrying out direct ray tracing of electrons with the two-dimensional commercial Lorentz 2EM software [5.5]. These simulations were performed manually, that is, both the analyser geometry and

electrode voltages were varied by trial and error while monitoring the energy resolution on a horizontal detection plane in rotationally symmetric coordinates (r, z). The first and most important task in this work is therefore to establish whether the current PRMA design is an optimal one. Is there a set of electrode voltages that provide a better energy resolution or wider energy pass range on the detector plane? What compromise in the energy resolution has been made by forcing all focusing points to be on a flat horizontal plane, how much better is the analyser's intrinsic energy resolution?

An impractical feature of the PRMA's current design is that the working distance (the distance from the specimen to the entrance of the analyser), is relatively small, only 3.5 mm, and this needs to be increased to at least 5 mm in order to make room for other instrumentation that must be placed close to the specimen in the SEM chamber. Just how the predicted energy resolution on the detector plane varies with working distance needs to be investigated. Another important practical consideration is the need to take into account fringe field effects due to the entrance/exit grids. Unlike the HFA, where the analyser horizontal bottom plane defines the detection plane, in the PRMA, electrons travel through the bottom plane at relatively shallow angles and are focused on a horizontal detection plane that lies outside the analyser, in a field-free region. The effect of fringe fields created by grid non-uniformities at the analyser bottom plane are expected to be significant, and their effect can only be simulated by the use of a fully three-dimensionally ray tracing program. In this present work, the effect of different grid layouts on the energy resolution will be simulated through the use of Lorentz 3EM, a commercial three-dimensional ray tracing programme [5.5].

Beyond better simulation of the PRMA design, there is the challenge of finding a suitable detector. A flat position sensitive electron detector that is multi-channel in the radial direction and rotationally symmetric in the azimuthal direction requires a curvilinear shaped position sensitive detector. Conventional electron position sensitive detectors do not usually have this geometry, they are usually fabricated in rectilinear coordinates, where the pixel shape is square or rectangular. The most commonly available type of electron position sensitive detectors is one dimensional in nature, and this makes the design of a suitable position detection system for the PRMA a challenging task. The work presented in this chapter develops a practical viable design strategy for the PRMA detector based upon the use of channeltron arrays. It goes on to make a prototype of a more optimal and practical PRMA design, and obtain preliminary results of it functioning as an energy analyser attachment inside a SEM.

5.2 Redesign of the PRMA by the use of the Damped least-squares method

The DLS method can be used together with ray tracing to optimise the PRMA to make a more practical design (already described in chapter 2). The DLS method of optimisation is first applied to extending the analyser working distance to more than 5mm without compromising the relative energy resolution considerably. The parameters to be adjusted for the PRMA are twelve electrode voltages, while the parameter to be minimized is the average output relative energy resolution (which includes 30 different energies). Optimisation of electrode voltages was carried out with and without the constraint of the detection plane being flat (lying on a horizontal plane).

Figure 5.2 shows the graph of simulated average relative energy for different analyser working distances. If the analyser working distance is extended beyond 8 mm, the average relative energy resolution is predicted to grow by around a factor of two (over 0.30%). For an analyser working distance of 7 mm (with the optimal polar emission angle for the central ray found to be 24.2^{o}), simulation results predict that the average relative energy resolution on a horizontal detector plane will grow from 0.14% (corresponding to the current working distance of 3.5 mm) to 0.23%, indicating that the working distance of the PRMA can be doubled without significantly degrading its average relative energy resolution.

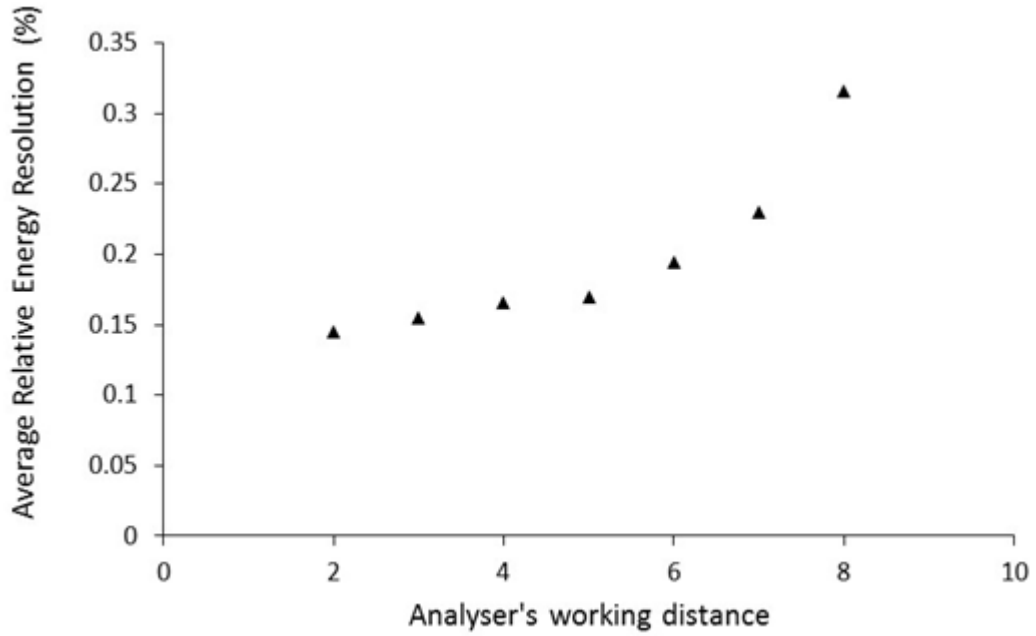

Figure 5.2: Simulated average relative energy resolution as a function of analyser's working distance on a horizontal detector plane.

Figure 5.3 shows the simulated trajectory paths through the PRMA design for an analyser working distance of 7 mm after applying the DLS optimization method. Equipotential lines plot from -176 to -2464V in uniform steps of -176V are also indicated. At each energy, seven trajectories are plot evenly between −3º and 3º around a 24.2º polar entrance angle. The electrode voltages V_1 to V_{11} and V_D are: -12.93V, -83.46V, -203.47V, -318.67V, -480.19V, -688.30V, -927.95V, -1247.89V, -1439.97V, -1519.95V, -1760V and -2639.84V. The central ray of the polar entrance angle was found to be 24.2º after optimization.

The new electrode voltages corresponding to the 7 mm analyser's working distance were all observed to be lower than that for the 3.5 mm case. In particular, the new and old electrode voltages were within a difference of 1% (i.e. 0.41 to 3.16V in terms of absolute number) for V_4 to V_d; and within 2 to 5% (i.e. up to 0.05V in terms of absolute number) for V_2 and V_3. The largest change was observed in the first electrode voltage, V_1 from -17 to -12.93V.

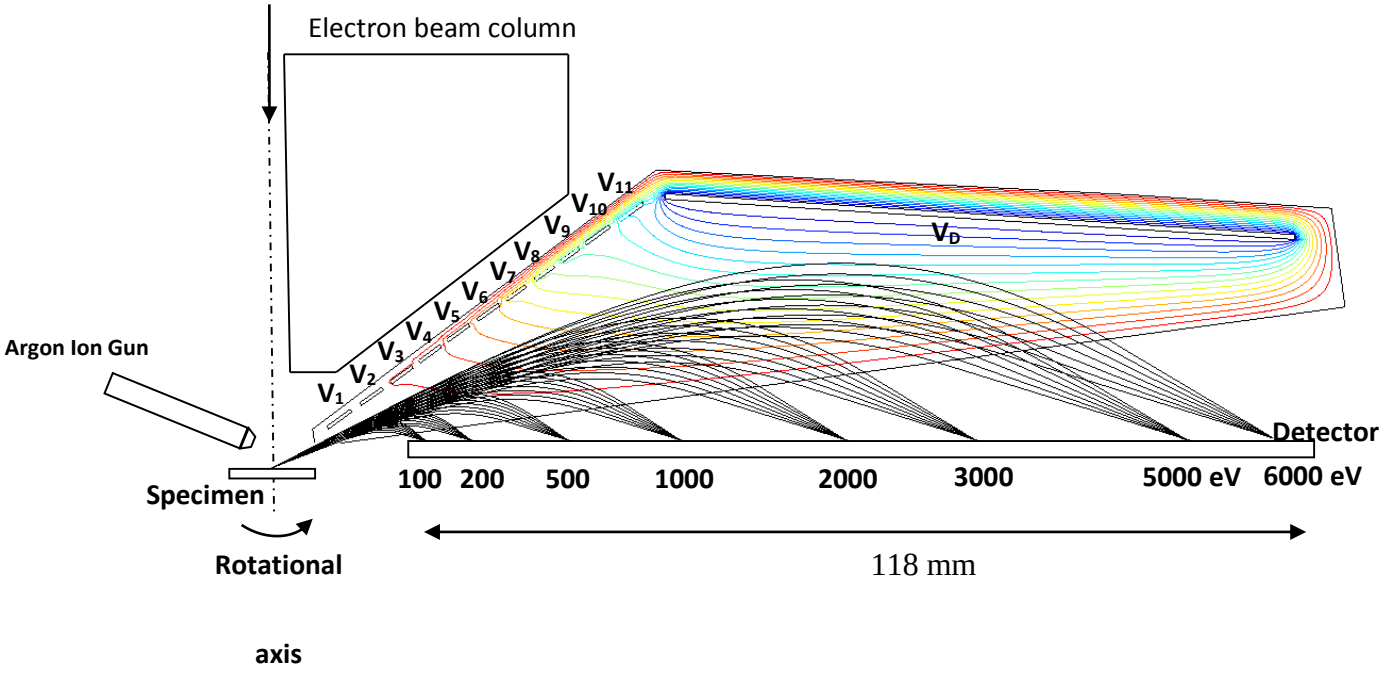

Figure 5.3: Simulated trajectory paths through the second-order focusing PRMA design. Equipotential lines plot from -176 to -2464V in uniform steps of -110V are also indicated. At each energy, seven trajectories are plot evenly between −3º and 3º around a 24.2º polar entrance angle. The electrode voltages V_1 to V_{11} and V_D are: -12.93V, -83.46V, -203.47V, -318.67V, -480.19V, -688.30V, -927.95V, -1247.89V, -1439.97V, -1519.95V, -1760V and -2639.84V.

The transmittance of the analyser, *T*, can be calculated by the following expression [5.6]

$$T = \frac{(\phi_2 - \phi_1)}{4\pi}(\cos 2\theta_1 - \cos 2\theta_2) \qquad (2)$$

Where θ_1 to θ_2 represents analyser entrance angles in the polar direction, and ϕ_1 to ϕ_2 are analyser entrance angles in the azimuthal directions. This formula assumes that electrons have a cosine emission angular distribution. For an engineering prototype to be placed within the SEM chamber, let us assume that the PRMA is constructed in the form of a sector module which extends 90º in the azimuthal direction. For a ± 3º polar angular spread around the central angle of a 24.2º, the transmission is 1.94%, assuming no loss in transmission due to the exit grid. This is over an order of magnitude higher than the HFA for a similar polar angular spread.

Figure 5.4a shows ray tracing around the output focal plane at selected energies for an angular spread of ±3º in uniform steps of 1º for the new PRMA design (analyser working distance of 7 mm), 1% above and below the energies of 600, 2000, 3500 and 5000 eV are plot. They indicate that the predicted energy resolution (corresponding to the half-width of the central ray) is around 0.2% for a wide range of energies. Figure 5.4b depicts the simulated trace-width as a function of polar angular spread, they have second-order focusing properties (3rd order geometrical aberration trace-width shape). Trace-width diagrams like these were obtained for other energies, confirming that second-order focusing is predicted over the entire electron energy range of detection.

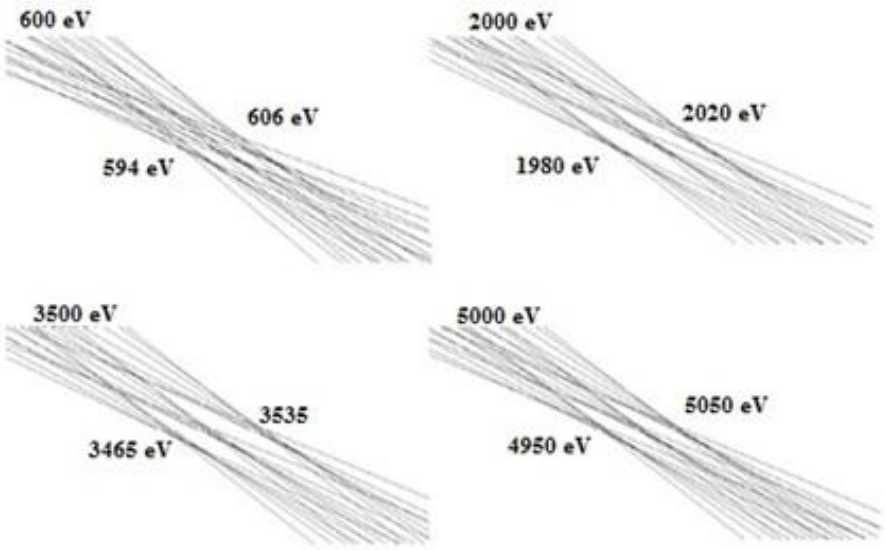

(a)

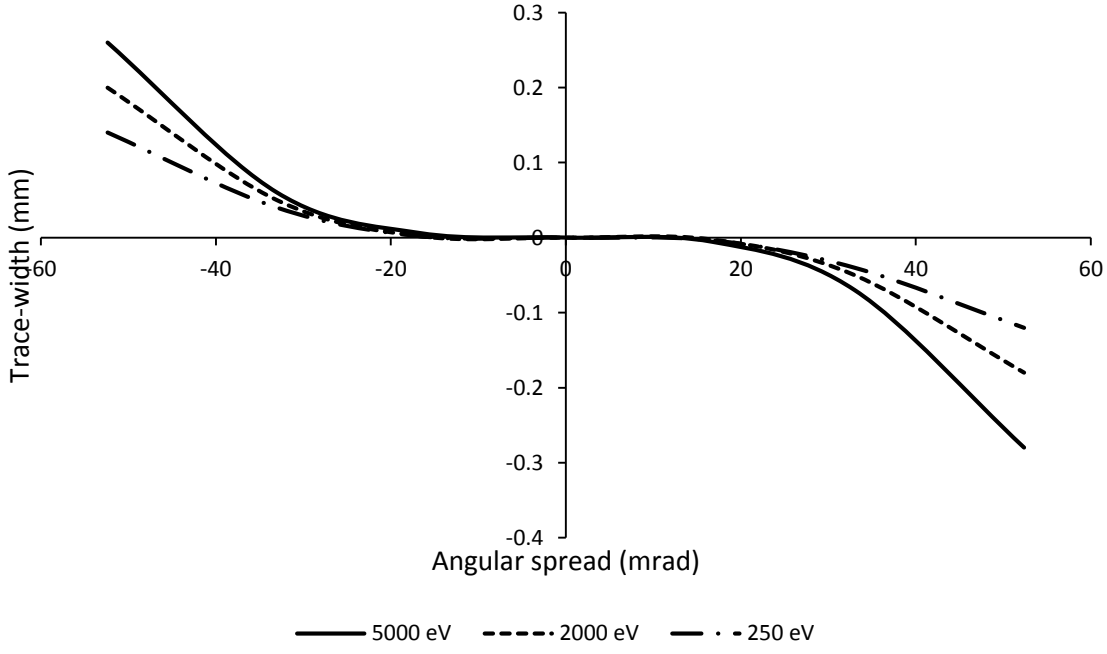

(b)

Figure 5.4: Simulated characteristics on the focal plane at selected energies of the PRMA design, for an angular spread of ±3º in uniform steps of 1º. (a) Trajectory paths with energies at ±1% below and above the central energies of 600, 2000, 3500 and 5000 eV (b) Trace-width as a function of polar angular spread on the Gaussian focal plane at selected energies. The polar angular spread ranges from −3º to +3º.

Figure 5.5 shows the simulated energy dispersion along the detector plane, and shows that the sensitivity of landing position (gradient) is greatest for the lower energies. The simulation results in Figure 5.4 and Figure 5.5 are similar to the ones in the original PRMA design [5.1], indicating that second-order focusing properties are still being retained despite having a larger analyser working distance.

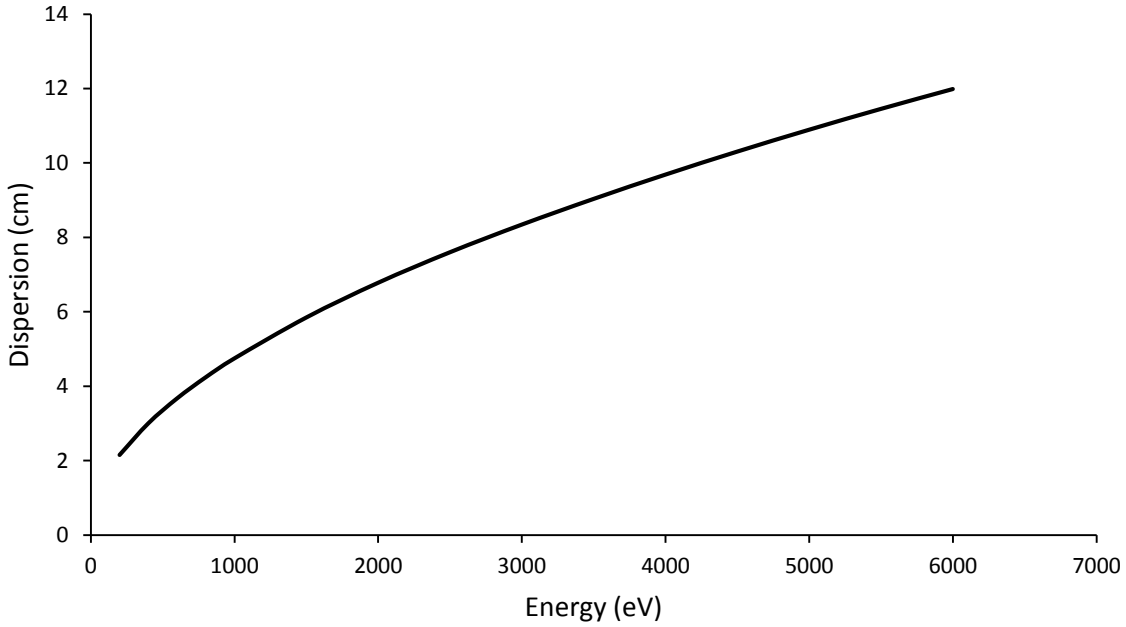

Figure 5.5: Simulated energy dispersion characteristics of the PRMA design along its horizontal detector plane.

With this improved version of the PRMA, further simulations are carried out to determine its field of view and depth of focus. Figure 5.6a illustrates how the simulated average relative energy resolution for the new PRMA design is expected to vary with different off-axis positions of the primary beam. It indicates that for within ±0.5 mm on either side of the rotational axis, the average energy resolution is around 0.25%. Within the SEM, the PRMA is therefore expected to have a relatively large field of view, that is, the average energy resolution will not be significantly degraded for different points within a ± 500 μm field of view. Figure 5.6b

indicates that the PRMA design is also expected to have a large depth of focus, the average energy resolution is below 0.5% when the specimen is misplaced vertically by ±0.5 mm. Since the precision on specimen stage positioning in the SEM is usually in the tens of micron range, or better, misplacement of specimen is not expected to affect the energy resolution at the detector plane.

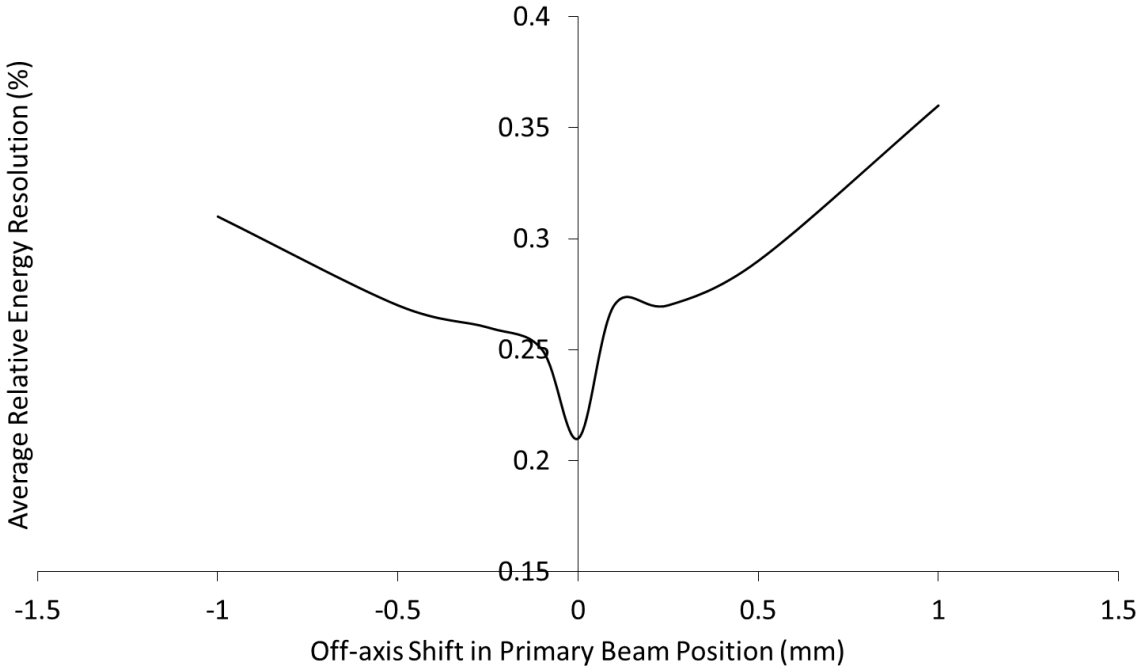

(a)

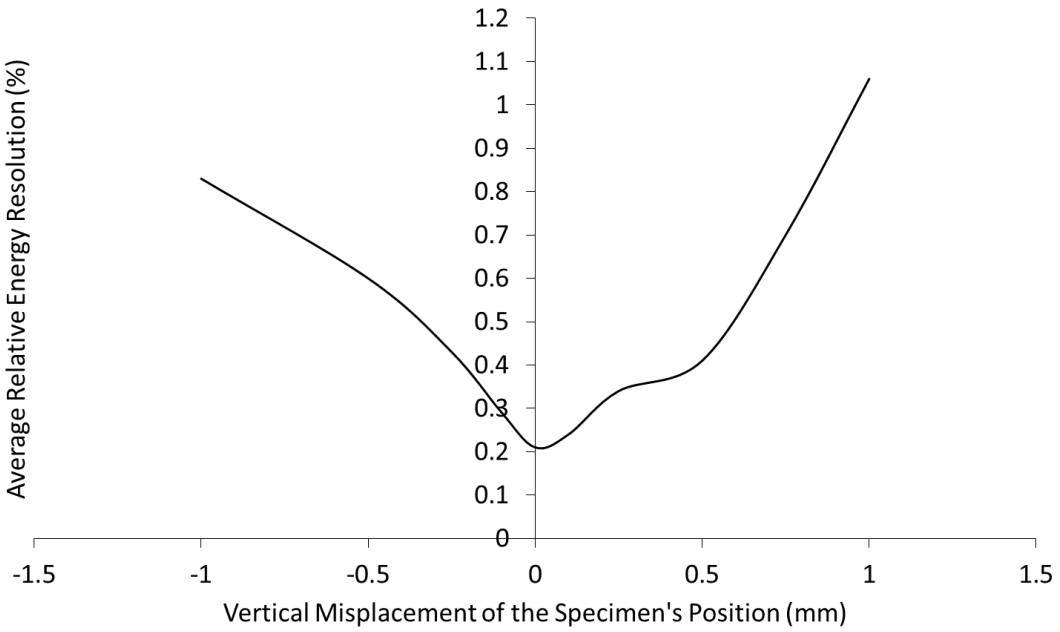

(b)

Figure 5.6: Simulated average relative energy resolution for: (a) Corresponding off-axis shift in primary beam position (b) Corresponding vertical misplacement of the specimen's position.

Figure 5.7 shows a comparison of the simulated relative energy resolution for the PRMA design in comparison with HFA design at a polar angular spread of ± 3°. For a polar angular spread of ± 3°, the average relative energy resolution for the HFA and PRMA design (with a working distance of 7 mm) is 1.528% and 0.23% respectively on the detector plane across the entire electron energy range of 100 eV to 5000 eV. For most of the energy range, the PRMA design has an energy resolution that is around 7.5 times better than the HFA. The simulated results presented in Figure 5.7 show that the energy resolution is not expected to degrade significantly by detecting electrons on a horizontal detector plane (as compared to the intrinsic focal plane). Since the PRMA suffers from relatively poor energy resolution in the lower energy range (< 200 eV), the detection range of the energy analyser can be shifted to a higher range, located further away from the analyser entrance plane. Further simulation results reveal that the predicted relative energy resolution on its intrinsic plane at a polar angular spread of ± 3° remains around 0.2% for the energy range up to 8,000 eV.

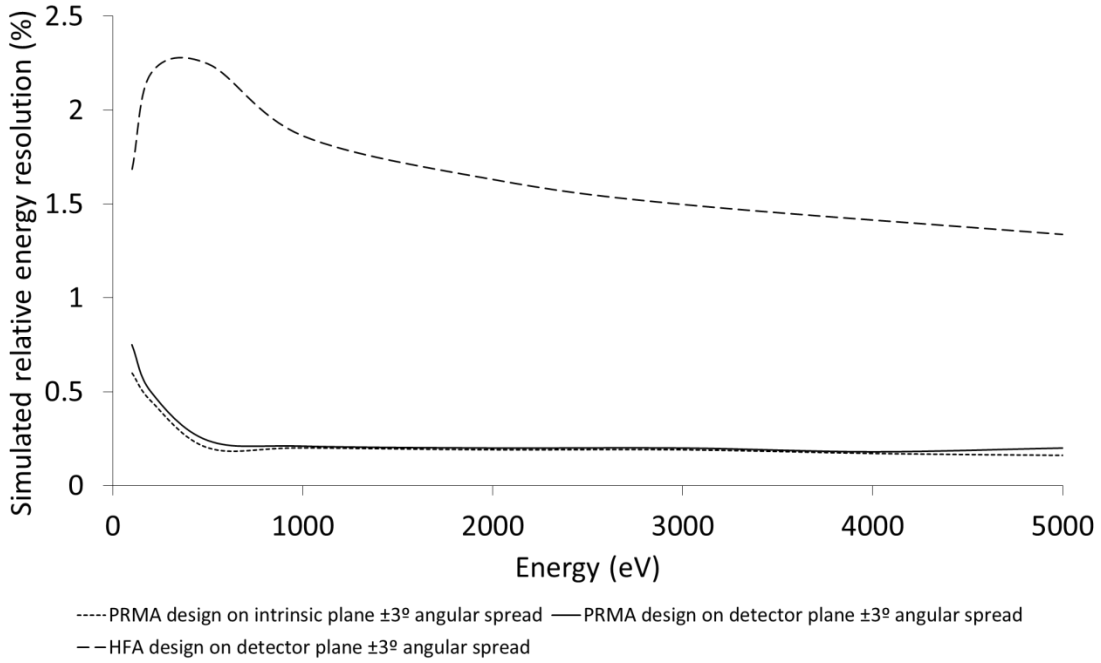

Figure 5.7: Simulated relative energy resolution for the PRMA design as a function of energy in comparison with the HFA for a polar angular spread of ± 3°.

5.3 Three-dimensional simulation of Exit Grid effects

Several grid designs were analysed by use of the Lorentz 3EM program. Each of them was assessed in terms of its adverse effect on the energy resolution for 90% transparency. Figure 5.8 shows 3 possible exit grids designs (not drawn to scale): (a) a square grid design, (b) a radial slot design and (c) a layered radial slot design. The square grid design is the one that is most readily available commercially. However, one limitation of the square grid design is that it is not rotationally symmetrical and causes greater scattering of electrons. The radial slot grid is designed to reduce the degree of scattering, however, a radial slot design suffers from the limitation that the separation between each wire increases in the radial direction. As the separation of the wires increases, leakage fields become larger and degrades the focusing properties of the analyser. The radial slot design is similar to a curvilinear grid, but does not have the tangential wires in between to distort the electrostatic field. The layered slot grid is

designed to maintain similar separation distance between wires as a function of radius, and thereby reduce fringe field effects.

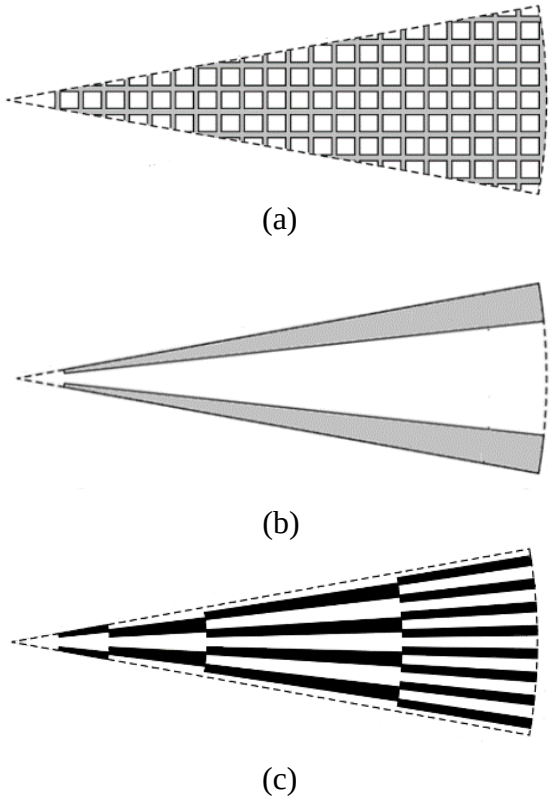

Figure 5.8: Schematic diagram of 3 possible exit grids design (not drawn to scale) represented by a repeating sector with periodic boundary. (a) Square grid design, (b) Radial slot design and (c) Layered radial slot design.

Simulation results in Figure 5.9 predict that the fringe field effects due to the square grid is likely to produce relative energy resolution that is considerably worse than those obtained by the other two grid layouts in the lower half of the energy range. The average relative energy resolution for the square grid, radial slot and layered radial slot designs are 0.36%, 0.27% and 0.25% respectively (for 90% grid transparency). These simulation results indicate that the radial slot and layered radial slot grids are the better ones to use. These simulation results also

indicate that the introduction of an appropriate exit grid design is not going to significantly degrade the focusing properties of the analyser for most the energy range, and it is the focusing properties of the analyser at the lower energy region that will be affected the most. Since the relative energy resolution of the analyser is already worse for the lower energy range (< 200 eV), this is another reason for moving the energy detection range to a higher one, say from 200 eV to 8 KeV.

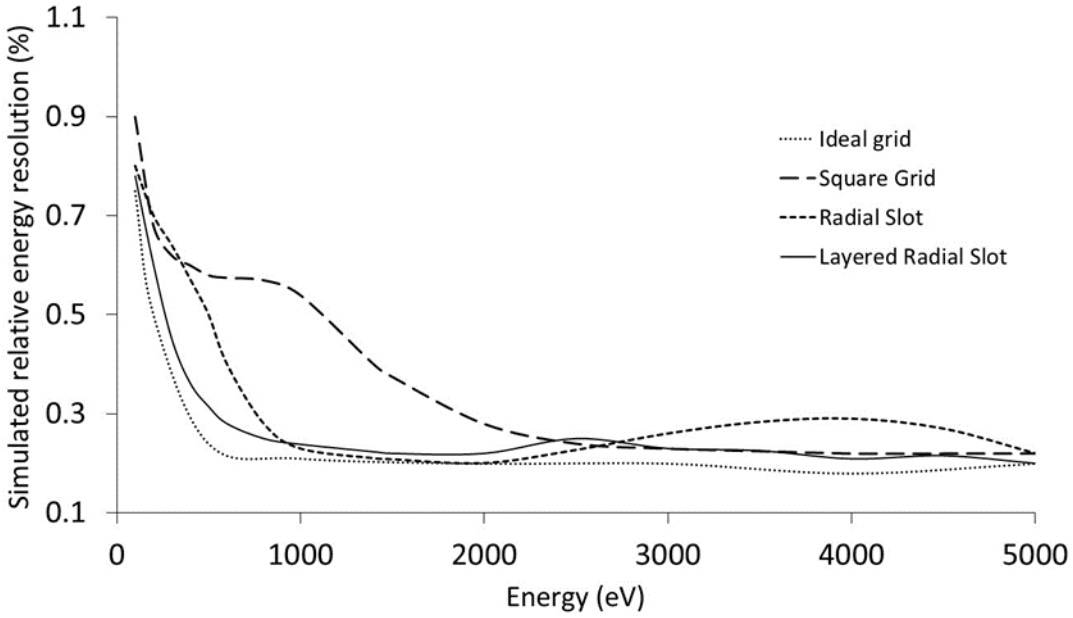

Figure 5.9: Simulated energy resolution for each energy level for the PRMA using (i) ideal grid, (ii) square grid, (iii) radial slot and (iv) layered radial slot.

5.4 The PRMA prototype as a SEM attachment

5.4.1 Experimental setup

A PRMA was designed to fit into the specimen chamber of a Philips XL30 ESEM-FEG, as shown in Figure 5.10. The prototype was made in the form of a sector module extending 110º in the azimuthal direction, although, only a small fraction of this angular range was used in practice due to detector constraints. The linear feed-through flange adapter held the PRMA prototype in place, so that a short SEM working distance (of 15 mm) could be achieved.

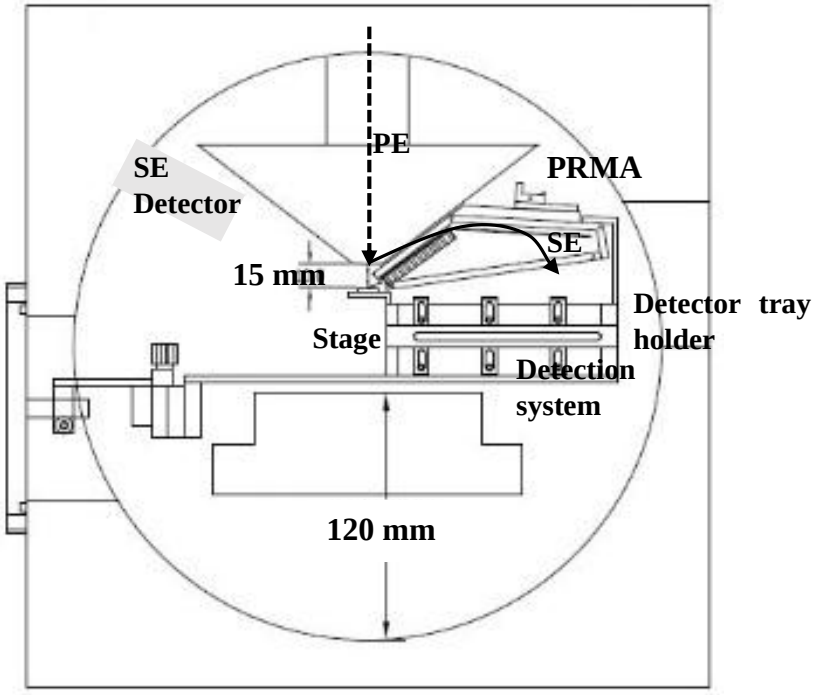

Figure 5.10: Experimental layout of the PRMA inside the Philips XL30 ESEM-FEG chamber.

The conductors in the PRMA prototype were made from aluminium, with the outer body chemically milled. Based on the simulation model, the electrodes should follow the conical body of the PRMA. These electrodes were manufactured as a planar sheet as shown in Figure 5.11. Guide holes were created at the end of each electrode to aid in the electrodes conforming

to the conical body of the PRMA when placed at the appropriate position. To ensure alignment of the electrodes, partially etched spacer bars were connected to the end of each electrode. Once all electrode fixings were in place (with reference from the guide holes), the spacer bars were then removed.

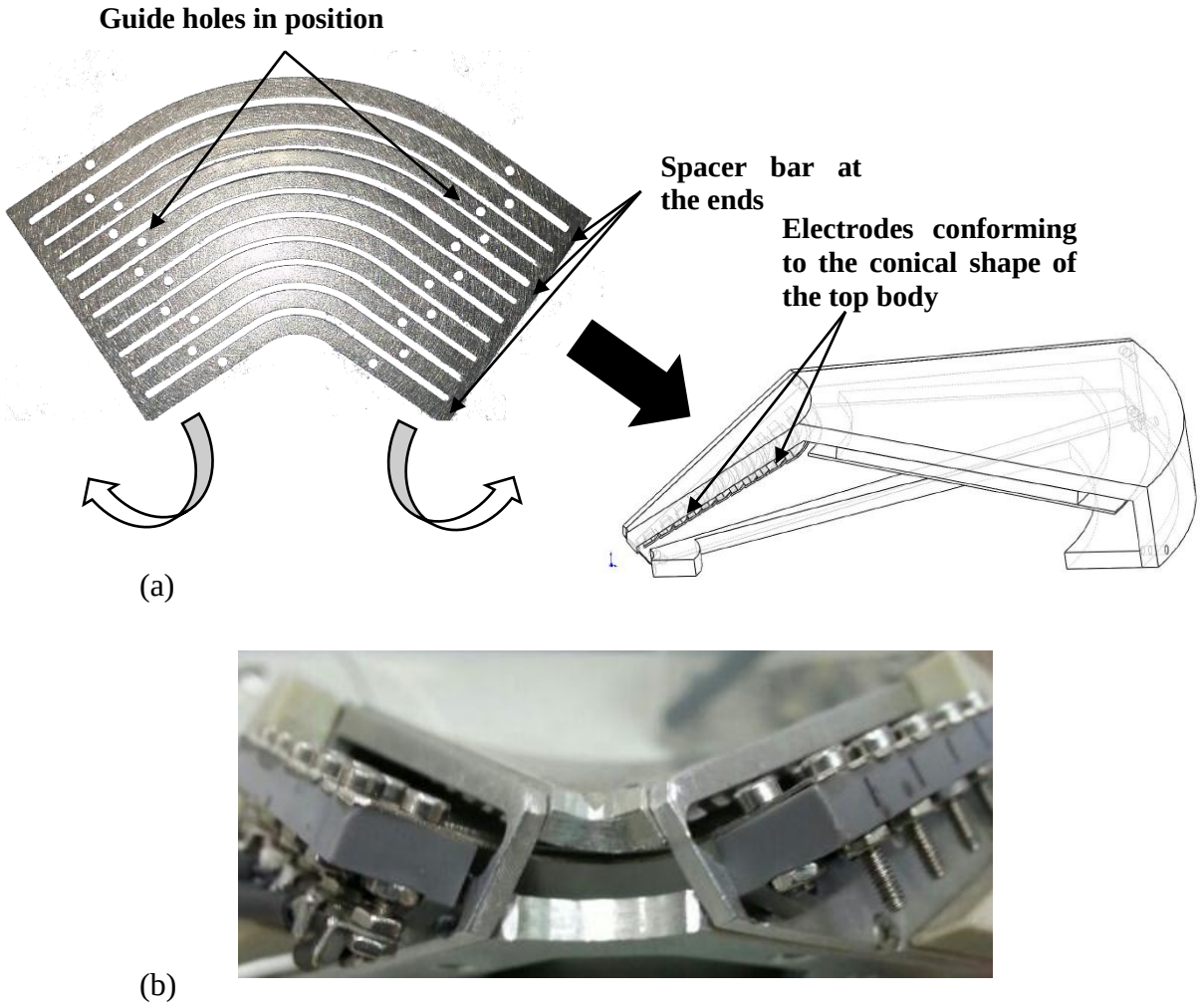

Figure 5.11: Guide holes were created at the end of each electrode. This aids in the electrodes conforming to the conical shape of the top body of the PRMA when placed at the appropriate position.

Each electrode is connected to the next one by a variable resistor located above an insulator at the top of the PRMA. The variable resistor chain, enables a single power supply to be

distributed appropriately between the electrodes (with values as shown in Figure 5.12), producing the desired potential field distribution. The potential-divider is designed to allow fine-tuning of the electrodes to their respective potentials without affecting the others along the variable resistor chain. The analyser field strength is therefore scaled by adjusting the power supply. Photographs of the constructed prototype are given in Figure 5.13.

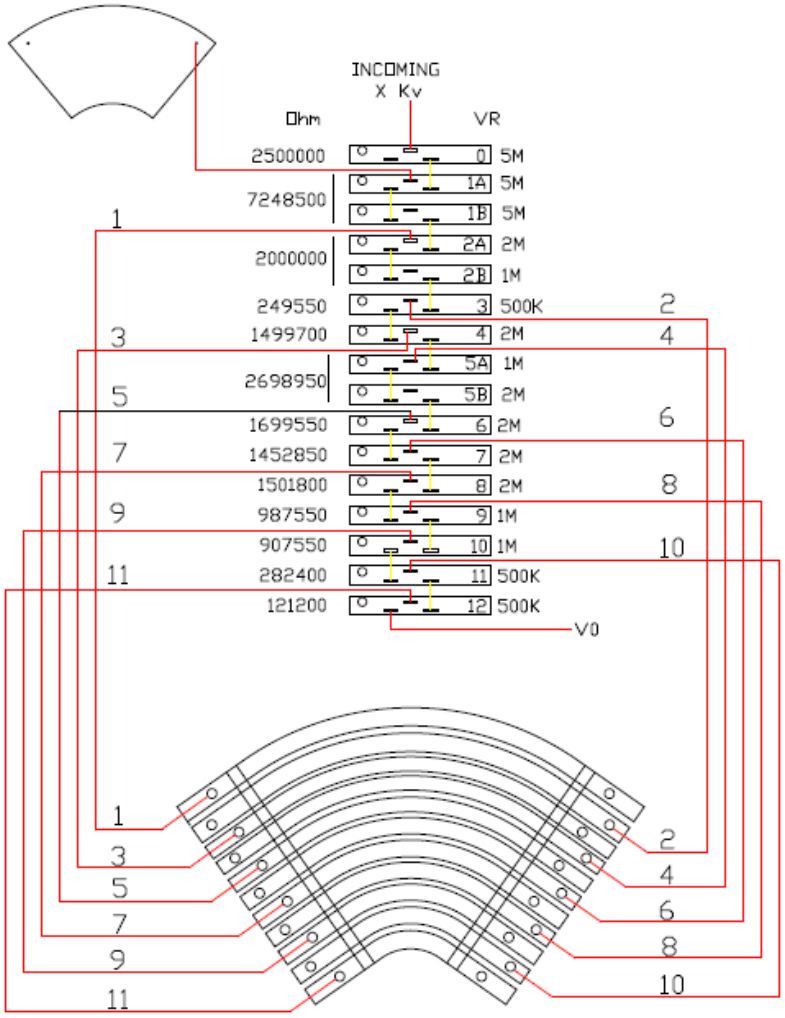

Figure 5.12: Schematic of the variable resistor chain to be used inside the SEM chamber to provide the appropriate potentials to the electrodes, to approximate the desired field in the simulation model.

(a) (b)

Figure 5.13: Photograph of the PRMA prototype. (a) As viewed from the top (b) As viewed from the side.

The primary beam was focused onto a spot on the surface of the specimen. For these initial proof-of-concept experiments, a single photomultiplier (PMT) with scintillator unit was placed at a single location on the detection plane, towards the high end of the energy spectrum. Figure 5.14 shows a photograph of the PMT, Hamamatsu-10271 with scintillator used.

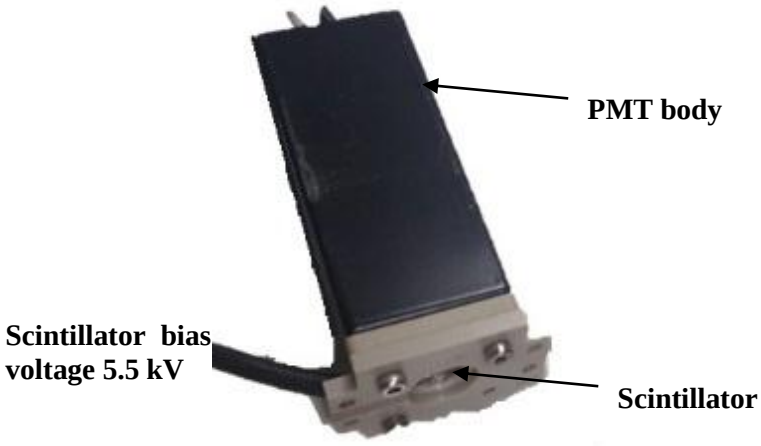

Figure 5.14: Photograph of the photomultiplier (PMT) with scintillator used in the experimental setup.

The scattered secondary electron energy distribution was obtained by ramping the deflection voltage of the analyser (V_{DEF}) and monitoring the PMT output, where the deflection voltage is

directly related to the SE energy. A PC was used to control V_{DEF} and the PMT current was measured by a Keitley 617 electrometer and monitored by PC through a National Instruments Data Acquisition (DAQ) board. The deflection voltage was ramped in steps of 0.5V and each point had a primary beam dwell time of ~150 ms (for the case of 1 sample per point). The SE analyser signal was collected from regions that were exposed to the primary beam for the first time in order to minimize the effects of contamination. At a primary beam energy of 5 keV, the beam current was measured to be 150 pA.

The PMT body was covered with grounded metallic foil to prevent charging of the dielectric material. For the acquisition of SE spectra, the scintillator voltage, V_{SC}, was biased to +5.5 kV. The PMT was placed inside a detector tray holder and covered by a grounded aperture slit. The grids used for the experiments had 80% transmission with a hole size of 112 μm and wire width of 14.7 μm. The grid was grounded by connection to the body of the PRMA.

5.4.2 Preliminary spectral results

A Silicon (Si) wafer specimen coated with Silver (Ag) of 500 nm thickness was used. Initial tests suffered from a weak SE signal, and the entrance slot of the prototype was enlarged to widen the entrance polar spread to ±4.5º (up from the previous ±3º) around the central ray of 24.2º. Figure 5.15 shows experimentally acquired SE spectra. The number of samples for each value of the deflection voltage was varied from 100, 200 and 400. The scale in Figure 5.15 is transformed into energy by multiplying the deflection voltage by 1.5 derived by simulation.

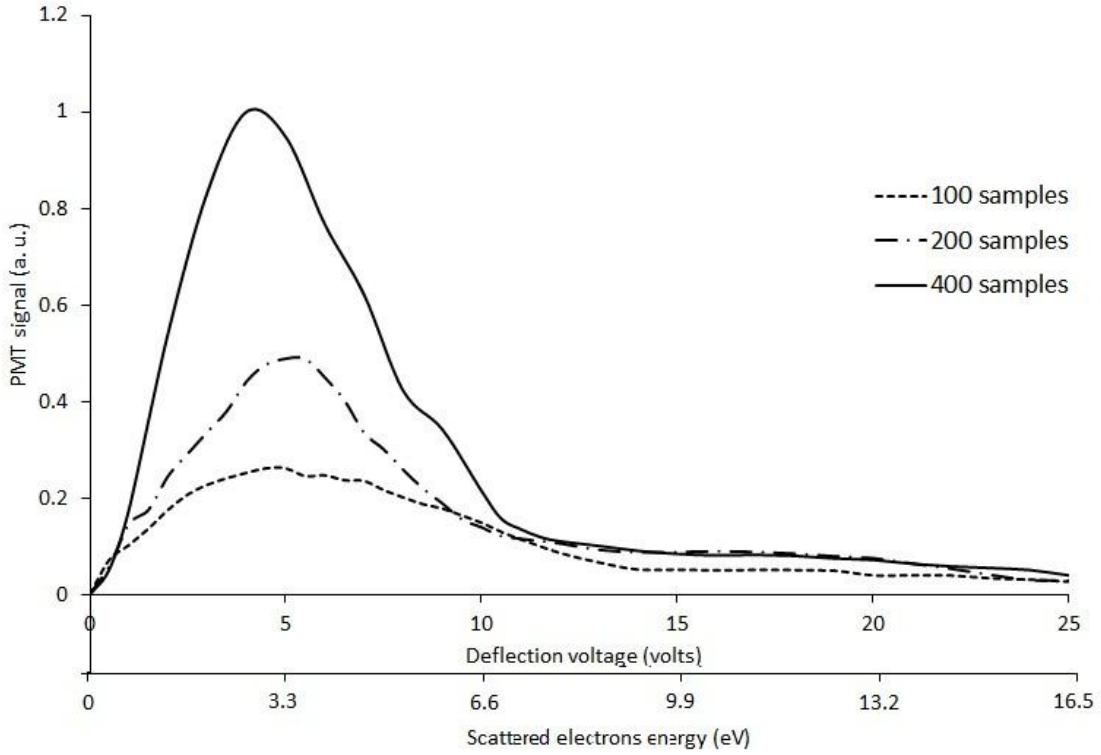

Figure 5.15: Experimental analyser signals obtained from a Silicon (Si) wafer specimen coated with Silver (Ag) of 500 nm thickness for 100, 200 and 400 samples. A primary beam acceleration voltage of 5 kV was used.

The experimentally obtained spectrum for the 400 samples curve was then fit to the SE Chung-Everhart energy distribution [5.6], as illustrated in Figure 5.16. It shows that the shape of the predicted and experimentally obtained curves generally match and this further validates that the experimentally obtained spectrum was indeed an SE spectrum. The work function for the best fit case was found to be 5.4 eV (whereas work function of Silver is 4.7 eV). The difference is most likely due to the effects of contamination on the specimen. The obvious mismatch for higher energies may be due to the misplacement of the primary beam relative to the analyser rotational axis, since there was no mechanism to align them.

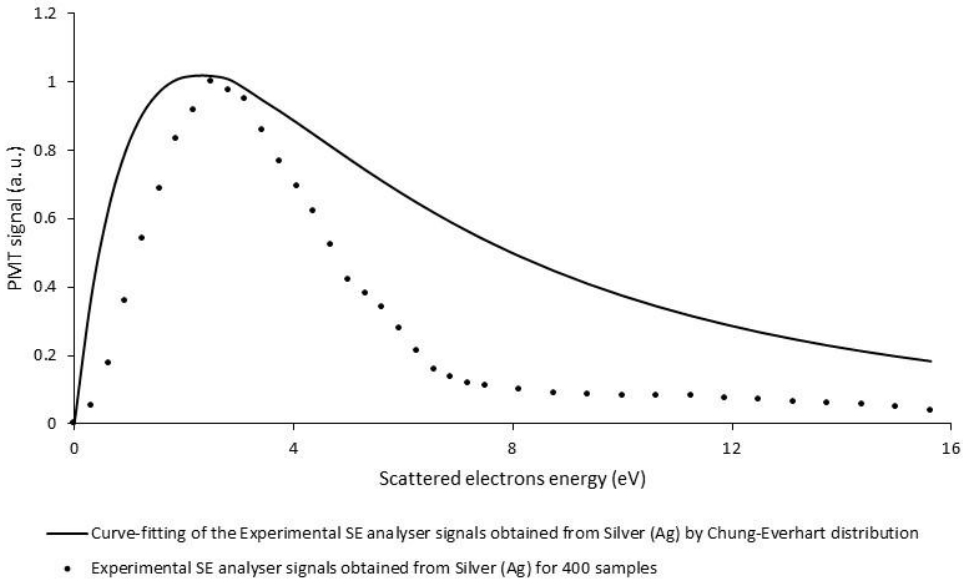

Figure 5.16: Curve-fitting of the experimental SE analyser signals obtained from Silver (Ag) by the Chung-Everhart distribution.

Table 5.1 quantifies the signal-to-noise ratio (SNR) at the signal peak position. The SNR increases by roughly $\sqrt{2}$ as the number of samples is doubled from N = 100 to 200 and to 400, indicating that the background noise is shot-noise [5.7, 5.8] in the SE energy range. The experimental results shown in Figures 5.15 and 5.16 and Table 5.1 provide preliminary proof-of-principle results to demonstrate that the PRMA prototype can function as a sequential energy spectrometer attachment inside a SEM.

No. of samples, N	**Signal-to-noise ratio (SNR) at the signal peak**
100	741
200	1221
400	1743

Table 5.1: Signal-to-noise ratio (at the signal peak) for the experimentally acquired SE analyser signals corresponding to 100, 200 and 400 samples.

5.5 A hybrid parallel detection proposal

In the absence of a commercially available rotationally symmetric position sensitive detector suitable for the PRMA, the following section describes a multi-channel detection system based upon an array of channeltrons/slit apertures which can be used in combination with ramping the analyser deflector voltage in time. This hybrid detection system has already been proposed for the Magnetic Box Analyser in chapter 3, since each channeltron now captures a different portion of the energy range, the scan time, compared to a single sequential detector, is reduced by the number of channeltrons used. The slit apertures are placed on the analyser detection plane. A schematic for this multi-channel proposal is shown in Figure 5.17.

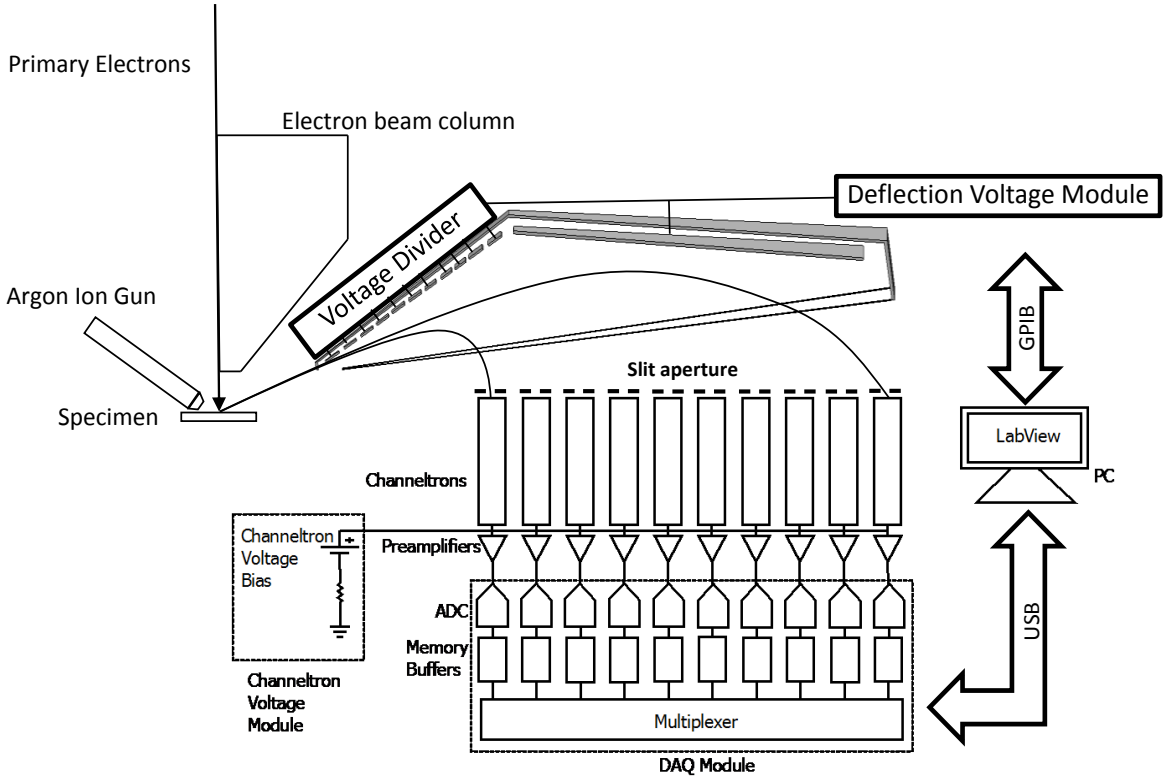

Figure 5.17: Signal acquisition block diagram for the PRMA channeltron array detection system.

The signal from each channeltron is amplified and stored separately in its own dedicated memory buffer. Only one deflection voltage is ramped in time, suitably divided and

synchronized to the DAQ card capturing the signals from the channeltron array. Once the deflection voltage is scanned, the data is fed by the DAQ to a PC via a fast USB connection. Subsequent averaging and processing, such as normalizing the relative signal strength from each channeltron can be done in software form. Figure 5.18 shows a photograph of a channeltron and its electrical connections. The channeltron operates in an analogue mode and a transimpedance amplifier was implemented to convert the current signal from the channeltrons to a voltage signal with a transimpedance factor of 10^6 ohms. A low-pass filter was also implemented to remove the background noise (80 Hz).

It should be noted that in each channel, the high voltage supply at the channeltron output is decoupled by a capacitor before the signal is amplified by the transimpedance head amplifier. This means that the output signal of each channel will be a differentiated form of the energy spectrum. In general, a channeltron has a gain in excess of 10^8 and can come in compact sizes. The channeltrons used for the prototype analyser here were manufactured as a matched unit by Photonis and the model is Channeltron-4800. The effective angular azimuthal angular collection range is $\pm 6.5^{o}$ for the channeltron positioned furthest away from the entrance of the analyser.

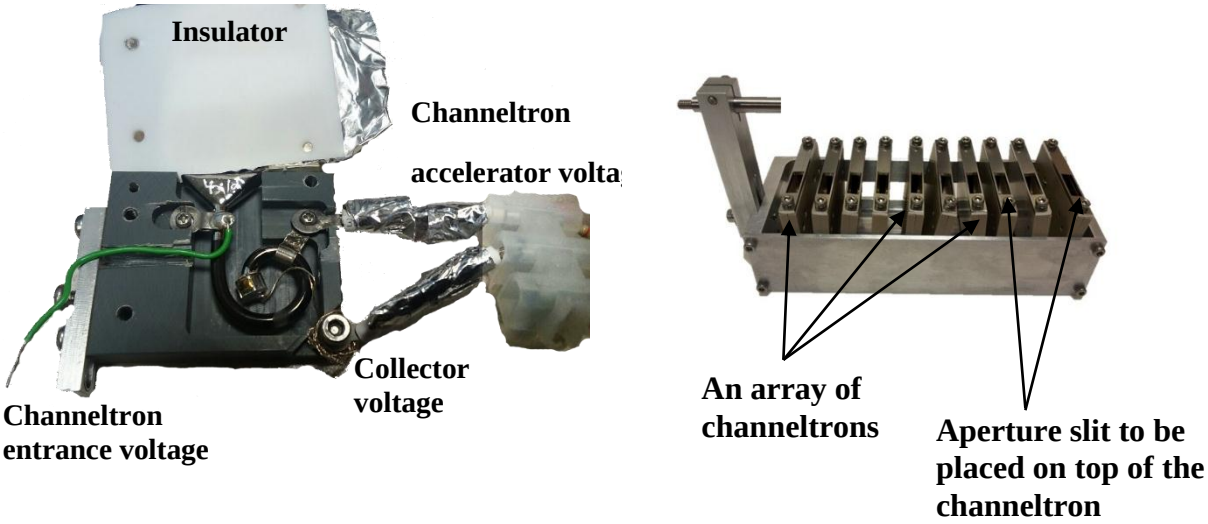

Figure 5.18: Photograph of the channeltron (a) Electrical connections to the channeltron (b) An array of channeltrons on the detector tray holder.

A simple experiment was carried out to test the channeltron detection system was working, which involved placing the channeltron detection system below the analyser, and switching the primary beam on and off. A primary beam acceleration voltage of 5 kV was used on a Silicon wafer specimen coated with Copper (Cu) of 50 nm thickness. An analogue power supply (OR-X-630 function generator) was used to vary the deflection voltage with a ramping frequency of 20 Hz. No procedure to increase the wider azimuthal angle scattered electrons was used in this experiment, and the effective azimuthal angular range in this experiment was limited to ±6.5º. When the primary beam in the SEM was switched off, the amplitude of the signal recorded on the DAQ decreased by a factor of 50. This gives an indication of the signal to noise over one scan and provides confirmation that the channeltron detection system is working. This preliminary result also highlights the need to improve the range of collection in the azimuthal angular direction, by for instance, the use of more channeltron arrays to improve its signal-to-noise ratio.

5.6 Conclusions

A practically viable engineering design for the PRMA to be used inside SEM chambers as an add-on energy spectrometer attachment has been developed. The DLS method was used to find optimal voltages on twelve electrodes in the analyser design so that that output relative energy resolution on the detector plane is minimized for a working distance of 7mm. Three-dimensional simulation that takes into account the fringe fields in various grid layouts predicts that a radial slot and layered radial slot design are the better ones to use. A PRMA prototype was made and proof-of-concept experiments were carried out for SE energy spectrum detection. A practical parallel detection system consisting of a channeltron array was also developed and tested. Preliminary experimental results to test the channeltron detection system indicate that they do collect scattered electron signals inside the SEM. They also highlight the need to provide some form of signal averaging and a means for widening the range of collection in the azimuthal angular direction in order to improve the output signal-to-noise ratio.

References

[5.1] A. Khursheed, H.Q. Hoang, A. Srinivasan, A wide-range Parallel Radial Mirror Analyzer for scanning electron/ion microscopes, Journal of Electron Spectroscopy and Related Phenomena, 184 (2012) 525-532.
[5.2] M. Jacka, M. Kirk, M.M. El Gomati, M. Prutton, A fast, parallel acquisition, electron energy analyzer: The hyperbolic field analyzer, Review of Scientific Instruments, 70 (1999) 2282.
[5.3] M. Jacka, A. Kale, N. Traitler, Hyperbolic field electron energy analyzer with second order focusing, Review of Scientific Instruments, 74 (2003) 4298.
[5.4] M. Jacka, Scanning Anger microscopy: recent progress in data analysis and instrumentation, Journal of Electron Spectroscopy and Related Phenomena, 114 (2001) 277-282.
[5.5] Lorentz-3EM, Integrated Engineering Software Inc., Canada, 2011.
[5.6] A. Khursheed, Scanning Electron Microscope Optics and Spectrometers, World Scientific, 2011.
[5.7] T.H. Wilmshurst, Signal Recovery from Noise in Electronic Instrumentation, 2nd ed., CRC Press, 1990.
[5.8] R.W. Harris, Introduction to Noise Analysis, Pion, 1974.

Chapter 6 : Conclusions and future work

6.1 Conclusions

The research work carried out for this thesis has been in the subject of developing add-on wide-band multi-channel spectrometer attachments for scanning electron/ion microscopes. Two spectrometer designs were examined, each of which involve using an array of electrodes to create complex field distributions. One spectrometer design, the Magnetic Box Analyser, uses an array of magnetic sector plates that generate a magnetic deflection field distribution inside an iron box, while the other, the Parallel Radial Mirror Analyser (PRMA), biases a set of rotationally symmetric electrodes to different voltages in order to create an electric mirror field distribution. Both of these multi-channel spectrometer designs were originally proposed in the form of idealised numerical simulations that made many simplifications and assumptions, and the main goal of this thesis has been to critically evaluate and further develop them, transforming them into realistic engineering designs from which prototype analysers can be made. This goal has been for the most part, achieved. Two wide-band multi-channel spectrometer engineering designs to function as energy analyser attachments for the Scanning Electron microscope (SEM) have been developed, one magnetic, the other electric, and in both cases, preliminary prototypes have been made. Future work should be directed towards their further experimental development and test.

An important overall conclusion that emerges from the research work carried out here, is that numerical ray tracing methods are by themselves, insufficient for successfully designing multi-channel spectrometers, they need to be used together with some form of optimisation technique such as the Damped least-squares (DLS) method. This is because, simultaneous adjustment of many voltages/excitations (over say five) in order to optimise the analyser's performance over

a large number of output channels (say over ten) is manually too cumbersome, and in practice, it leaves too many unanswered questions about how much further the analyser design can be optimised. In this thesis, a DLS program module was used in combination with the commercial Lorentz ray tracing software, both in two and three dimensions [6.1-6.2], and was found to be a robust and reliable way of optimising complex multi-channel spectrometer designs. One future recommendation is that all such direct ray tracing software, if used to design complex multi-electrode spectrometers, be combined with an optimisation module based upon methods such as DLS.

For the Magnetic Box Analyser, the simulations carried out were able to account for magnetic saturation and the 3D fringe field at the entrance slit, something which had not been previously achieved [6.3]. The analyser entrance geometry was shaped into a conical upper part so that it allows for short SEM working distances (~20 mm). The more realistic simulation design of the Magnetic Box Analyser, with the benefit of optimisation by DLS, predicts that it can in principle become a high performance wide-band energy analyser SEM attachment for Auger Electron Spectroscopy (AES). The simulated relative energy resolution is predicted to lie below 0.13% for an entrance polar angular spread of ±3˚ across the Auger electron energy range of 50 to 2500 eV. This energy resolution is typically over an order of magnitude better than previous wide-range multi-channel analysers proposed for parallel AES, such as the Hyperbolic Field Analyser (HFA). This high resolution is only predicted on the Magnetic Box Analyser on its intrinsic focal plane, if it operates to focus on a flat horizontal detector plane, the average energy resolution drops to about 0.32%. For this reason, for high energy resolution applications, it is recommended that the detection system consist of an array of discrete miniature detectors whose individual heights can be adjusted to their optimum values.

Another important aspect of the Magnetic Box Analyser emerging from simulations carried out here is that the analyser is predicted to have at least two points of third-order focusing on its detector plane. Just what it is in the analyser design that gives rise to these points of higher-order focusing needs to be investigated. There may be a way to increase the number of these higher-order focusing points and greatly improve its overall optical performance even further.

Although the possibility of the Magnetic Box Analyser design acting as the central part of a mass spectrometer attachment for Focused Ion Beam instruments (FIBs) was investigated, simulations results indicate that magnetic saturation effects prevent it from being small enough to be a compact attachment. The possibility of the analyser being used as part of a multi-channel mass spectrometer for a standalone SIMS column is feasible, although more simulations are required in order to compare it with present multi-channel SIMs systems.

A prototype of the Magnetic Box Analyser design was built, and its experimentally measured magnetic field distribution lay close to the predicted simulation field distribution, with a margin of error below 5%. The next obvious step is to experimentally test the prototype in a SEM as an energy analyser attachment. Some means of varying the sector plate excitations will be needed in practice, both for optimising the analyser's performance and for ramping the analyser deflector field strength if an array of discrete miniature detectors are used.

The second multi-channel energy analyser design, the PRMA, uses an array of electrodes to create an electric retarding field to mirror and deflect electrons through an exit grid so that they are focused onto a flat detection plane for a wide energy range (typically 50 to 2500 eV). Several design features of this analyser were altered in order to transform it into an analyser

attachment for the SEM, such as extending its working distance (from 3.5 mm to 7 mm), and three-dimensional simulation of grid fringe fields. Simulations results of the more realistic PRMA design, predict that its average relative energy resolution is around 0.2% (optimal grid layout) for a polar angular spread of ± 3º, and confirm that it has second-order properties across the entire energy range of Auger electron detection. At lower energies, the relative energy resolution goes up beyond 0.6%. One important characteristic of the PRMA design is that its simulated resolution on a flat detector plane is close to its intrinsic focal point resolution, that is, its optics is not significantly degraded by constraining its output focal plane to be a horizontal one. This means that the natural choice of detector for this analyser is a flat plane position sensitive detector.

A comparison of the simulated energy resolution for the PRMA and the Magnetic Box Analyser on its mid-plane symmetry is shown in Figure 6.1 for a polar angular spread of ± 3º. Although the Magnetic Box Analyser has an average predicted relative energy resolution that is around two times better than the PRMA, it should be noted that this factor of improvement will be drop when out-of-plane electron trajectories are taken into account, the average predicted relative resolution for both spectrometers is therefore around the same value, around 0.2%.

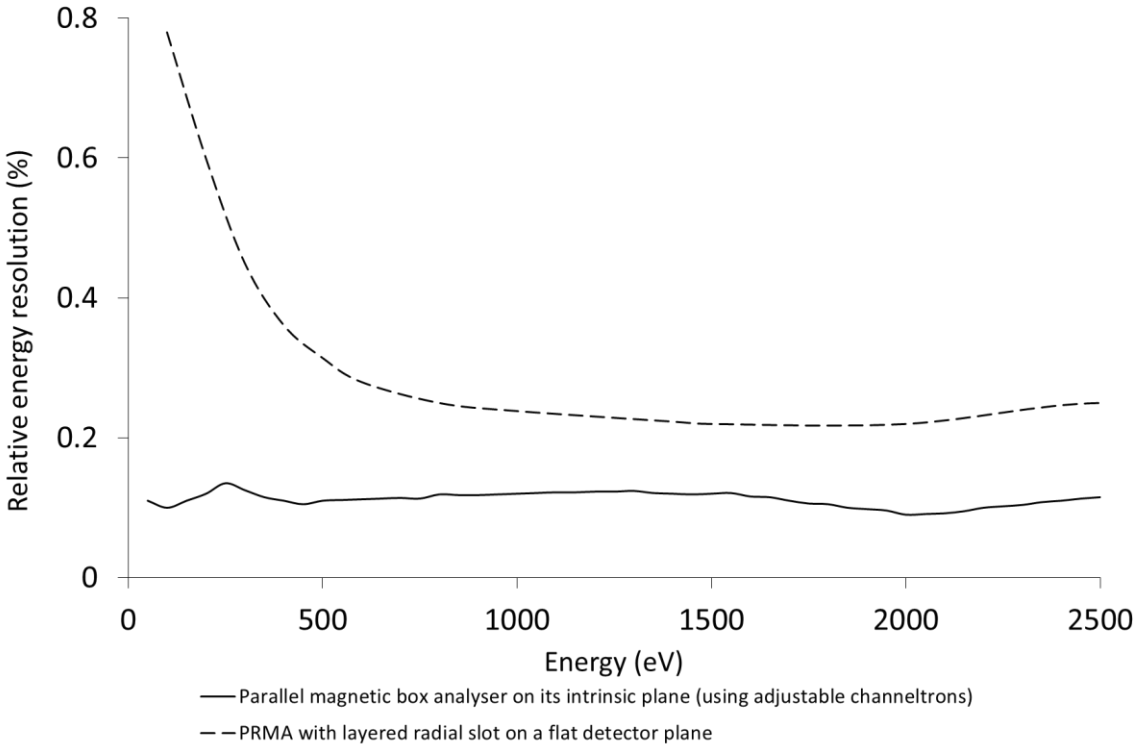

Figure 6.1: Comparison of the simulated relative energy resolution of the parallel magnetic box analyser on its intrinsic plane with the PRMA on a flat detector plane.

6.2 Suggestions for future work

The PRMA's most important merit lies in its high theoretical transmittance, that is, its full 2π rotationally symmetric detection plane. However, to take full advantage of this, curvilinear shaped position sensitive detector units are required, which at the moment, do not exist commercially. For the practical proposal of using an array of channeltrons, a means for widening the range of collection in the azimuthal angular direction needs to be found. A circular aperture plate can be placed on the analyser detection plane, the plan view of which is shown in Figure 6.2. The simulated full trace-width (for a polar angular spread of $\pm 3^{\circ}$), W_i shown in Table 6.1 determines the width of the slots in the aperture plate. This kind of aperture plate can be readily fabricated by laser cutting technology.

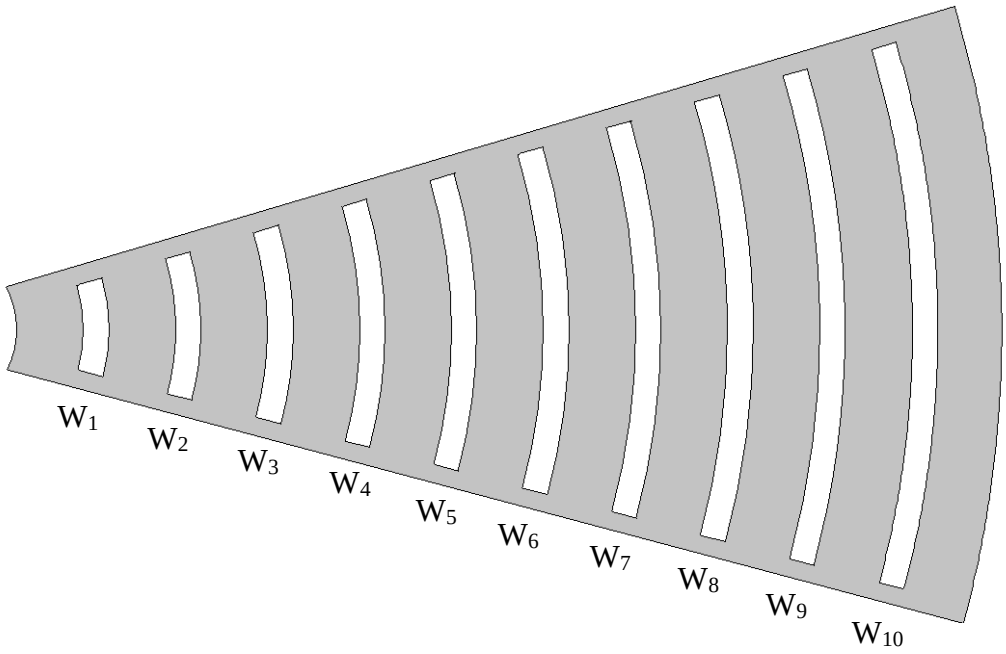

Figure 6.2: Top view of a possible circular aperture plate design to enlarge the range of collection in the azimuthal angular direction for the PRMA.

i	Energy (eV)	W_i, simulated full trace-width on the detector plane for ±3º polar angle (microns)
1	100	70
2	200	55
3	400	63
4	750	85
5	1000	110
6	1250	120
7	1500	124
8	2000	158
9	2500	151
10	3000	185

Table 6.1: Electron energy and their corresponding trace-width on the detector plane in microns.

Figure 6.3 shows the schematic diagram of one possible scheme for obtaining signals on the channeltron for a wider angular collection in the azimuthal direction. The diagram depicts an end view of the aperture plate/channeltron layout, as seen from the rotational axis. The wider angle electrons strike a 0 volt side-wall plate that has a high secondary emission yield, such as gold foil or Magnesium Oxide, effectively acting as an electron multiplier stage in the detection process. The channeltron entrance electrode will be biased up to several hundreds of volts in order to attract the secondary electrons created at the 0 volt side-wall on to the channeltron.

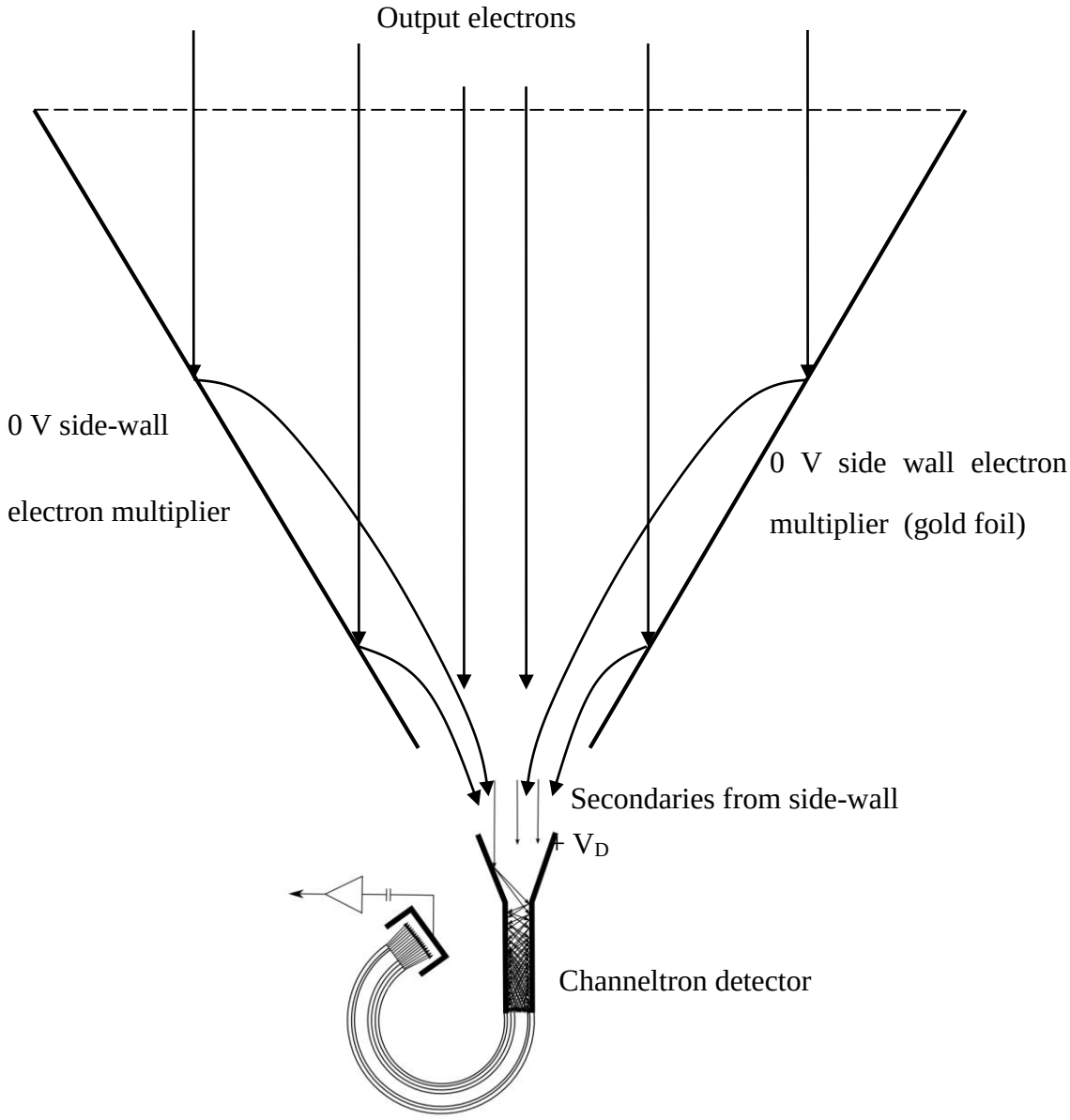

Figure 6.3: Schematic diagram of one possible scheme for obtaining signals on the channeltron for a given energy range from wider angle electrons in the azimuthal direction.

Another important line of development for future work is to investigate whether the optimised field distributions found for the Magnetic Box Analyser and the PRMA can be reduced to simple analytical expressions, which might help in understanding and improving their optics further. The fact this may be possible is already indicated by preliminary studies on the PRMA electric potential field distribution. Suppose that the field distribution is an ideal hyperbolic field in a $(u\text{-}v)$ coordinate, where the hyperbolic field distribution can be expressed as $V(u,v) = \frac{V_1}{b^2}uv$. Figure 6.4 shows the relationship between the $(u\text{-}v)$ and $(x\text{-}y)$ coordinate system.

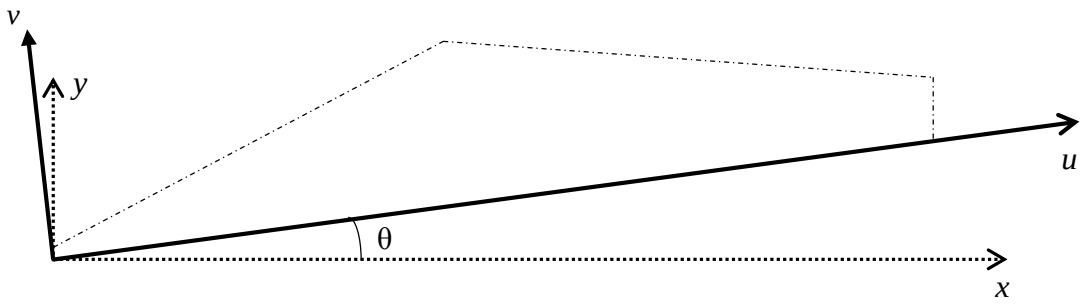

Figure 6.4: The $(u\text{-}v)$ and $(x\text{-}y)$ coordinate system are related by an angle of rotation, θ. The solid lines represent the $(u\text{-}v)$ coordinate system in an ideal hyperbolic field, and the dotted lines represent the $(x\text{-}y)$ coordinate system used in the simulation model.

Clearly, a transformation of $V(u,v)$ into $V(x,y)$ can be carried out by the following relations:

$$u = x\,cos\theta + y\sin\theta$$

$$v = -x\,sin\theta + y\,cos\theta$$

(θ is a negative angle)

The resulting electric potential can then be expressed as follows

$$V(x,y) = \sin(2\theta)\left(\frac{y^2}{2} - \frac{x^2}{2}\right) - xy(2sin^2\theta - 1) \qquad (6.1)$$

An approach is to determine the angle of rotation θ by considering a least-squares fitting between the simulated contour plot and the one analytically derived from equation (6.1). The second approach (which has been proven to be more effective) is to model the distribution in the PRMA by using a scaling factor $k > 0$ along the diagonal that makes an angle of -45º with the horizontal (x-axis). This can be easily achieved by a clockwise rotation of 45º, followed by a scaling of factor k along the vertical (y-axis) and finally, a counter-clockwise rotation of 45º. From equation (6.1), the resulting electric potential can then be expressed as follows

$$V(x,y) = -\left(\frac{-k^2}{2}\left(\frac{y}{\sqrt{2}} - \frac{x}{\sqrt{2}}\right)^2 + \frac{1}{2}\left(\frac{x}{\sqrt{2}} + \frac{y}{\sqrt{2}}\right)^2\right) \qquad (6.2)$$

The scaling factor k is then determined by mapping the potential distribution described by equation (6.2) to the numerically simulated contour plots in Figure 6.5. Only the desired region (marked by the red polygon) was considered during the least-squares fitting and k was found to be 1.37.

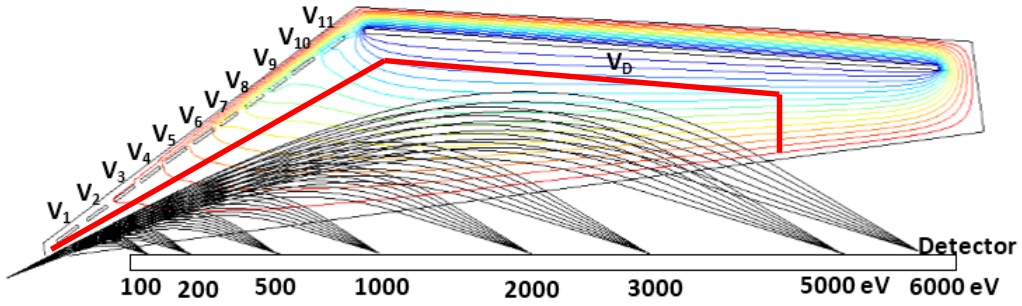

Figure 6.5: Mapping of the potential distribution described by equation (6.2) to the desired region marked by the red polygon in the numerically simulated contour plots, in order to determine the scaling factor k.

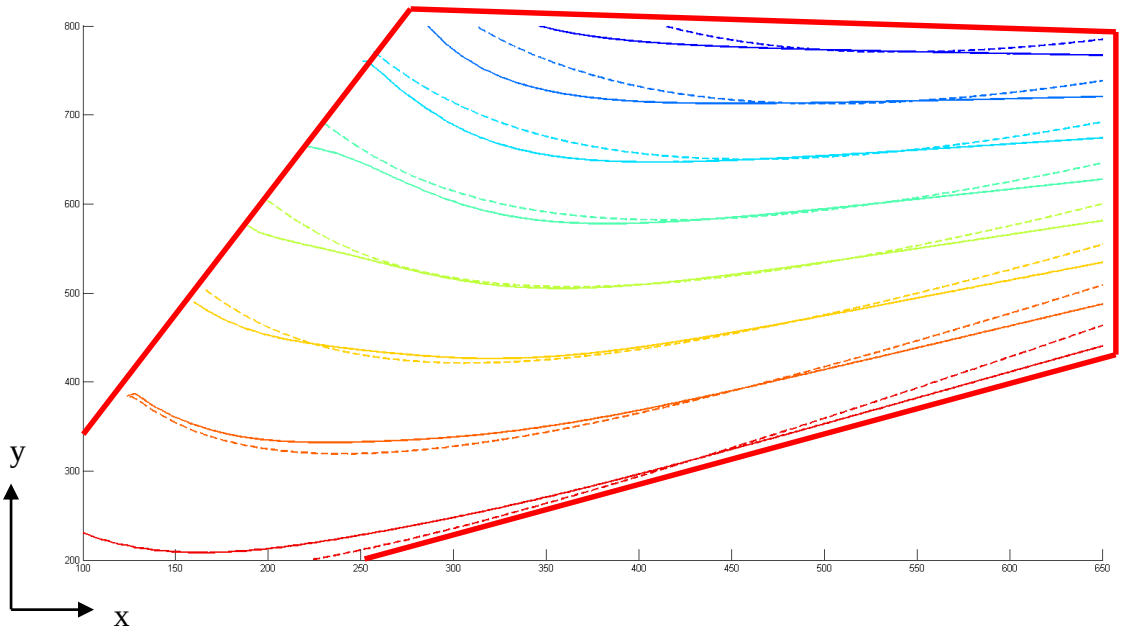

Figure 6.6: Comparison of the analytically derived and simulated contour lines of constant potential V(x, y) in the (x-y) coordinate system. Equipotential lines plot from -138.22 to -1332.59V in uniform steps of -149.29V are also indicated. Solid lines are from the numerical simulation while dotted lines are obtained from equation (6.2).

Figure 6.6 compares the analytically derived and Lorentz 2EM numerical simulated contour lines of constant potential $V(x, y)$ and shows good agreement between the two. Since $E(x, y) = -\nabla V(x, y)$, the required electric field is obtained by taking the corresponding partial derivative of equation (6.2). Figure 6.7 shows preliminary direct ray tracing of electron trajectory paths through this field by Lorentz 2EM, indicating that the analytical potential distribution does indeed focus electrons on to a flat detector plane.

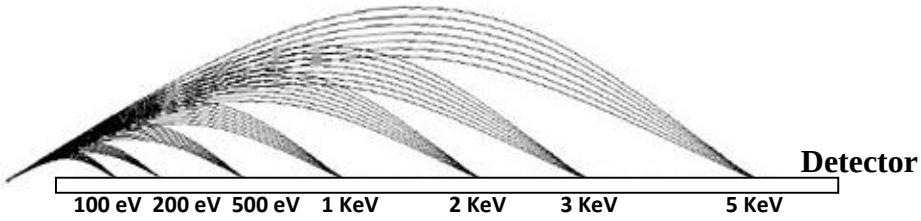

Figure 6.7: Direct electrons ray-tracing through the analytical function given in equation (6.2). At each energy, seven trajectories are plot evenly between -3° and 3°.

This approach indicates that it may be possible to find analytical representations of the numerically solved PRMA field distribution. Whether an analytical function exists which can produce second-order focusing across the entire energy range is a subject for future work. This analytical function approach may provide new insights on the conditions required to produce second-order focusing over a wide energy range.

References

[6.1] Lorentz-2EM, Integrated Engineering Software Inc., Canada, 2011.
[6.2] Lorentz-3EM, Integrated Engineering Software Inc., Canada, 2011.
[6.3] A. Khursheed, Design of a parallel magnetic box energy analyzer attachment for electron microscopes, Journal of Electron Spectroscopy and Related Phenomena, 184 (2011) 57-61.

Appendix A: Further details of the Damped least-squares optimisation program

This appendix further details how the DLS optimisation program can be applied to optimise for parameters in energy spectrometer's design. These parameters are illustrated in Figure A1: (a) minimise the vertical heights of the smallest focal points from a horizontal detector plane, where the detector plane is taken to be the mean of the height of the focal points, i.e. minimise $Y_1, Y_2, Y_3 \ldots Y_n$; (b) minimise the simulated relative energy resolution across the entire energy range at a pre-determined detector height, i.e. minimise $L_1, L_2, L_3 \ldots L_n$; (c) minimise the relative energy resolution, i.e. minimise $W_1, W_2, W_3 \ldots W_n$, and determine the focal plane shape for the best spectrometer performance (intrinsic resolution).

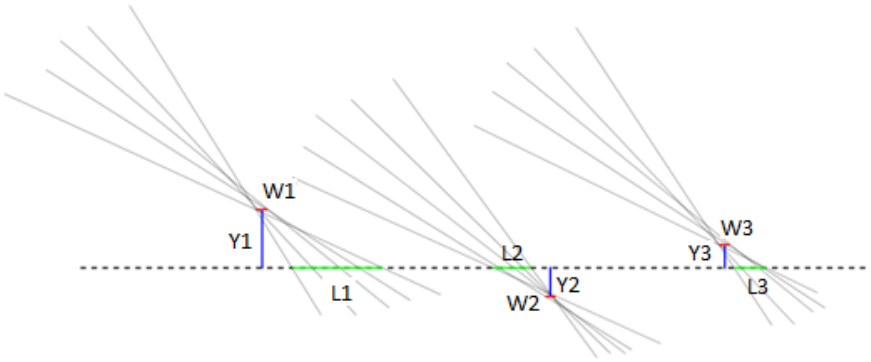

Figure A.1: Parameters to be optimised for in an energy spectrometer design (a) Minimisation of the vertical height Y_1, Y_2, Y_3 from a horizontal detector platem (b) Minimisation of the relative energy resolution across the entire energy range at a pre-determined detector plate, indicated along L_1, L_2, L_3 (c) Minimisation of the relative energy resolution on the output focal plane indicated along W_1, W_2, W_3.

The excitation strength of the magnets (or the voltage of the electrodes) is first given a step size and changes in the parameters are recorded in order to compute the Jacobian matrix of the system. When the parameter (such as vertical height Y_1, Y_2, Y_3) is being minimised for, it is akin to shifting the minimum trace-width located at the best focal point of each set of electron ray paths down (or up) onto a pre-determined detector plane. This has the effect of degrading

the focusing properties that were initially located at the best focal point. Simulation results predict that it is best to optimise for operand (a) and (b) simultaneously in order to achieve good focusing properties along a horizontal detector plane.

Many features in Lorentz can only be accessed through the Graphical User Interface (GUI). To overcome the lack of advanced scripting functionality in Lorentz, GUI automation had to be used to run simulations in Lorentz with varying parameters without human intervention. This is critical when dealing with a highly iterative numerical method like the Damped least-squares (DLS). The Python GUI automation library *Pywinauto*[1] was used for this purpose.

Pywinauto uses an object-oriented model to interact with the GUI of an application. First, the application is started with the command:

app = application.Application.start(pathToApplication)

Then the topmost window can be accessed through the member function, *app.top_window_()*.

Following that, we can perform interaction with the GUI. For example, to open up the Material Table in Lorentz, the code is:

app.top_window_().MenuSelect("Physics->Material Table")

To implement certain existing function ("save", for example) via the Lorentz command line, the code is: *app.top_window_().CommandEdit.SetEditText("save")*

Combination of such commands can be used to interact with the GUI such that all the

1 Available at https://code.google.com/p/pywinauto/

simulations and parameter modification in Lorentz are implemented automatically. In order to carry out the iterative steps listed in the DLS flow diagram (Figure 1 of Chapter 2), the GUI automation has to be carried out in different sections. Each section is encapsulated in a function in the optimisation program. The actions are:

- Opening a model in Lorentz
- Closing a model in Lorentz
- Checking the value of the Lorentz command line output
- Checking the value of the Lorentz command line input
- Getting the B-H curve of a material (for optimizing the magnetic box)
- Applying the B-H curve of a material (for optimizing the magnetic box)
- Amend any geometry or layout
- Setting the voltage of a specific electrode by specifying a bounding box that surrounds it (for optimizing the PRMA)
- Launching the electron emission, and then checking periodically to see when it has finished
- Writing the electron trajectory data to an output file

With these basic actions, a user can then automate the entire process of optimising an analyser design, which uses the above actions in the following order:

1. Open model
2. Set voltages of electrodes (or apply B-H curve of materials) or amend geometry/layout
3. Launch electron emission
4. Check that simulation is completed
5. Write trajectory data
6. Close model (if necessary)

Appendix B: Publications resulting from this project

A. Khursheed, K. H. Cheong & H. Q. Hoang, (2010). Design of a parallel mass spectrometer for focused ion beam columns. *Journal of Vacuum Science & Technology B, 28*(6), C6F10-C6F14.

K. H. Cheong, & A. Khursheed, (2011). A parallel magnetic sector mass analyzer design. *Nuclear Instruments and Methods in Physics Research Section A: Accelerators, Spectrometers, Detectors and Associated Equipment*, *645*(1), 221-226.

K. H. Cheong, W. Han, A. Khursheed, K. Nelliyan. A Parallel Radial Mirror Energy Analyser attachment for the Scanning Electron Microscope, Accepted for publication in *Microscopy and Microanalysis*.